ABSTRACT

Title of Dissertation:	WINTER STORM TRACKS, RELATED WEATHER, AND SUBSEASONAL-TO-SEASONAL (S2S) PREDICTION IN THE NCEP CLIMATE FORECAST SYSTEM FOR NORTH AMERICA
	Katherine Elizabeth Lukens Doctor of Philosophy, 2019
Dissertation directed by:	Research Professor Ernesto Hugo Berbery, Department of Atmospheric and Oceanic Science

The subseasonal-to-seasonal (S2S) forecast period (2 weeks—2 months) represents a major gap in operational forecasting. Advancing S2S prediction is an international priority, particularly for disaster mitigation and resource management decisions. If storm tracks contain S2S signals, their characterization in long term forecasts could advance S2S prediction by providing important information at longer lead times that may not be acquired from standard wind and precipitation forecasts.

Potential damaging effects of Northern Hemisphere winter storm tracks on North American weather are investigated using the NCEP Climate Forecast System (CFS) reanalysis (CFSR). Storm tracks are described by objectively tracking 320-K isentropic potential vorticity anomalies (PV_{320}). Large increases in deep convective heating, near-surface winds, and precipitation are found where strong storms (those

with higher PV_{320}) are most intense. The eastern US and North American coasts are most vulnerable to strong-storm related losses, which depend on the dynamics and local population density. Despite representing a small fraction (16%) of all storms, strong-storm tracks have a significant imprint on winter weather potentially leading to structural/economic loss.

Storm tracks in weeks 3-4 CFS reforecasts (CFSRR) are examined to assess their potential use in S2S prediction. Removal of statistically significant positive biases in PV_{320} storm intensity improves general storm track features. CFSRR reproduces observed storm-related weather and the characteristic intensity/frequency of hazardous strong-storm winds. Bias-corrected reforecasts better depict the observed variability in storm-related weather. CFSRR contains useful storm track-related information supporting our hypothesis that storm track statistics contribute to the advancement of S2S prediction of hazardous weather in North America.

The weeks 3-4 CFS version 2 (CFSv2) operational forecast performance is evaluated from a storm-focused perspective. CFSv2 retains the ability to predict general storm track behavior. Significant negative biases in storm intensity are apparently driven by mean static stability, with relative vorticity being a secondary driver. CFSv2 partially encapsulates the variability in storm winds and generally reproduces more extreme precipitation observations. Bias corrections improve storm wind forecasts. This work demonstrates that the use of climatological PV storm track statistics coupled with an appropriate storm track bias correction is a powerful instrument for the advancement of S2S prediction.

WINTER STORM TRACKS, RELATED WEATHER, AND SUBSEASONAL-
TO-SEASONAL (S2S) PREDICTION IN THE NCEP CLIMATE FORECAST
SYSTEM FOR NORTH AMERICA

by

Katherine Elizabeth Lukens

Dissertation submitted to the Faculty of the Graduate School of the
University of Maryland, College Park, in partial fulfillment
of the requirements for the degree of
Doctor of Philosophy
2019

Advisory Committee:
 Associate Professor Kayo Ide, Chair
 Research Professor Ernesto Hugo Berbery, Co-chair/Advisor
 Distinguished University Professor Eugenia Kalnay
 Associate Research Professor Alfredo Ruiz-Barradas
 Professor Da-Lin Zhang
 Associate Professor Michael Evans, Dean's Representative

Dedication

My thesis is dedicated to my mother, Beth Lukens, my father, Jim Lukens, and my brothers, Kenny and Tim Lukens. Their unwavering support has helped guide me along this journey.

I am especially thankful to my mother. She is my best friend and the person to whom I turn for support and advice on all things. Her composure and wisdom, particularly during my more frantic moments, continue to give me the strength and courage to accomplish every one of my goals.

I am incredibly grateful for my father, whose passion for meteorology sparked my own love for the atmospheric sciences at a very young age. His love and encouragement to pursue my dreams has helped to fan a spark of wonder into a flame of academic ambition that has led me toward a promising career in atmospheric science.

I further dedicate this work to my grandmothers, Margaret Ionni and Mildred Lukens. Your love and support over the years have shown me what family truly means. Even when we are not together, you are always with me. I am so proud to be your granddaughter.

This work is for my sisters by choice, Elyse Colbert Hagner, Briana Hawras, and Courtney Spamer Travis. They have seen me at my very best, and they have stood by me through the very worst. Though we are not bound by blood, we share an unbreakable kinship that has always served as a haven of cheer and inspiration when I needed it most. Thank you, ladies, for being in my life!

I want to thank all of my dear friends at the University of Maryland, Penn State, and beyond for their love and moral support, and for reminding me to have fun once in a while! You mean the world to me.

Finally, I dedicate this thesis to Stephen Doore. I cannot adequately express in words how meaningful your presence in my life has been these last years. You are one of the few people on this earth on whom I can truly rely, not only for support but for stability, empathy, and love when life becomes chaotic. You are generous and so kind, and you keep me grounded. I know I would not have made it this far without you. I love you. Thank you for being my rock.

Acknowledgements

This thesis and the work presented therein would not exist without the support of my advisor, Dr. Ernesto Hugo Berbery. I will be forever grateful for his taking me on as a student years ago. Through the highs and lows of my graduate career, Hugo has shown me nothing but patience and a willingness for me to succeed. He has taught me so much, and I continue to learn from his example as a scientist and mentor. He has had an immense positive impact on my career, and I credit his invaluable guidance in having helped shape me into the scientist I am today. Thank you, Hugo, for everything you have done for me.

I would like to express my sincere appreciation for the members of my dissertation committee, Dr. Kayo Ide, Dr. Eugenia Kalnay, Dr. Alfredo Ruiz-Barradas, Dr. Da-Lin Zhang, and Dr. Michael Evans for their valuable suggestions and comments on my dissertation.

I thank Dr. Kevin Hodges for his computational support with the storm tracking methodology that formed the foundation of the experiments presented in this thesis. I also thank Mr. Patrick Meyers for his technical advice and overall support of my graduate work.

I am so grateful for the continued support of my undergraduate advisors at Penn State, Dr. Steven B. Feldstein and Dr. Sukyoung Lee. They each played critical roles in developing my research ability through their encouragement, mentorship, and passion for science. Moreover, their belief in me as a scientist strengthened my own resolve to pursue a graduate degree and a career in atmospheric research.

Table of Contents

List of Tables

List of Figures

List of Abbreviations

°	= degrees
°N	= degrees North
°W	= degrees West
∂	= partial derivative
$\dfrac{\partial\theta}{\partial p}$	= static stability
$\dfrac{\partial\mathbf{v}}{\partial z}$	= vertical wind shear
∇	= vector differential operator
ζ_θ	= isentropic relative vorticity
θ	= potential temperature
Σ	= sigma
σ_B	= Eady growth rate
ω	= vertical wind in pressure coordinates
4D	= 4-dimensional
AO	= Arctic Oscillation
ATOVS	= Advanced TIROS Operational Vertical Sounder
CDASv2	= Climate Data Assimilation System version 2
CFS	= Climate Forecast System
CFSR	= Climate Forecast System Reanalysis
CFSRR	= Climate Forecast System Reanalysis and Reforecasts
CFSv1	= Climate Forecast System version 1
CFSv2	= Climate Forecast System version 2
CMAP	= Climate Prediction Center Merged Analysis of Precipitation
CONUS	= contiguous United States
c_p	= specific heat for dry air at constant pressure
CPC	= Climate Prediction Center
DJF	= December-January-February
ECMWF	= European Centre for Medium-Range Weather Forecasts
f	= Coriolis parameter
g	= gravitational constant
GDAS	= Global Data Assimilation System
GFS	= Global Forecast System
GLDAS	= Global Land Data Assimilation System
GODAS	= Global Ocean Data Assimilation System
GPCP	= Global Precipitation Climatology Project
GSI	= gridded statistical interpolation
H1	= hybrid level 1
hPa	= hectopascals
i	= time index
K	= Kelvin
km	= kilometers

mph	=	miles per hour
m s^{-1} (or m/s)	=	meters per second
MAE	=	mean absolute error
MJO	=	Madden-Julian Oscillation
MSLP	=	mean sea level pressure
N	=	Brunt-Väisälä frequency
n	=	number of winters in period of analysis
NAA	=	North American-Atlantic
NCAR	=	National Center for Atmospheric Research
NCEP	=	National Centers for Environmental Prediction
NCL	=	NCAR Command Language
NH	=	Northern Hemisphere
NMME	=	North American Multi-Model Ensemble
N_{pop}	=	local population number
p	=	pressure; vertical coordinate
PR	=	precipitation rate
PV	=	isentropic potential vorticity
PV_{320}	=	potential vorticity at 320 K
PVU	=	Potential Vorticity Units
PV_x	=	maximum PV intensity
$\dot{Q}/c_p$	=	residual diabatic heating rate
R	=	gas constant
RMSE	=	root mean squared error
RSR	=	ratio of RMSE to standard deviation of (re)analysis
S2S	=	subseasonal-to-seasonal
SD	=	standard deviation
SSI	=	spectral statistical interpolation
SST	=	sea surface temperature
SubX	=	Subseasonal Experiment
SW-NE	=	southwest-northeast
T	=	temperature
t	=	time
T42	=	Truncation 42 horizontal resolution
T574	=	Truncation 574 horizontal resolution
T_{all}	=	all-storm track maximum intensity threshold
T_{str}	=	strong-storm track maximum intensity threshold
TOVS	=	TIROS Operational Vertical Sounder
UTC	=	Coordinated Universal Time
v	=	wind vector
v	=	local storm track-related wind speed
v_{98}	=	local wind speed at the 98th quantile
X	=	(re)analysis storm track PV intensities or related weather variables
x	=	horizontal coordinate in the x-direction
Y	=	(re)forecast storm track PV intensities or related weather variables
y	=	horizontal coordinate in the y-direction

Chapter 1: Introduction

The subseasonal-to-seasonal (S2S) time frame (ranging from 2 weeks to about 2 months) has largely been considered a major gap in operational forecasting as it represents a forecast range that bridges weather and climate prediction and is not well-defined by either category. Figure 1.1 (Mariotti et al. 2018, their Fig. 1) illustrates the change in prediction skill with lead time for weather, S2S, and climate prediction. For weather forecasts the prediction skill is generally known and is high at short lead times (hours) and decreases with increasing lead time out to 2 weeks. For climate or seasonal outlooks the skill is consistently low-to-moderate for forecasts beyond 2 months. The S2S time frame lies in between, and the prediction gap is emphasized by a question mark. The need to address this gap and advance S2S prediction is internationally recognized as a high priority (Brunet et al. 2010; Vitart et al. 2012, 2017; Mariotti et al. 2018). Studies suggest that identifying sources of predictability at S2S scales could considerably benefit society by offering actionable information that could (a) facilitate disaster mitigation efforts and help optimize the security of life and property, and (b) enhance management practices across multiple sectors including agriculture, water security, public health, transportation, and energy (e.g., Shapiro et al. 2010; White et al. 2017; Vitart et al. 2012, 2017).

Studies indicate that there are numerous potential sources of S2S predictability, including the Madden-Julian Oscillation (MJO) and stratospheric initial conditions (Baldwin and Dunkerton 2001; Waliser et al. 2003; Vitart 2014). It has been shown that improvements in the representation of the MJO and related teleconnections in

The S2S Prediction Gap
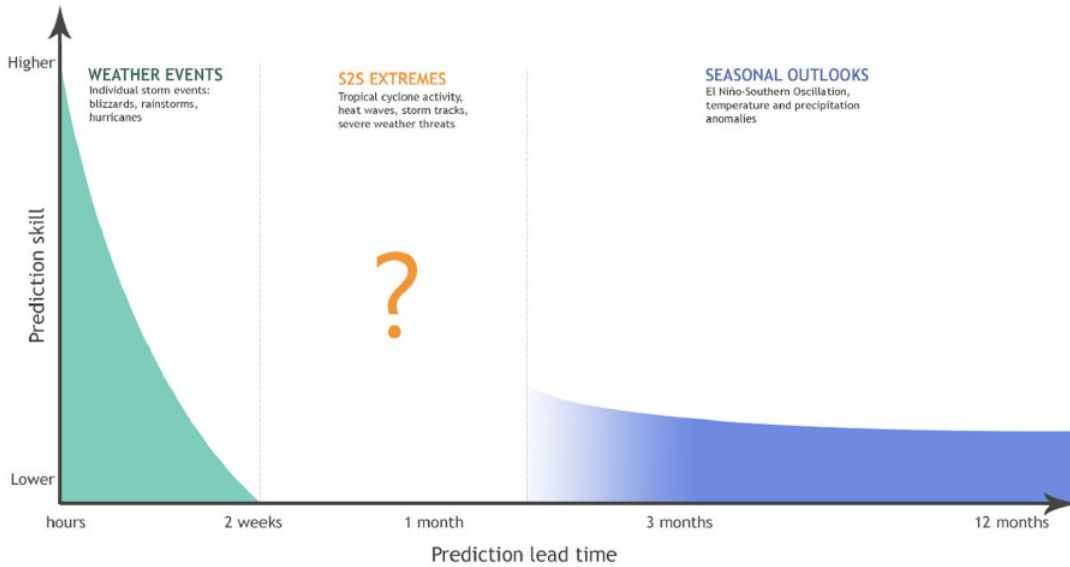
Figure 1.1: Schematic of prediction skill on the y-axis versus lead time on the x-axis. The S2S prediction gap is highlighted by a question mark in between (left group) weather prediction, and (right group) climate prediction (or seasonal outlooks). NOAA CPO graphic taken from Mariotti et al. (2018), their Fig. 1, originally adapted from IRI.

forecast models can largely contribute to increased forecast skill, e.g., of the North Atlantic Oscillation index and surface air temperatures in the extratropics (Lin et al. 2010; Vitart 2014). Further, better characterization of stratospheric conditions and thus the intraseasonal memory of the stratosphere in dynamical models have the potential to improve subseasonal prediction (Baldwin et al. 2003; Brunet et al. 2010).

Convection in the tropical Pacific that is associated with the MJO and excites Rossby wave activity has been found to largely contribute to intraseasonal (30-90 day) storm track variability over North America (Grise et al. 2013; Guo et al. 2017; Zheng et al. 2018). In addition, variations in stratospheric circulation anomalies tend to precede shifts in the storm tracks by ~60 days (Baldwin and Dunkerton 2001). More importantly, storm tracks can themselves contain signals in S2S, and this is important

for S2S weather prediction, e.g., because winter weather in North America is largely influenced by the Pacific and Atlantic storm tracks (Hawcroft et al. 2012; Ma and Chang 2017). If forecast models contain storm track-related S2S signals and account for potential sources of predictability, then the characterization of storm tracks in long term forecasts could help advance S2S weather prediction by providing key information that may not be acquired from standard wind and precipitation forecasts.

1.1   *Dynamics of Winter Storm Tracks and Environmental Influences*

Two well-documented mid-latitude winter storm tracks in the Northern Hemisphere (NH) affect weather and climate in North America: the Pacific storm track which extends eastward across the North Pacific Ocean, and the Atlantic storm track which extends northeastward across the North Atlantic Ocean. Elsewhere in the NH mid-latitudes there is the Mediterranean storm track which spans eastward across the Mediterranean Sea to the Middle East (Hoskins and Hodges 2002). The storm tracks are characterized as large narrow bands of high baroclinic instability along which individual storms tend to propagate, and are maintained by the continuous downstream development of baroclinic disturbances (Simmons and Hoskins 1979; Wallace et al. 1988; Orlanski and Chang 1993). The upper-tropospheric winds (i.e., the 200-hPa jet stream) and divergence aloft produce cyclonic circulation poleward of the zonal flow, enhancing cyclonic shear and generating upstream confluence that can predominantly maintain the mean baroclinicity needed for continued downstream eddy activity (Wallace et al. 1988; Hoskins and Valdes 1990). Even in cases of weaker instability, the downstream radiation of kinetic energy in the form of ageostrophic geopotential

fluxes contributes to the growth and intensification of new eddies at the expense of upstream decaying eddies (Simmons and Hoskins 1979; Orlanski and Chang 1993). Baroclinic disturbances propagate downstream as large-scale wave packets with a group velocity that primarily dictates the speed at which new eddies develop (Orlanski and Chang 1993).

Many factors influence the NH storm track distribution, including sea surface temperature (SST) gradients, uneven heating, and orography (Hoskins and Valdes 1990; Held 1993; Brayshaw et al. 2008, 2009; Chang 2009). A strong mid-latitude SST gradient alongside a reduced subtropical SST gradient will generally strengthen the storm tracks and shift them poleward (Brayshaw et al. 2008). In the North Atlantic the large SST gradient formed by the protrusion of the warm Gulf Stream into the cool higher latitude ocean induces surface wind convergence on the warm side of the Gulf Stream front, intensifying the vertical wind velocity and vertical instability, in turn enhancing convection and storm development (Minobe et al. 2008, 2010).

Uneven diabatic heating induced in part by land-sea temperature contrasts plays a role in storm track modulation (Hoskins and Valdes 1990; Chang 2009). As cool westerly flow off the land passes over warmer western oceans, the surface air warms rapidly, triggering the generation of surface sensible heat fluxes that act to destabilize the atmosphere (Mak 1998). The sensible heat fluxes counter the damping effect of poleward eddy heat fluxes, preserving baroclinicity at the surface and maintaining the storm tracks through the development of unstable waves aloft (Hotta and Nakamura 2011). Asymmetries in diabatic heating partly account for the greater strength of the Atlantic storm track compared to the Pacific storm track, despite the lower baroclinicity

in the Atlantic (Chang 2009). For instance, the large land-sea temperature gradient in winter induced by strong air mass contrasts between cold air over northeastern North America and warmer air over the Gulf Stream form a region of particularly high baroclinic instability along an axis that follows the North American east coast (Brayshaw et al. 2009). Storms tend to deepen and intensify leeward of the Appalachian Mountains (Colucci 1976), and the baroclinic zone over the North American east coast promotes the further amplification of storms, including nor'easters (Davis and Dolan 1993). Additionally, the strength and areal width of marine storms are determined by the intensity of the diabatic heating (Mak 1998).

As for orographic influences, mountainous terrain mainly acts to suppress storm track activity by blocking or deflecting the westerly flow over land (Chang 2009). The Rocky Mountains deflect westerly Pacific cyclones/storms southward which leads to a southwest-northeast (SW-NE) tilt in the upper tropospheric jet, the subsequent downstream flow, and the Atlantic storm track, dynamically separating the Northern Hemisphere storm tracks (Brayshaw et al. 2009; Chang 2009). The Atlantic track lies coincident with the SW-NE axis of the low-level baroclinic zone that follows the North American east coast, further enhancing cyclonic activity in the region of the Atlantic storm track (Brayshaw et al. 2009).

1.2   *Storm-Related Winter Weather and Storm Loss*

High impact weather events (e.g., droughts, floods, heat waves, wildfires, and persistent periods of cold) have a history of physically and fiscally devastating society. This is also the case of extratropical storms. Strong storms have the potential to produce

high winds and heavy precipitation that can induce, e.g., transportation interruptions, higher demands for power and emergency supplies, and an increased risk of damages and casualties (Kunkel et al. 2013; Wang et al. 2017). In populated areas there is great potential for the near-surface wind distribution to change dramatically and inflict serious damage during the evolution of intense extratropical cyclones. Over open waters strong near-surface winds have great impacts where maritime transportation, fishing vessels, and manned offshore oil and gas production units are most vulnerable (Bell et al. 2017). Strong storms can also change the winter precipitation distribution by generating excessive amounts in a relatively short amount of time (days to a week). Lasting and possibly devastating effects like major flooding and wind damage may result leading to states of emergency, especially when the cumulative impacts and insurance losses from several storms occurring in rapid succession are considered (Mailier et al. 2006).

Shifts in storm track behavior can yield corresponding changes in the intensity and frequency of extreme precipitation and wind events, which can profoundly affect a region's climate. For instance, a northward shift of the Pacific storm track brought about by a deepening of the semi-permanent Aleutian Low in the high latitudes can amplify winter precipitation in western North America (Chang et al. 2002; Salathé 2006; Kunkel et al. 2012; Pfahl and Wernli 2012; Ma and Chang 2017).

The storm tracks are collocated with climatological precipitation maxima that exceed 6 mm day^{-1} over the respective ocean basins (Adler et al. 2003; Hawcroft et al. 2015; Xie et al. 2017). Further, precipitation and upper-level zonal flow are highly correlated over the mid-latitude oceans and over land upstream of high orography,

supporting the notion that strong baroclinic cyclones aloft lead to large accumulations of precipitation at the surface (Maddox et al. 1979; Garreaud 2007; Pfahl and Wernli 2012). Storms and frontal systems account for over half of the mean total winter precipitation in the mid-latitudes (Catto et al. 2012; Hawcroft et al. 2012; Pfahl and Wernli 2012). Extremely high precipitation is produced primarily by extratropical storms with the most heavily precipitating storms contributing substantially to the winter climatological precipitation (Maddox et al. 1979; Hawcroft et al. 2012; Pfahl and Wernli 2012). Over land, precipitation tends to increase upstream of high orography due to a combination of orographic uplifting and a strong upper-level zonal flow that drives storm intensification and rapid storm succession (Garreaud 2007). Specifically in North America, over 70% of winter precipitation is associated with low-level cyclonic activity (Hawcroft et al. 2012).

Recent studies have found that there is significant skill in the seasonal prediction of mid-latitude storm tracks and extremes, particularly in winter (e.g., Yang et al. 2015). In the last few decades in the United States, weather-related losses have increased (Kunkel et al. 1999; Pielke and Carbone 2002; Karl et al. 2008), and the vulnerability to storm-related loss is expected to rise with projected increases in strong-storm frequency and intensity (Karl et al. 2008; Shapiro et al. 2010; Kunkel et al. 2013; Lawrimore et al. 2014). As such, the study of storm tracks and related impacts is critical for understanding the effects of destructive weather and anticipating weather-related fluctuations in the state of the economy, particularly in winter.

1.3   Objectives of this Research

This work aims to contribute to the understanding of the subseasonal-to-seasonal prediction gap in operational forecasting by assessing (and potentially improving) the prediction of storm tracks and related weather at S2S time scales in North America. Specifically, our work investigates the impact of strong winter storms tracks on surface weather and related structural and economic loss using the National Centers for Environmental Prediction (NCEP) Climate Forecast System (CFS) Reanalysis (CFSR). Additionally, we evaluate the ability of the NCEP CFS to reproduce storm track behavior and related winter weather in subseasonal retrospective forecasts (i.e., reforecasts/hindcasts) and operational forecasts. Table 1.1 summarizes

Table 1.1: Table of descriptions of datasets and relevant changes in the NCEP Climate Forecast System. Information is consolidated from Saha et al. (2010a), Chelliah et al. (2011), Wang et al. (2011), Saha et al. (2014a,b,c), NCEP (2015), National Weather Service (2019), and NCEP Central Operations

Implementation Date	Description
Jan 2015	*GFS/GDAS upgrade:* Increased horizontal resolution; upgraded model physics; enhancements to Hybrid 3D-VAR EnKF data assimilation; 1-degree soil moisture climatology replaced with CFS/GLDAS climatology at T574 resolution.
2011 - Present	*CFSv2/CDASv2 operational forecast data range*
March 2011	*CFS operational model upgraded to version 2 (CFSv2):* Major upgrade to modeling system, output product content and format, model components, etc. *--Atmospheric model:* Virtual temperature instead of enthalpy is used as prognostic variable; Disabled 2 simple modifications made in CFSR to improve marine stratus prediction; Added new parameterization gravity wave drag induced by cumulus convection; Advanced cloud-radiation interaction scheme is applied in Rapid Radiative Transfer Model (RRTM); In-cloud condensate mixing ratio is computed by ratio of grid mean condensate mixing ratio and cloud fraction when cloud fraction is > 0; CO_2 mixing ratio includes climatological seasonal cycle superimposed on observed estimate at initial time. *--Noah land surface model:* CFSv2/Noah vegetation parameters and rooting depths refined to increase evapotranspiration; surface runoff parameters were nominally adjusted to increase predicted runoff.
2008	CFS/GODAS upgrade (Deep Water Assimilation): Introduced 2 new members out to 9 months; reduced initial conditions to 1-day lag in ocean and atmosphere.
May 2007	SSI replaced with GSI in operations. Operational GSI forms the basis for the CFSR.
1998	Assimilated data into CFSR changed from TOVS to Advanced TOVS (ATOVS)
1982 - March 2011	*CFS Reforecast (CFSRR) data range*
1979 - March 2011	*CFSR data range*

the changes made to the CFS over time as well as the temporal ranges for the reanalysis, reforecast, and operational forecast datasets.

The weeks 3-4 time frame is our chosen sub-monthly forecast period of analysis. This forecast period represents the gap in predictability as it lies between what is characterized as weather prediction (out to 2 weeks) and forecasts beyond one month that benefit from improved representations of intraseasonal phenomena like the MJO that has a period of 30-90 days (Mariotti et al. 2018). Further, resource management decisions can benefit from accurate forecasts at weeks 3-4 time scales (Vitart et al. 2012, 2017; Mariotti et al. 2018). For example, improved total rainfall forecasts at longer lead times can offer the agriculture sector more time to prepare for potential impacts from flooding or dry periods. In addition, the NCEP Climate Prediction Center (CPC) routinely issues weeks 3-4 outlooks for precipitation and temperature. Our work addresses the following objectives:

Objective 1: The first objective is to provide a comprehensive assessment of winter storm track behavior and corresponding structural and economic loss from a storm-focused perspective. We investigate the relation of winter storm tracks to surface weather and diabatic heating distributions by identifying the general properties of the more intense (severe) storm tracks during the NH winter in the CFSR. Further, we examine the relation of winter storm tracks to North American high impact weather (as measured by low-level winds and precipitation intensity) and related potential damaging effects.

Objective 2: The second objective is to evaluate the potential use of storm track statistics in the advancement of S2S prediction. We assess to what extent the storm

tracks can be anticipated at the weeks 3-4 lead time in the CFS reforecasts (CFSRR). Statistically significant systematic biases are found in the storm track reforecasts, and they are removed in order to gauge whether additional improvement can be gained in the prediction of expected severe weather in a conceptual forecast mode.

Objective 3: The final objective of this thesis research is to assess the usefulness of storm track diagnostics in operations. This is done by evaluating the performance of the weeks 3-4 operational forecasts of storm track behavior and related weather in the CFS version 2 (CFSv2). The analysis is expanded to include separate assessments of the storm tracks in the Pacific and Atlantic regions, and bias corrections are applied to evaluate whether any additional improvements can be gained. In addition, we explore the potential sources of the storm track intensity biases found in the operational forecasts at weeks 3-4 time scales in order to further our understanding of their characterization and impact in the CFS.

The objectives are achieved through the use of a Lagrangian storm tracking approach (Hodges 1995, 1999; Hoskins and Hodges 2002). The storm tracking approach objectively identifies maxima in dynamic variables (e.g., potential vorticity) as extratropical cyclones and tracks the evolutions from development (cyclogenesis) to dissipation (cyclolysis). Sets of statistics are generated from the tracked mid-latitude cyclones and are used in the analysis of storm track behavior and related impacts. A high-level description of the approach is presented in Chapter 2.

The dissertation is organized as follows. Chapter 2 presents a comprehensive analysis on the behavior of strong winter storm tracks and the potential damaging effects of related high impact weather in North America. Chapter 3 assesses whether

CFS weeks 3-4 reforecasts contain useful storm track-related information to warrant operational applications. Chapter 4 addresses the third objective by evaluating the use of storm track statistics for operational applications based on the conceptual analysis in Chapter 3. Moreover, the work in this chapter investigates the origin of storm track intensity biases found in the forecasts, and briefly explores whether the operational forecasts should be validated using the reforecasts. Reforecasts are often assumed to accurately represent corresponding operational forecast errors, and this can be potentially problematic, e.g., if updates to the operational model produce biases that differ from those in the reforecasts used to verify them.

Systematic biases are found in the storm track forecasts and reforecasts, and a bias correction method that identifies and removes the errors is developed and validated. The method is of simple design and can be implemented quickly, and this is advantageous for the rapid release of severe weather forecasts. Further, it can be adapted for use in different operational forecast models like those in the North American Multi-Model Ensemble (NMME; Kirtman et al. 2014), or the collaborative multi-model subseasonal prediction experiment SubX (Pegion et al. 2019, submitted manuscript). Use of the method is presented in Chapters 3 and 4.

Most of the content in this thesis is reorganized based on the publications of Lukens et al. (2018) and Lukens and Berbery (2019). Concluding remarks and future directions are presented in the final chapter.

Chapter 2: The Imprint of Strong-Storm Tracks on Winter Weather in North America

Abstract: Northern Hemisphere winter storm tracks and their relation to winter weather are investigated using CFSR data. Storm tracks are described by isentropic potential vorticity (PV) maxima within a Lagrangian framework; these correspond well with those described in previous studies. The diagnostics focus on strong-storm tracks, which are comprised of storms that achieve a maximum PV exceeding the mean value by one standard deviation. Large increases in diabatic heating related to deep convection occur where the storm tracks are most intense. The cyclogenesis pattern shows that strong storms generally develop on the upstream sectors of the tracks. Intensification happens towards the eastern North Pacific and all across the North Atlantic Ocean, where enhanced storm track-related weather is found. The relation of storm tracks to near-surface winds and precipitation is evaluated. The largest increases in storm track-related winds are found where strong storms tend to develop and intensify, while storm precipitation is enhanced in areas where the storm tracks have the highest intensity. Strong storms represent about 16% of all storms but contribute 30-50% of the storm precipitation in the storm track regions. Both strong-storm related winds and precipitation are prone to cause storm-related losses in the eastern US and North American coasts. Over the oceans, maritime operations are expected to be most vulnerable to damage offshore of the US coasts. Despite making up a small fraction of all storms, the strong-storm tracks have a significant imprint on winter weather in North America potentially leading to structural and economic loss.

In order to examine whether model forecasts contain useful storm track-related information to contribute to the advancement of S2S weather prediction, we must first understand the behavior of winter storm tracks and weather-related impacts. This chapter discusses the characteristics of storm tracks as constituted by storms that achieve high isentropic potential vorticity (PV) and thus will be called *strong-storm tracks*. The following objective questions are addressed: (1) how do strong-storm tracks relate to surface weather and diabatic heating distributions?, and (2) what are the potential damaging effects of very high near-surface winds and precipitation rates associated with the strong-storm tracks that could lead to structural and economic loss in North America? We also discuss the robustness of the results by using a dataset of observed precipitation.

Chapter 2 is drawn from the publication Lukens et al. (2018). The structure of the chapter is as follows: Section 2.1 describes the datasets and cyclone tracking method used. Section 2.2 discusses the properties of the strong-storm tracks that affect North American winter weather, while Section 2.3 examines the relation between the strong-storm tracks and the potential destructive effects of the associated wind and precipitation. Section 2.4 summarizes the key findings.

2.1   *Data and Analysis Methods*

2.1.1   Datasets

2.1.1.1 Climate Forecast System Reanalysis (CFSR)

The CFSR (Saha et al. 2010a) product is the most recent complete compilation of global reanalysis data generated by NCEP. The CFSR couples the atmosphere,

ocean, land surface, and sea ice to provide our best 4D view of the Earth's natural state, constrained by observations, every 6 hours. The global atmospheric data have a horizontal grid spacing of 38 km, 64 vertical sigma-pressure levels and are archived on a $0.5° × 0.5°$ latitude-longitude grid. The gridded statistical interpolation (GSI) scheme assimilates atmospheric variables including global precipitation rates derived from rain gauge and satellite observations into CFSR. The coupled assimilation provides a more complete and better-quality dataset of precipitation than past NCEP reanalyses that neglect coupling in the data assimilation, with better correspondence between the model physics and observed precipitation (Saha et al. 2010b; Wang et al. 2011). The accuracy of CFSR is improved over past NCEP reanalyses in part because of higher spatial and temporal resolutions, the assimilation of bias corrected observations, and the coupling to sea ice and the ocean (Saha et al. 2010b). Despite the improvements in CFSR, an artificial discontinuity around October 1998 in the wind and precipitation time series has previously been found. The ingestion of satellite observations often marks the onset of artificial trends in other reanalysis datasets (Bengtsson et al. 2004), and CFSR is no different. The discontinuity in CFSR is thought to be due to the introduction of the assimilation of data from the low-earth polar-orbiting Advanced TIROS Operational Vertical Sounder (ATOVS) satellite, which contributes to less spin-up of the initial moisture, resulting in a more humid atmosphere after 1998 (Saha et al. 2010b; Chelliah et al. 2011; Wang et al. 2011; Zhang et al. 2012). Our study uses CFSR data for DJF from 1980-2010 and examines this discontinuity to assess the potential effects on our results.

2.1.1.2 Global Precipitation Climatology Project (GPCP)

The GPCP (Huffman et al. 2012) 1-degree daily dataset of precipitation accumulations centered on 12:00 UTC are examined alongside the reanalysis information. Since October 1996, the GPCP has provided high quality, high resolution global precipitation data. The daily dataset is derived from the GPCP Version-2 Monthly Precipitation Analysis by combining in situ data (i.e., surface rain gauges) with histograms of 3-hourly infrared brightness temperatures from geosynchronous-orbit satellite infrared data and precipitation derived from atmospheric parameters retrieved from low earth orbit satellites (Huffman et al. 2001; Adler et al. 2003; Pendergrass 2015). In this study, GPCP daily precipitation is used for DJF from 1999-2010 and is taken as "ground truth" although some estimates, particularly over oceans, may be less reliable (Adler et al. 2012).

2.1.2   Tracking of Storms

Previous studies have used different metrics and variables to represent storm tracks, including mean sea level pressure (MSLP), geopotential height, and the meridional component of the upper tropospheric wind (e.g., Gulev et al. 2001; Hoskins and Hodges 2002; Raible 2007). A traditional metric used to describe general storm track behavior is the Eulerian diagnostic. In an Eulerian view, storm tracks are identified using band-pass or high-pass filtered variances of dynamic variables converted to standard deviations (Blackmon et al. 1977; Wallace et al. 1988). High standard deviations represent the variability in high frequencies and indicate high baroclinicity. A key element of the Eulerian view is the observation of a parcel's

movement from a single location. One-point lagged correlations illustrate this concept in terms of general storm track behavior by highlighting the basic characteristics of synoptic waves associated with high frequency fluctuations that pass over a single point. Lagged time correlations of variables like MSLP and 500-hPa geopotential height have often been used to describe the southwest-to-northeast downstream development of baroclinic waves that propagate within the NH storm track regions (e.g., Simmonds and Hoskins 1979; Wallace et al. 1988; Chang and Orlanski 1993). However, MSLP and 500-hPa geopotential height are dominated by large scales, making small-scale, high-frequency features like cyclones difficult to identify without bias toward larger, slower disturbances (Wallace et al. 1988; Hoskins and Hodges 2002). The upper-level meridional wind tends to better capture the higher frequencies and reveals downstream-developing wave trains along the storm tracks (Chang and Orlanski 1993; Berbery and Vera 1996).

The Lagrangian view is a more recently adopted framework for diagnosing storm track behavior. From this perspective, a cyclone is followed throughout its evolution. Low-level relative vorticity and PV are useful to track storms in a Lagrangian framework because of their dependence on higher order derivatives that allows for the detection of small scale features like cyclogenesis (Hoskins and Hodges 2002).

PV is particularly valuable as it includes both absolute vorticity and static stability (Hoskins et al. 1985), and thus describes the major dynamic and thermodynamic properties of atmospheric circulation. PV is defined in Eq. (2.1) as the

measure of the ratio of absolute vorticity (i.e., the measure of rotation) of a vortex to the depth of that vortex:

$$PV \equiv -g(\zeta_\theta + f)\frac{\partial\theta}{\partial p} \qquad (2.1)$$

where ζ_θ is isentropic relative vorticity, f the Coriolis parameter, g the gravity constant, and $\frac{\partial\theta}{\partial p}$ static stability. Moreover, PV is a preferred dynamic tracer for cyclones due to its conservation properties in an adiabatic and frictionless flow (Holton 2004). In the Northern Hemisphere, a strong positive PV anomaly in the upper troposphere that is not necessarily restricted to the tropopause induces a cyclone near that level that can, in turn, induce a positive anomaly and cyclone at the surface (Hoskins et al. 1985; Holton 2004; Hoskins 2015). Additionally, PV is useful as it conforms to the principle of invertibility, which establishes that the 3-dimensional wind and temperature fields are induced by the PV structure if relatively fast-moving waves are neglected (Hoskins et al. 1985; Hoskins 1997).

In this study, small scale isentropic potential vorticity maxima at the 320-K level (hereafter PV_{320}) at 6-hourly intervals are objectively tracked in DJF for 1980-2010 following the Lagrangian approach discussed in Hoskins and Hodges (2002). The method first identifies cyclones as PV_{320} anomalies that exceed 0.5 Potential Vorticity Units (PVU, where 1 PVU = 10^{-6} K m^2 kg^{-1} s^{-1}) on a NH polar stereographic projection, which helps to prevent latitudinal bias in the identification of cyclones at high latitudes (Sinclair 1997). The PV_{320} threshold of 0.5 PVU is significantly low to account for most possible storms: in this case about 296 cyclones per DJF season are identified that

satisfy the post tracking filters (discussed below). The 320-K isentrope is chosen as the level of analysis as it resides in the mid-upper troposphere near the upper-level jet stream (Fig. 2.1) where characteristics of cyclones are often identified (e.g., Hoskins and Hodges 2002). The PV_{320} anomalies are produced by applying a spherical harmonic analysis to the PV_{320} field and removing the background planetary scale waves with total wavenumbers less than or equal to 5 and reducing the horizontal resolution to T42 (128 longitudinal by 64 latitudinal points) to reduce noise. Additionally, a spectral taper is applied to the spectral coefficients to further reduce noise (Hoskins and Hodges 2002). This has been found to be a conservative but useful approach when examining fields that are dominated by a large scale background and are very noisy at high resolutions and focuses on the synoptic spatial scales of cyclones. The identified PV_{320} maxima are initially linked using a nearest neighbor method to form tracks and are then refined using a constrained optimization approach which swaps points between tracks to maximize the track smoothness (Hodges 1994, 1995). Constraints are applied adaptively for maximum propagation speed and track smoothness (Hodges 1999) suitably chosen for the extra-tropics. Following completion of the tracking, a filter is applied to retain only those cyclones that last at least 2 days and travel farther than 1000 km. These conditions act as spatial and temporal filters to remove short duration or semi-stationary eddies.

An additional filter is also applied to remove any weak storms with a maximum intensity smaller than a relatively low threshold T_{all} defined as:

$$T_{all} = \overline{PV_X} - 1.5 \times (PV_X)_{SD} \qquad (2.2)$$

18
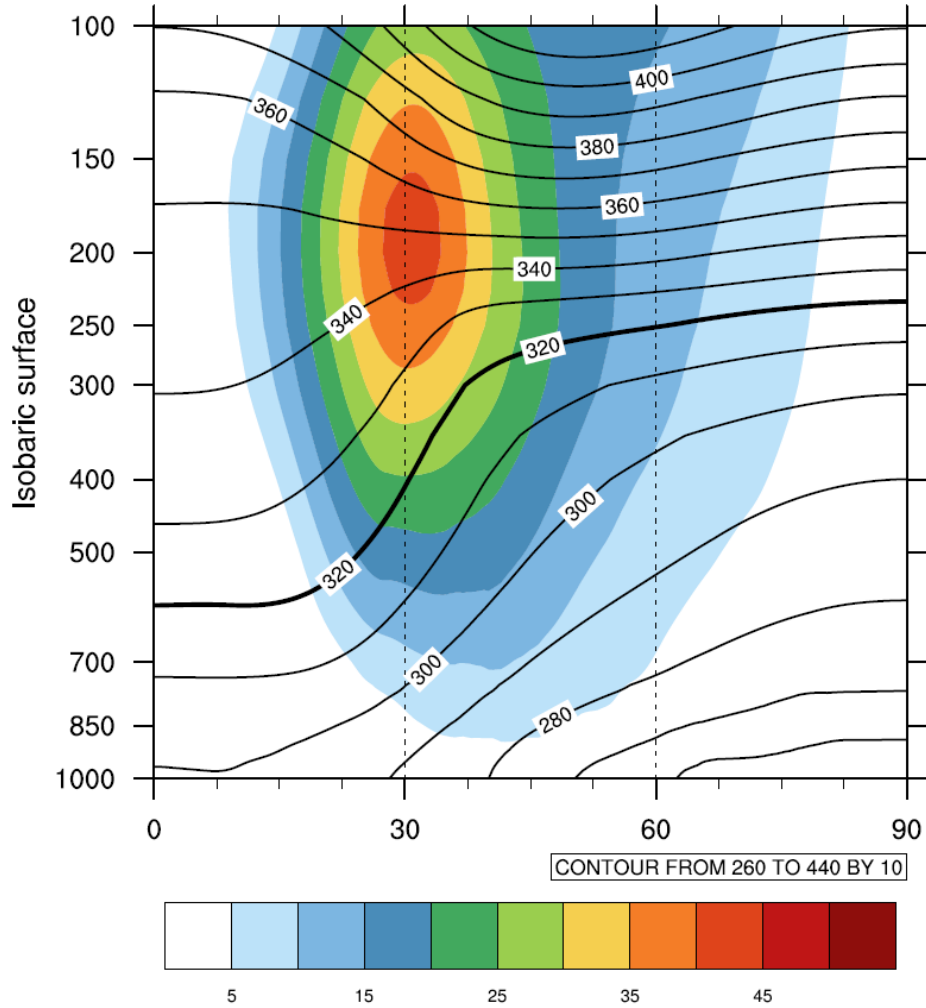
Figure 2.1: DJF mean zonal state in the Northern Hemisphere for 1980-2010. The mean zonal wind is shaded with 5.0 m s^{-1} intervals. Line contours indicate the vertical distribution of mean zonal isentropic surfaces at a 10 K contour interval. The bold black line highlights the θ=320 K surface on which the mid-latitude storm tracks are defined.

where T_{all} refers to the threshold to identify all storms, $\overline{PV_X}$ is the maximum PV intensity averaged for all identified cyclones in the NH, and SD is the standard deviation. Storms that adhere to these criteria shape the *all-storm tracks.* Considering that extratropical storms at 320 K in the NH have an average PV_x = 3 PVU and a standard deviation $(PV_x)_{SD}$ = 1.3 PVU, storms that shape the all-storm tracks achieve maximum PV that exceeds a low threshold of 1 PVU, following Eq. (2.2). As apparent

in Fig. 2.2, this threshold captures weak cyclogenesis and provides a large number of cases for the analysis: on average, about 259 storms per season that satisfy the post tracking filters comprise the extratropical NH all-storm tracks.

Strong-storm tracks represent storms with maximum PV intensities that exceed a threshold of:

$$T_{str} = \overline{PV_X} + 1 \times (PV_X)_{SD} \tag{2.3}$$

where T_{str} refers to the threshold for strong storms and all other terms were defined for Eq. (2.2). The values used to compute T_{str} are the same for the storm tracks in both the Pacific and Atlantic regions, despite being calculated separately: storms in the Pacific and Atlantic Oceans have an average PV_x of 3.8 PVU with a standard deviation of 1 PVU, yielding T_{str} = 4.8 PVU as also noted in Fig. 2.2. Strong storms represent about 16% of all storms that develop in both regions and correspond to similar percentiles of the storm strength distribution in each basin. On average, 9 (6) strong storms per season develop in the storm track region over the Pacific (Atlantic) Ocean (Table 2.1).

The statistics of a large number of the cyclone trajectories describe the main properties of the Northern Hemisphere storm tracks, including the track density, genesis density, lysis density, and mean storm track intensity. Following Hoskins and Hodges (2002), the track density statistic is calculated by using a single point from each track nearest to each estimation point for each PV cyclone trajectory; the genesis

Table 2.1: Statistics for the DJF strong-storm tracks for (a) the entire Northern Hemisphere, (b) the Pacific storm track, and (c) the North American-Atlantic storm track. In (b) and (c), only strong storms that develop within the specified storm track domain are included. The first column shows the average number of strong storms per DJF, mean strong-storm intensity, and average maximum intensity of strong storms in the first, second, and third rows respectively throughout the entire 31-year period. The following two columns denote the values corresponding to the early and later periods, and the last three columns highlight the values for each decade.

(a) Northern Hemisphere	1980-2010	1980-1998	1999-2010	1981-1990	1991-2000	2001-2010
Average Number of Strong Storms per DJF	26	24	29	26	24	30
Mean Intensity (PVU)	3.8	3.8	3.8	3.8	3.8	3.8
Average Max Intensity (PVU)	5.4	5.4	5.4	5.4	5.4	5.4

(b) Pacific storm track	1980-2010	1980-1998	1999-2010	1981-1990	1991-2000	2001-2010
Average Number of Strong Storms per DJF	9	9	9	10	7	9
Mean Intensity (PVU)	3.8	3.8	3.8	3.8	3.7	3.8
Average Max Intensity (PVU)	5.3	5.3	5.3	5.3	5.3	5.3

(c) North American-Atlantic storm track	1980-2010	1980-1998	1999-2010	1981-1990	1991-2000	2001-2010
Average Number of Strong Storms per DJF	6	5	8	5	6	8
Mean Intensity (PVU)	3.8	3.8	3.8	3.8	3.8	3.9
Average Max Intensity (PVU)	5.3	5.3	5.3	5.3	5.3	5.3

density statistic uses the first detected positions of the cyclones; likewise, the lysis density statistic uses the last detected positions of the cyclones, and the spherical kernel density estimator method (Hodges 1996; Hodges 2008). The genesis and lysis densities are computed as probability density functions (pdf) and scaled to number densities (per unit area per month) by multiplying by the number of points and scaling to a unit area equivalent to a 5° spherical cap ($\sim 10^6$ km^2); in the case of the track density, the raw statistic is not a pdf but is scaled to number density by multiplying by the number of tracks and scaled to a unit area equivalent to a 5° spherical cap. The mean intensity statistic is calculated using a kernel regression estimator (Hodges 1996) applied to the PV intensity for all points along the cyclone trajectories. For both the density and regression estimators adaptive smoothing is used (Hodges 1996).
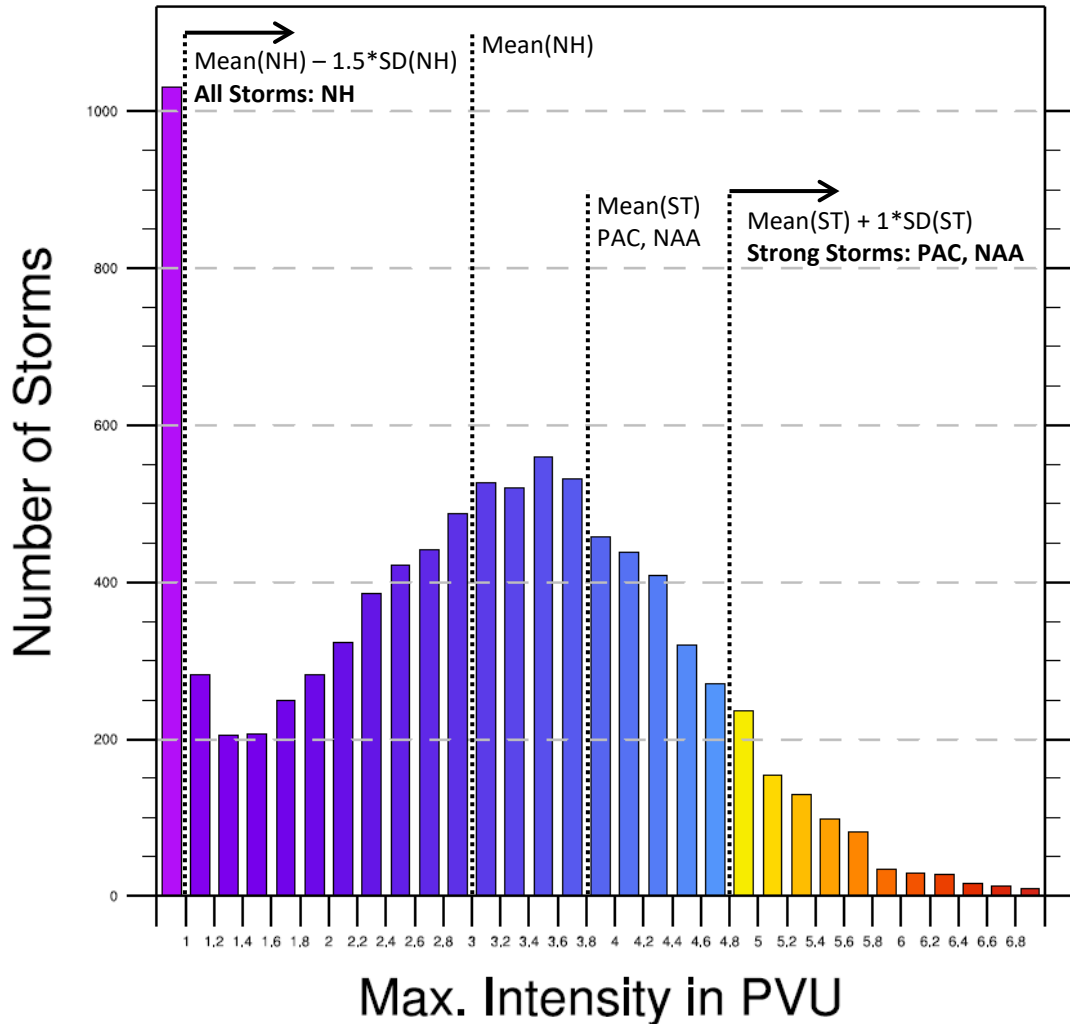
Figure 2.2: Histogram of all DJF storms binned by maximum intensity in the Northern Hemisphere for 1980-2010. Maximum intensity bins are shown in the x-direction at an interval of 0.2 PVU. Storms included in the all-storm track analysis have maximum intensities of 1 PVU or greater. Strong storms that follow the Pacific (PAC) or North American-Atlantic (NAA) storm tracks have maximum intensities of 4.8 PVU or greater and are highlighted in warm colors. In parentheses in the labels, NH signifies the statistics for the Northern Hemisphere, while ST indicates the statistics for the PAC and NAA storm tracks.

It should be noted that the methodology does not focus on individual events but rather interprets each climatological storm track as a wave packet that has its own properties and predictability. This perspective provides an overall sense of where winter storms tend to develop and intensify, and where related damages are more likely to occur.

Sensitivity tests were carried out to assess the robustness of the results in relation to (a) the isentropic level of the analysis on which to describe the storm tracks and (b) the PV intensity threshold, used for the initial identification, above which to consider a cyclone. An analysis of storm tracks on different isentropic surfaces (Fig. 2.3) resulted in the choice of the 320-K isentrope (Fig. 2.3b) as it is a good intermediate level on which the storm track features best correspond with previous studies (e.g., Hoskins and Hodges 2002). Isentropic PV above 320 K (e.g., PV at 330 K shown in Fig. 2.3a) poorly represents mid-latitude winter storm tracks, as the resulting storm tracks are of diminished size and magnitude relative to those described in previous studies. Further, the Pacific and Atlantic storm tracks at higher isentropic levels are no longer distinct as they merge into one zonal band of cyclone activity that crosses North America. Isentropic PV nearer the surface (< 320 K) (e.g., PV at 300 K shown in Fig. 2.3c) is also found to inadequately represent mid-latitude storm tracks. Lower potential temperatures are generally found closer to the Earth's surface and are more likely to "intersect" the ground (see Fig. 2.1). This confines the detection of cyclonic features on lower isentropic surfaces to the higher latitudes near cyclone "attractor" regions that exist over Japan and eastern Canada (Fig. 2.3c) near areas of large low-level baroclinicity (Fig. 2.4a). As such, lower mid-latitude storms are generally missed. Further, the entire Mediterranean storm track is no longer detected on lower isentropic levels. In addition, we examined the sensitivity of PV storm tracks to different minimum intensity thresholds above which to identify a cyclone; however, the structures and relative intensities of the storm tracks were found to be insensitive to the PV intensity threshold.

(a) PV track density at 330 K

(b) PV track density at **320 K**

(c) PV track density at 300 K
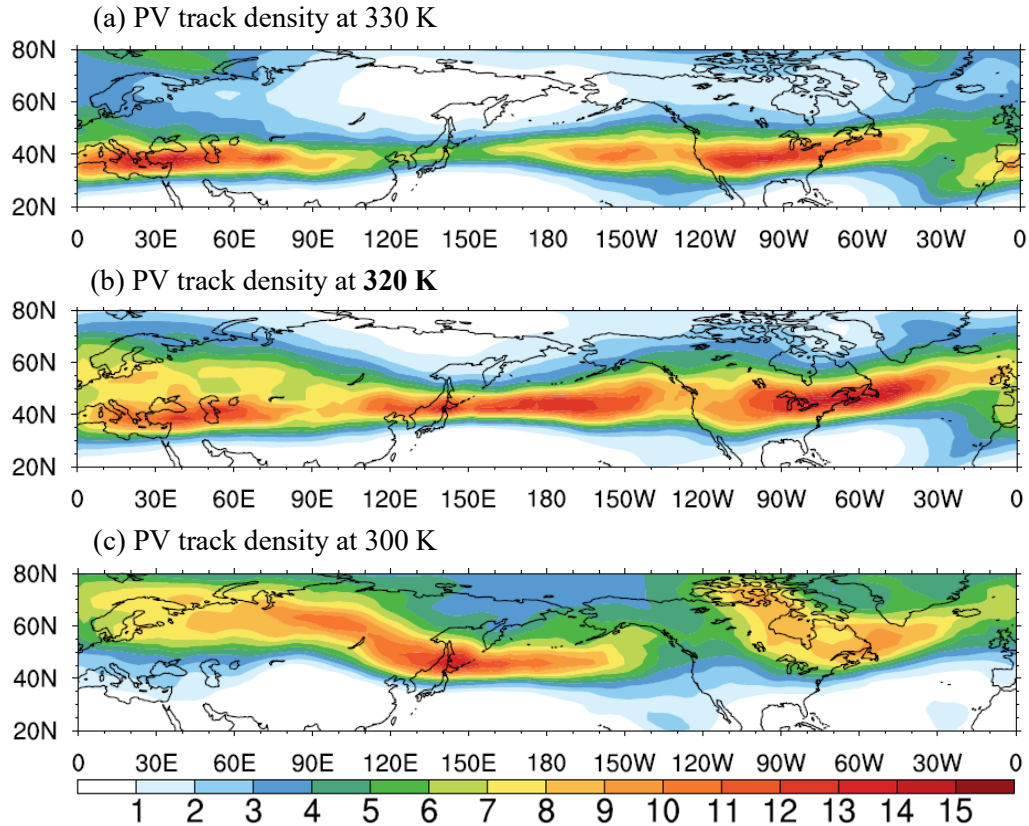
Figure 2.3: Storm track densities computed from all identified cyclones in the Northern Hemisphere DJF season for 1980-2010 on isentropic levels (a) 330 K, (b) 320 K, and (c) 300 K. All panels are shaded at intervals of 1 storm per 10^6 km^2 per month.

2.1.3 Relation of Storm Tracks to Diabatic Heating and Weather Distributions

In general, the storm tracks and diabatic heating in the corresponding regions act symbiotically. The presence of the heating aloft helps to maintain the baroclinicity needed to sustain cyclone activity, while the storms act to transport the heating downstream as they propagate along the storm tracks, thereby influencing the 3-dimensional diabatic heating distribution (Hoskins and Valdes 1990). With this co-dependence between the storm tracks and diabatic heating in mind, our study explores

the direct relationship between the heating and the storm tracks that influence North American weather. The diabatic heating is computed diagnostically at each level between 900 and 100-hPa as the residual in the thermodynamic equation (e.g., Hoskins et al. 1989; Barlow et al. 1998; Holton 2004):

$$\frac{\dot{Q}(x,y,p,t)}{c_p} = \frac{\partial T}{\partial t} + \mathbf{v} \cdot \nabla T + \omega \left(\frac{\partial T}{\partial p} - \frac{RT}{c_p p} \right) \qquad (2.4)$$

where $\dot{Q}/c_p$ is the residual heating (K day^{-1}), T the temperature, $\mathbf{v}$ the horizontal wind vector, ω the vertical wind in pressure coordinates, R the gas constant for dry air, c_p the specific heat for dry air at constant pressure, and p the pressure level. The residual is then vertically averaged to yield daily diabatic heating estimates of the free atmosphere.

To establish the relationship between the storm tracks and diabatic heating, near-surface winds, and precipitation, we follow a similar approach to that discussed in Hawcroft et al. (2012) and related literature. Each variable is considered to be associated with a cyclone if it is found within a particular circular area around the cyclone center. Precipitation from both reanalysis and observations is considered to be associated with a storm if it is found within a 12° circular area around each storm center, as this is a typical size of a storm precipitation footprint in the Northern Hemisphere winter (Hawcroft et al. 2012, 2016; Booth et al. 2018). The reanalysis precipitation is associated with storm centers identified at corresponding 6-hourly time steps, while the GPCP observations are associated with storm center positions at 12:00 UTC each day. Other variables have been reported to be greatly affected within the core of a cyclone represented by a 5° cyclone radius (Field and Wood 2007; Hawcroft et al. 2012, 2016),

and this is the choice we consider for diabatic heating and near-surface winds which are associated with the storm centers every 6 hours.

We also tested the sensitivity of storm-related weather to the size of the radius around the storm centers, and considered that storms tilt westward with height. At the time of a surface cyclone's maturity, the average horizontal displacement between a surface and upper air cyclone is about 200-300 km (e.g., Lim and Simmonds 2007), and this distance falls within the geodesic circular area around the PV_{320} cyclone centers we relate to near-surface weather. Further, near-surface weather related to storms tends to fall within a circular area of 1000 km around a surface cyclone center (Field and Wood 2007; Hawcroft et al. 2016; Booth et al. 2018), implying that the circular area around a PV cyclone that is horizontally displaced by <1000 km from a surface center can capture much of the storm-related weather at the surface. We expanded the circular area around all PV_{320} storm centers in order to account for the change in degree of vertical tilt throughout a storm's evolution and to detect all possible weather related to the surface cyclones. The expansion of the circular area yields relationships between the storm tracks and surface weather that are similar to those presented here (where the smaller areal sizes are used). Further, use of the larger area introduces uncertainty in the magnitude of storm-related weather due to the inclusion of too many extraneous grid points in the calculation. In addition, we examined PV_{320} cyclone centers that exist within +/- 24 hours of PV_{320} maxima in an attempt to isolate the impact of related surface cyclone development on surface weather, since surface cyclones tend to develop about 24 hours before maximum deepening which can occur before or after the upper air cyclone deepens (Sanders 1986; Lim and Simmonds 2007).

This analysis also yields similar results to those presented here, indicating that our choices of radial sizes reasonably represent the imprint of PV storm tracks on surface weather.

The storm track-related heating, winds, and precipitation fields in the figures are masked at grid points where the average number of storms falls below some very low number (in this case 0.5 storms per unit area per month) in order to highlight the mid-latitude main activity storm track regions.

2.1.4 Storm Loss Metrics

To examine the relation between strong-storm tracks and high wind speeds that could lead to potential damage at the surface, we employ a metric defined by Klawa and Ulbrich (2003). The metric is represented by a loss index that highlights areas where strong storms are likely to produce considerable damage by way of winds that exceed the local 98th percentile. Moreover, the loss index is proportional to the monetary value of loss induced by storm-related damages. Following Klawa and Ulbrich (2003),

$$\text{Loss Index} = \sum_{seasons} N_{pop} \left(\frac{v}{v_{98}} - 1 \right)^3 \text{ for } v \geq v_{98} \qquad (2.5)$$

where N_{pop} is the local population number, v the local wind speed related to the storm tracks, and v_{98} the local wind speed at the 98th quantile for 1980-2010. Use of this metric has led to the successful reproduction of storm loss in Germany at the end of the 20th century, in turn leading to a storm loss risk assessment for the nation in the 21st century (Klawa and Ulbrich 2003; Donat et al. 2011).

Precipitation and storm severity are inherently linked in part by condensational

heating and the enhancement of moisture flux convergence (Trenberth et al. 2003). To

our knowledge and unlike for winds, a general relationship between storm track-related

precipitation and damaging effects has not yet been established. We adopt a simple

approach in which we assume that areas that are most likely to experience loss are those

where the storm track precipitation exceeds the local 98th percentile.

2.2 *Dynamics of Storm Tracks*

2.2.1 Environment

The Eady Growth Rate used in this study combines information of the static

stability and the wind vertical shear for the layer 850-700 hPa, and it is frequently used

as a measure of baroclinic instability (Lindzen and Farrell 1980; Hoskins and Valdes

1990). The growth rate σ_B is defined by Eq. (2.6):

$$\sigma_B = 0.31f \left| \frac{\partial \mathbf{v}}{\partial z} \right| N^{-1} \tag{2.6}$$

where f is the Coriolis parameter, N the Brunt-Väisälä frequency, and $\frac{\partial \mathbf{v}}{\partial z}$ the vertical

wind shear. Following Hoskins and Valdes (1990), Fig. 2.4 shows that (i) regions of

large baroclinic instability are found over the western Pacific and Atlantic Oceans (Fig.

2.4a), and (ii) the largest region of low-level baroclinic instability lies poleward of the

200-hPa jet stream (Fig. 2.4b). Note that a region of high instability in the western

Pacific is zonal in orientation and parallels the strong 200-hPa jet. In the western

Atlantic, the region of lower troposphere instability also parallels the local upper-level

jet maximum with a SW-NE orientation that follows the eastern North American

coastline. A secondary region of baroclinic instability is found in the southeast of the Mediterranean Sea and is also poleward of the corresponding local upper-level jet maximum.

2.2.2 Physical Properties of the Storm Tracks

Winter all-storm track behavior as defined by PV at 320 K for 1980-2010 (as stated, those with $T_{all} \geq 1$ PVU, the threshold for all-storm tracks) is found to be consistent with that presented in Hoskins and Hodges (2002) and other studies. As an example, the all-storm track density statistic from this study and that defined by the ECMWF Reanalysis low-level relative vorticity for 1979-2000 in Hoskins and Hodges (2002) are shown alongside each other in Fig. 2.5. The PV_{320} all-storm tracks in this study (Fig. 2.5a) show three distinct regions of storm activity that maintain similar magnitudes and spatial orientations to those shown in the low-level relative vorticity storm tracks (Fig. 2.5b), supporting that PV_{320} is a useful dynamical tracer for winter storms.

The characteristics of the 1980-2010 strong winter storm tracks (as stated, those with $T_{str} \geq 4.8$ PVU) are depicted in Fig. 2.6. In Fig. 2.6a, the mid-latitude trajectories of individual strong storms converge into quasi-zonal bands of high cyclonic activity that form the strong-storm tracks. The number of individual strong storms per unit area, or strong-storm track density (Fig. 2.6b), is largest over the Pacific, North American-Atlantic (NAA), and Mediterranean regions. As expected, and in agreement with Wallace et al. (1988) and Hoskins and Valdes (1990), the three regions of strong-storm tracks are concentrated poleward of the upper-level jets where there is amplified
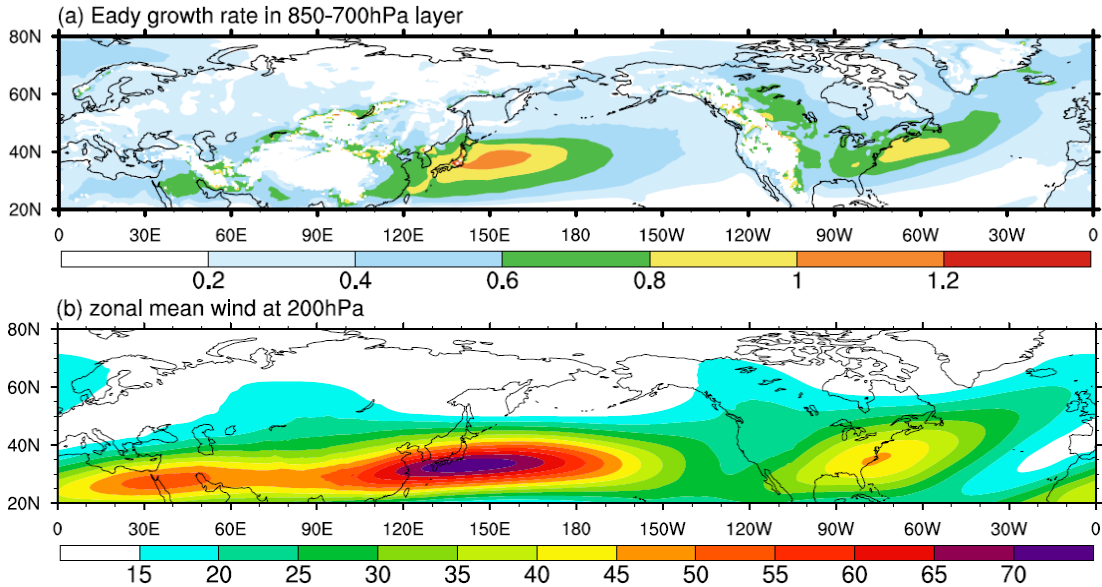
Figure 2.4: (a) 1980-2010 DJF Eady growth rate average for the 850-700 hPa layer. Values exceeding 0.2 day^{-1} are shaded at 0.2 day^{-1} intervals. Masked areas over the continents indicate regions where the land extends above the 850-hPa surface. (b) Zonal mean wind at 200-hPa. Values exceeding 15 m s^{-1} are shaded.

cyclonic shear and enhanced downstream development of baroclinic disturbances (Figs. 2.4b, 2.6b). Fig. 2.6b also highlights that the strong-storm track density (shades) resembles the track density for all winter storms (contours). This is particularly evident over the North Atlantic where the NAA storm tracks for both strong storms and all storms extend northeastward from central North America into the higher latitudes near Iceland.

The mean intensity statistic denotes the average strength of the strong-storm tracks identified in DJF (Fig. 2.6c). The strong-storm tracks are most intense where the corresponding track densities are highest: the eastern North Pacific and western North Atlantic Oceans, and the Mediterranean Sea. The Pacific strong-storm track intensity (shades) shows an eastward shift relative to the corresponding all-storm track
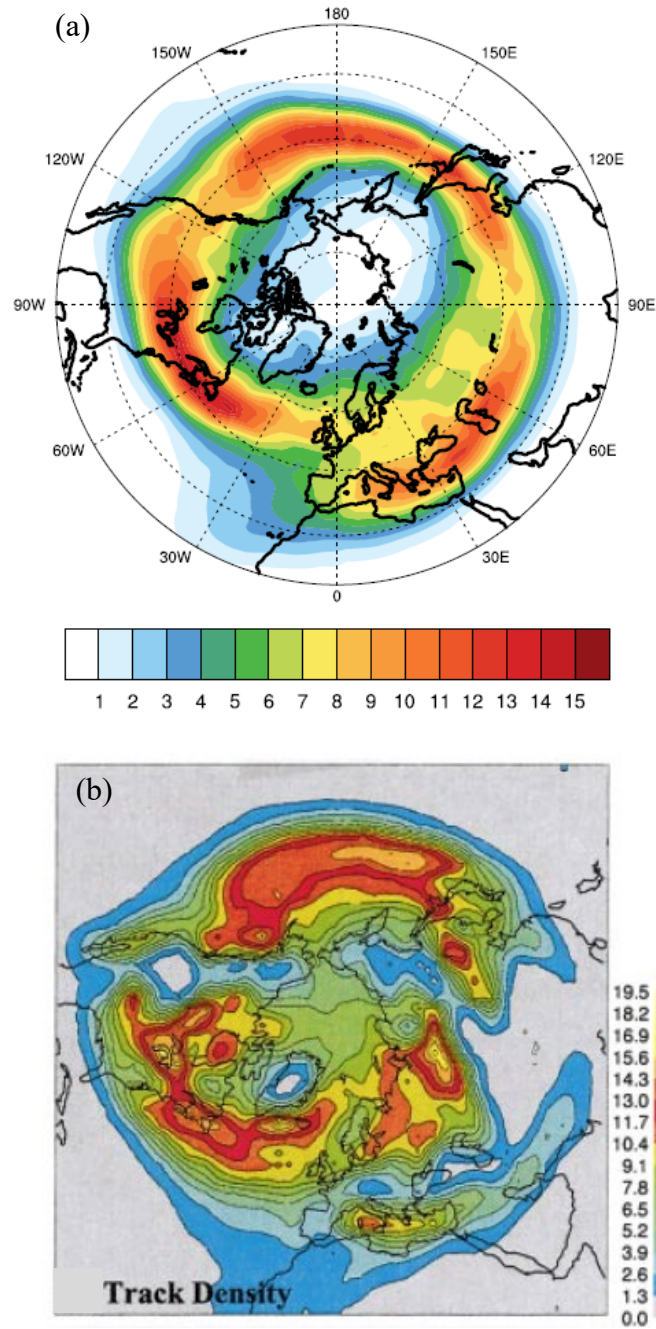
Figure 2.5: NH DJF track density for positive features in (a) potential vorticity at 320 K, and (b) relative vorticity at 850 hPa. Units are storms per 10^6 km^2 per month. Panel (a) corresponds to the all-storm track density for 1980-2010 in CFSR examined in this study. Panel (b) corresponds to Fig. 6b from Hoskins and Hodges (2002) that analyze storm tracks in ECMWF Reanalysis for 1979-2000.
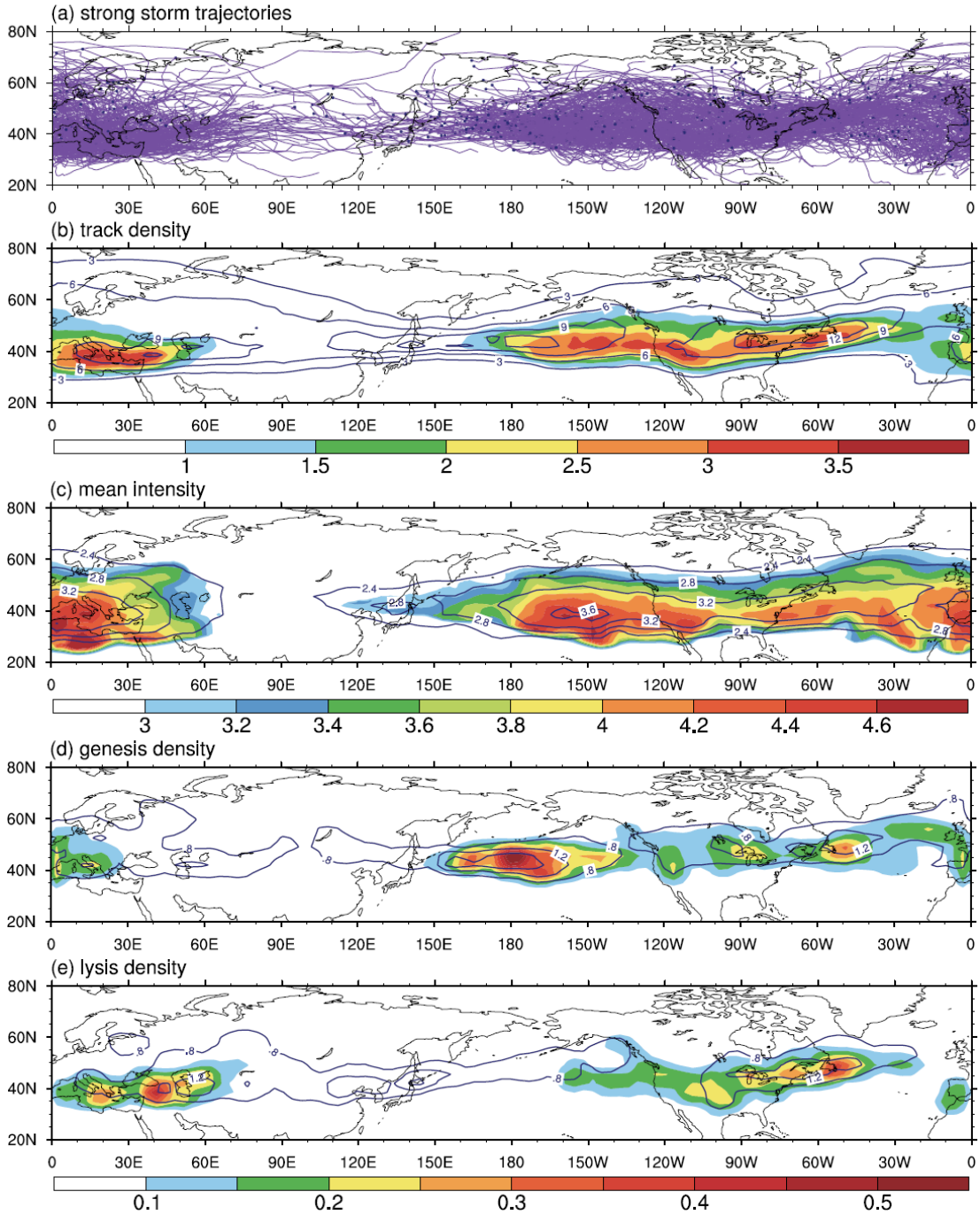
Figure 2.6: Storm track statistics in the Northern Hemisphere DJF season for 1980-2010. All-storm track properties are depicted in contours, while the strong-storm track properties are shaded. (a) Individual trajectories of strong storms; (b) Track density for all-storm tracks (contours at intervals of 3.0 storms per 10^6 km^2 per month) and strong-storm tracks (shaded at intervals of 0.5 storms per 10^6 km2 per month); (c) Mean intensity of all-storm tracks (contour intervals of 0.4 PVU) and strong-storm tracks (shaded at intervals of 0.2 PVU); (d) cyclogenesis density for all-storm tracks (contours at intervals of 0.4 storms per 10^6 km^2 per month) and strong-storm tracks (shaded at intervals of 0.05 storms per 10^6 km^2 per month); (e) as (d) but for cyclolysis.

(contours). The substantial increase in the strength of strong storms towards the eastern Pacific Ocean is indicative of their potential destructive power as they move eastward and hit the North American west coast. Unlike the Pacific track, the NAA strong-storm track retains its high intensity across its respective ocean basin. This suggests that the colocation of the low-level baroclinic zone with the highly active NAA strong-storm track facilitates the invigoration intense storms in the western Atlantic; in turn, the storms act to reinforce the intensity of the storm track as they propagate across the ocean.

Figs. 2.6d-e illustrate the general temporal evolution of strong storms (shades) that follow the storm tracks. The genesis density statistic in Fig. 2.6d highlights regions of cyclogenesis, i.e., the location of the strong storms' initial development. Regions of strong-storm dissipation are represented by the lysis density statistic (Fig. 2.6e). Corresponding characteristics of the all-storm tracks are also shown by contours in Figs. 2.6d-e to display the similarity in behavior between the all-storm and strong-storm tracks.

Strong storms that can affect North American weather tend to develop in small groups near low-level baroclinic zones westward of where the storm tracks peak in intensity (Figs. 2.4a, 2.6d). The storms propagate eastward and become strongest over the eastern North Pacific and western North Atlantic Oceans (Fig. 2.6c). As they continue to move eastward the strong storms tend to decay (Fig. 2.6e), in part as they encounter high orography and become disorganized and either dissipate or reorganize leeward of the orography and reinvigorate (Fig. 2.6d-e). Fig. 2.6d also shows and supports that strong storms, e.g., intense winter nor'easter storms, which in part are

33

influenced by heat fluxes over the Gulf Stream, tend to develop over the western North Atlantic Ocean near the northeastern United States (Kuo et al. 1991; Davis and Dolan 1993; Yao et al. 2008).

In the analysis of strong-storm tracks that influence North American weather, it is desirable to take into account the corresponding patterns of diabatic heating for the atmospheric column, following Eq. (2.4). The distribution of positive heating rates in the NH winter is influenced by the distribution of the warm Kuroshio and Gulf Stream currents in the western North Pacific and North Atlantic Oceans, respectively, and by the zonal asymmetry of the land-ocean distribution (Brown 1964; Geller and Avery 1978; Wei et al. 1983). For instance, cooler westerly continental winds that blow across the warmer western ocean currents promote significant sensible heat fluxes near the surface and the rising of warm moist air. This tends to lead to a reduction in static stability (i.e., an increase in baroclinic instability) and increased vertical development and the generation of baroclinic cyclones aloft (Hoskins and Valdes 1990; Magnusdottir et al. 2004). The cyclones then redistribute the heating through latent heat release as they propagate downstream.

The residual diabatic heating climatology for NH DJF shows positive heating rates in the western North Pacific and western North Atlantic Oceans (Fig. 2.7a). This pattern resembles the low-level baroclinic instability (Figs. 2.4a) that is maintained by the low-level flow off the continents over the warm western boundary currents that protrude poleward into the cool ocean waters. The climatological values of diabatic heating rate are in agreement with those shown in Chan and Nigam (2009) and Chang (2009). The heating related to the all-storm tracks (Fig. 2.6b) exhibits similar values to
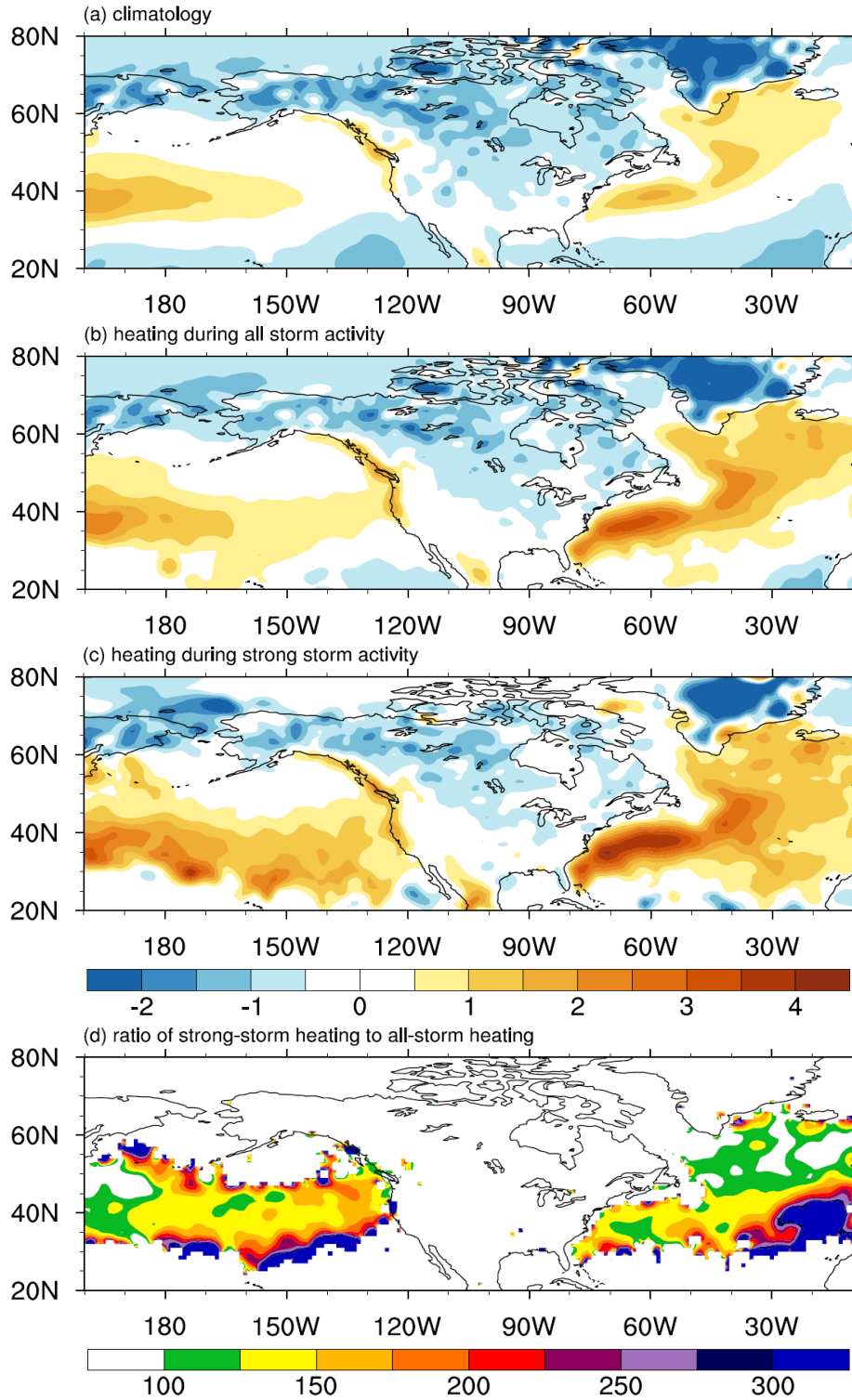
Figure 2.7: DJF 1980-2010 vertically averaged 900-100 hPa diabatic heating (a) climatology, (b) during all storm activity, and (c) during strong storm activity, all shown at an interval of 0.5 K day^{-1}. (d) The ratio (%) of the strong-storm diabatic heating to the all-storm diabatic heating. Shaded regions in (d) indicate areas where the all-storm and strong-storm heating rates are positive.

the climatology in the central North Pacific Ocean, suggesting that the storm track largely contributes to the diabatic heating distribution over that part of the basin. In contrast to the climatology, the all-storm heating in the eastern North Pacific and in the North Atlantic Ocean increases in strength and spreads across the oceans in the mid-latitudes (Fig. 2.7b). The heating in both storm track regions is even more intense during strong storm activity (Fig. 2.7c). For instance, in the North Pacific, the strong-storm track-related heating further intensifies in the east where the Pacific strong-storm track is most intense, and it remains strong as it spreads up and down the west coast of North America. In relation to the NAA strong-storm track, the heating is most intense over the western North Atlantic and remains strong across the ocean where the storm track retains its high intensity.

Fig. 2.7d presents the ratio of the positive heating rates related to strong-storm activity to the positive heating rates related to all-storm activity. This comparison between the strong-storm and all-storm heating reveals that the heating related to the strong-storm tracks is at least 25% more intense than the heating related to the all-storm tracks over the Pacific and Atlantic Oceans where the storm tracks are strongest. Moreover, in the lower mid-latitudes, the strong-storm heating is up to 3 times more intense than the all-storm heating.

Deep convection associated with strong-storm activity is obtained directly as a diagnostic from the CFSR database (Fig. 2.8). High positive heating rates associated with deep convection are found in each of the strong-storm track regions and are highest where the storm tracks are most intense (see Figs. 2.6b-c). Furthermore, the heating from deep convection largely resembles the diabatic heating distribution in the
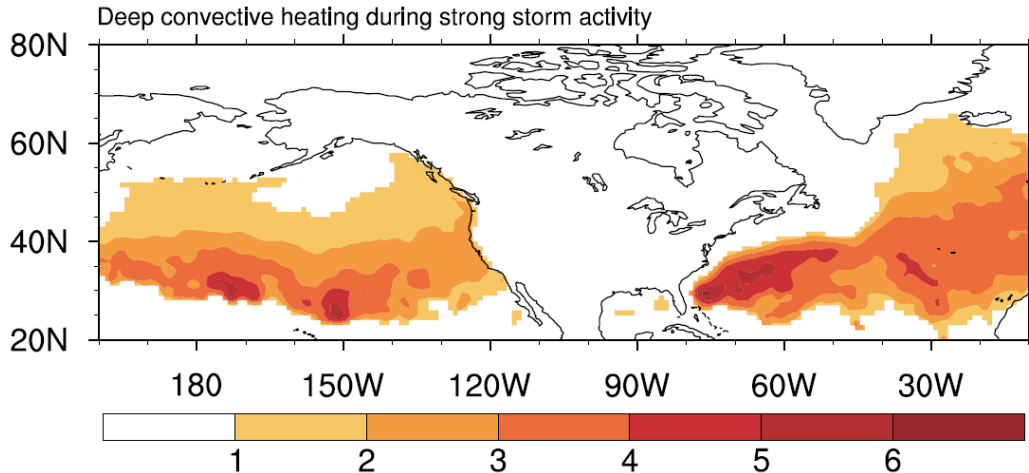
Figure 2.8: Mean heating from deep convection during strong storm activity averaged between 900-100 hPa in the Northern Hemisphere DJF season for 1980-2010. Contour interval is 1.0 K day^{-1}. Regions outside the all-storm track regions are masked out.

strong-storm track regions (Figs. 2.7c), suggesting that deep convective processes dominate the strong-storm tracks in the free atmosphere.

The strong-storm diabatic heating in the western North Atlantic corresponds with the higher track density and is more intense than the heating in the North Pacific (Figs. 2.6b, 2.7c). Similar relationships are found in the deep convection associated with strong-storm tracks (Fig. 2.8). Along with the local SW-NE oriented low-level baroclinic zone and upper-level jet near the east coast of North America (Fig. 2.4), the stronger heating in the Atlantic promotes greater instability and increased cyclonic activity (Fig. 2.6b), supporting the findings of Brayshaw et al. (2009).

2.2.3   Strong-Storm Track Variability

It has been found that winter storm track activity and intensity have increased over the past several decades, in particular in the Atlantic storm track region (Chang

and Fu 2002, 2003). In fact, storm tracks are modulated in part by large-scale circulation patterns. For example, meridional shifts in the storm tracks are linked to the intensification and relative locations of the jet stream as well as low-frequency modes of variability (Chang 2001; Chang and Fu 2002, 2003; Brayshaw et al. 2008; Ma and Zhang 2018). Additionally, previous studies have analyzed the response of storm track variability to future anthropogenic climate change scenarios and found that the storm tracks shift poleward and intensify due in part to poleward shifts in mid-latitude baroclinic regions (e.g., Ulbrich and Christoph 1999; Yin 2005; Salathé 2006). In this section we examine the inherent variability that exists in the strong-storm tracks and related diabatic heating in DJF for 1980-2010. The results are included to supplement our analysis of strong-storm track behavior in Section 2.2.2, although they have no bearing on the conclusions of this thesis.

Figure 2.9 presents maps of standard deviations and trends over time of the strong-storm track properties and related diabatic heating (colors) overlaid with contours of the corresponding 1980-2010 DJF averages (where the contoured strong-storm means are identical to those presented in Fig. 2.6). (Similar results are found for the all-storm tracks and are not shown.) The standard deviations represent the average variability observed for 1980-2010, and positive (negative) values in the corresponding trends denote an average increase (decrease) in magnitude over the course of the period.

The SD of the strong-storm track density (Fig. 2.9a) is high across the mid-latitude strong-storm track regions. The corresponding linear trend of track density (Fig. 2.9b) is positive and statistically significant ($p < 0.05$) in the northeast Pacific Ocean poleward of the mean track density maximum (contours). This suggests the
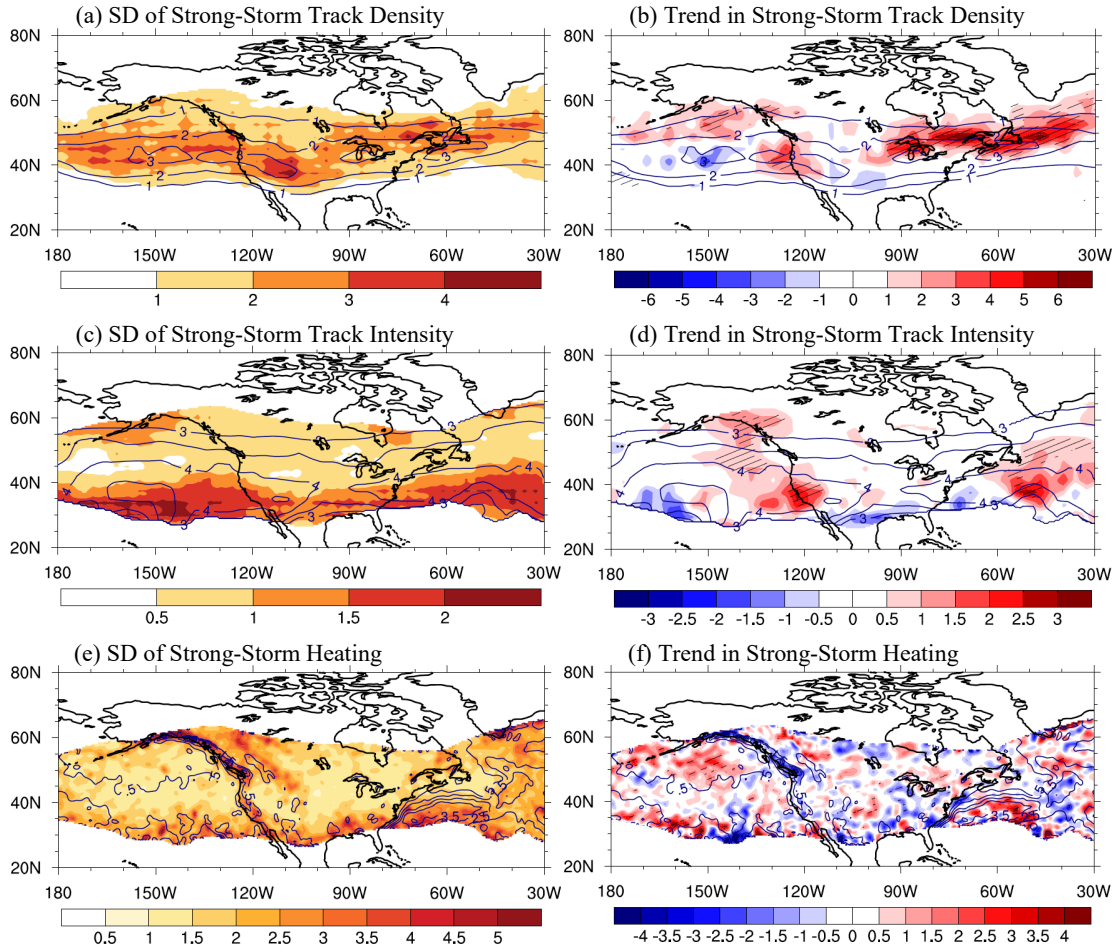
Figure 2.9: Variability in strong-storm tracks during DJF for 1980-2010. Colors indicate (left column) (a,c,e) standard deviations (SD) and (right column) (b,d,f) temporal trends over the course of the 31-year period. Labeled contours indicate the 31-year means for (top row) track density in units of storms per 10^6 km^2 per month, (middle row) mean intensity in units of PVU, and (bottom row) residual diabatic heating in units of K day^{-1}. Hatched marks in panels (b,d,f) indicate statistical significance ($p < 0.05$). Areas outside of the main activity strong-storm track regions are masked.

strong-storm activity tends to shift poleward over the northeastern Pacific region. This is accompanied by additional increases in Pacific strong-storm activity near the North American west coast. Higher statistically significant positive trend values in the NAA storm track region indicate that winter strong-storm activity has largely increased in the region over the 31-year period. The results are in agreement with Chang and Fu (2003) that found a considerable increase in Atlantic storm track activity over time.

The SD of mean PV_{320} intensity (Fig. 2.9c) is highest in the lower mid-latitudes of the main activity storm track regions. However, statistically significant trends in PV_{320} intensity (Fig. 2.9d) indicate that strong storms strengthen poleward of the SD maxima over the eastern oceans where local increases in storm track activity are observed (Figs. 2.9a,b).

The residual diabatic heating related to the strong-storm tracks is largely variable in the lower mid-latitudes of the strong-storm track regions and along the North American west coast (Fig. 2.9e). Statistically significant positive trend values associated with strong-storm heating (Fig. 2.9f) are found in the northeastern North Pacific Ocean where the track density tends to increase. This suggests that poleward shifts in the magnitude of strong-storm track-related heating induce enhanced baroclinicity and eddy activity to the north that in turn act to shift the storm track poleward, supporting the findings of Yin (2005) and Ma and Zhang (2018). In the Atlantic sector, positive trends in strong-storm heating are found over the western North Atlantic, suggesting increased diabatic heating that promotes greater instability and storm activity and intensification in the region (Figs. 2.9b,d), supporting the findings of Brayshaw et al. (2009).

2.3   *Surface Weather Related to the Storm Tracks*

2.3.1   Near-surface Winds

The relation between the storm tracks and near surface winds will be discussed next with the support of Figs. 2.10 and 2.11. Statistically significant wind speeds are highlighted by hatched marks in Fig. 2.10. In the absence of storm activity (Fig. 2.10a),

near-surface winds achieve magnitudes of about 4-6 m s^{-1} and resemble the pattern of the upper-level jet presented in Fig. 2.4b with primarily eastward and northeastward directions in the North Pacific and North Atlantic Oceans, respectively. Fig. 2.10b shows that for both the Pacific and NAA all-storm tracks (i.e., storms with $T_{all} \geq 1$ PVU), the near-surface winds intensify where the storm tracks are strongest and shift eastward in the eastern ocean basins. The winds associated with the strong-storm tracks (i.e., $T_{str} \geq 4.8$ PVU) presented in Fig. 2.10c show further intensification and a stronger eastward shift over the oceans. Wind speeds related to the all-storm tracks and strong-storm tracks are statistically significant throughout the storm track regions.

The increases in wind speed related to the all-storm tracks are better seen in Figs. 2.11a and 2.11b that depict the difference and ratio, respectively, between the all-storm related wind speeds and the no-storm wind speeds. Likewise, Figs. 2.11c and 2.11d depict the wind speed difference and ratio between strong-storm and no-storm events. In the North Pacific Ocean, wind speeds increase in the eastern basin where the all-storm track is strongest (Fig. 2.11a), particularly in the lower and higher mid-latitudes as the higher storm winds spread across the latitudes toward the edges of the storm track regions and achieve intensities over 5 times larger than winds in the absence of storm activity (Fig. 2.11b). The winds over the ocean further intensify during strong storm activity (Figs. 2.11c-d), helping to drive strong storms eastward to the North American coast. Moving to the Atlantic sector, wind speeds are found to intensify across the North Atlantic but particularly in the west and lower mid-latitudes as the storm winds shift southeastward. A secondary maximum is found in the northeastern

41
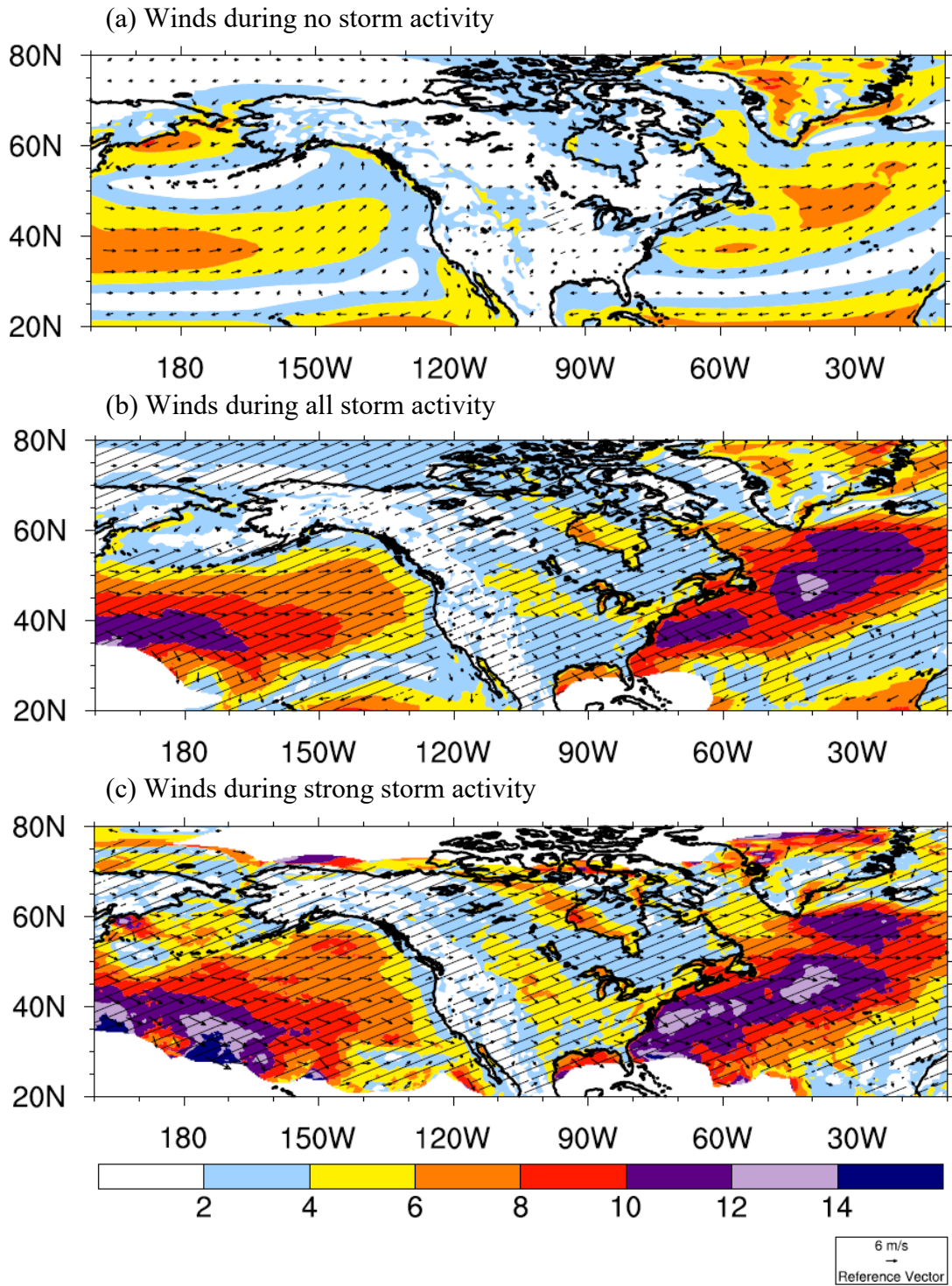
Figure 2.10: Mean near-surface wind distributions on the hybrid level 1 in DJF for 1980-2010 (a) during no storm activity, (b) during all storm activity, and (c) during strong storm activity. Shaded intervals are 2.0 m s^{-1}. Statistical significance ($p < 0.05$) is highlighted by hatched marks. In (b), areas are masked if found outside of the all-storm track regions (areas in white equatorward of 30°N). In (c), areas are masked if found outside of the strong-storm track regions (areas in white equatorward of 30°N or poleward of 70°N).
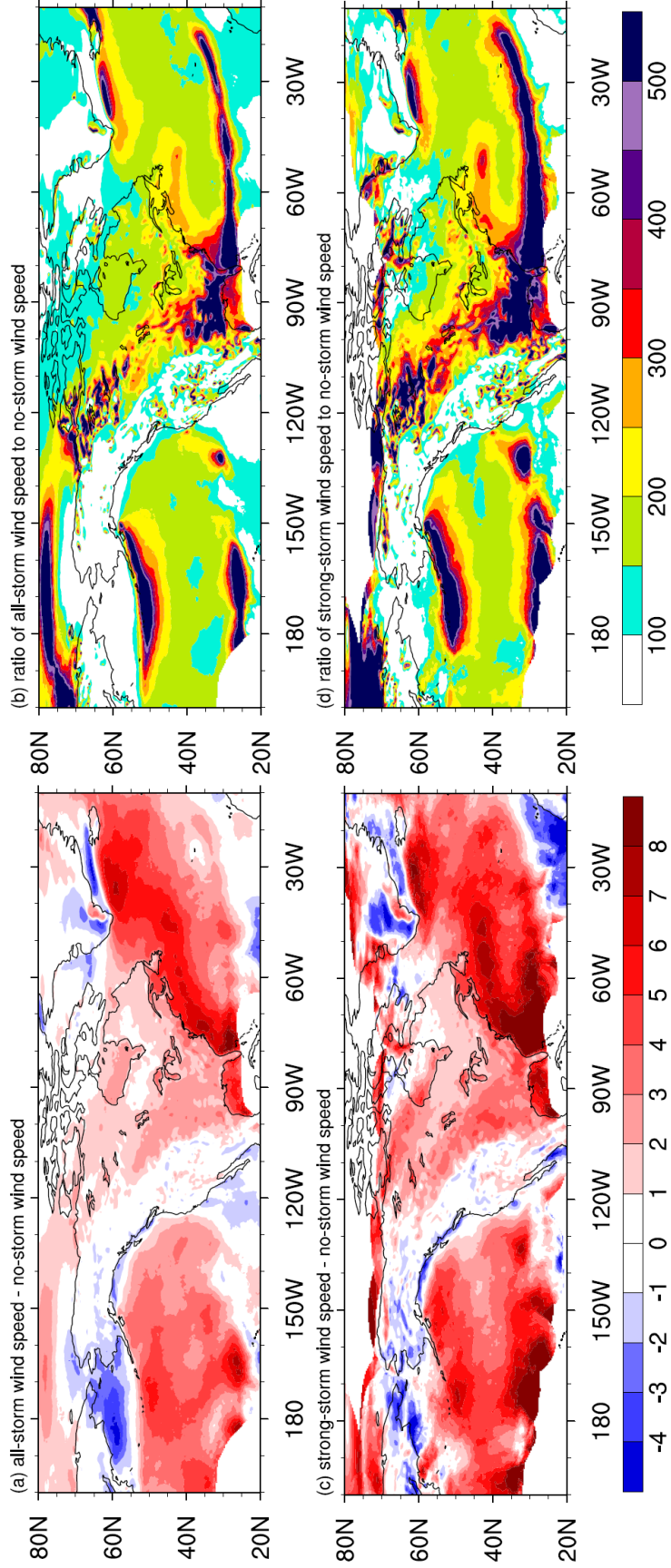
Figure 2.11: Wind speed comparisons based on Fig. 2.10. (a) Difference between all-storm wind speed and no-storm wind speed. (b) Ratio (%) of the all-storm wind speed to the no-storm wind speed. (c) Difference between strong-storm wind speed and no-storm wind speed. (d) Ratio (%) of strong-storm wind speed to the no-storm wind speed. In (a) and (c), shaded intervals are 1.0 m s⁻¹. In (b) and (d), values exceeding 100% are shaded with intervals of 50%. Regions outside the all-storm track regions are masked out

ocean basin where the westerly winds associated with the Icelandic Low augment the all-storm wind speeds (Figs. 2.11a-b; also seen in Fig 2.10c). During strong storm activity, wind speeds are further enhanced, specifically over the western ocean just offshore of North America and near the edges of the storm track regions as the storm winds shift southeastward and cover a wider latitudinal range (Figs. 2.11c-d). Over land, near-surface wind speeds related to the all-storm tracks increase east of the Rocky Mountains (Figs. 2.11a-b). Greater intensification in the wind speeds is evident during strong-storm events (Figs. 2.11c-d), specifically in the eastern US where the corresponding strong-storm track strengthens (see Fig. 2.6c).

Overall the strong-storm tracks leave greater imprints in the near-surface wind field in the North Atlantic than in the North Pacific (Fig. 2.10c), most notably just offshore of North America where maritime shipping and oil platforms are exposed. Increases in wind speeds near the coasts are also more pronounced in the western North Atlantic (Figs. 2.11c-d), consistent with the distributions of diabatic heating and deep convection that indicate greater baroclinic instability in the region (see Figs. 2.7c, 2.8). This would suggest that maritime operations in the western North Atlantic are more at risk to damage by way of near-surface winds associated with the strong-storm tracks.

The potential damage associated with extratropical strong-storm tracks over land in North America is assessed taking into account very high near-surface storm wind speeds, i.e., those that exceed the local 98th percentile (Fig. 2.12). Areas east of high orography most often experience strong-storm track-related near-surface wind speeds above the 98th percentile (Fig. 2.12a). As seen in Fig. 2.12b, these same areas also experience the most intense wind speeds related to the strong-storm tracks.
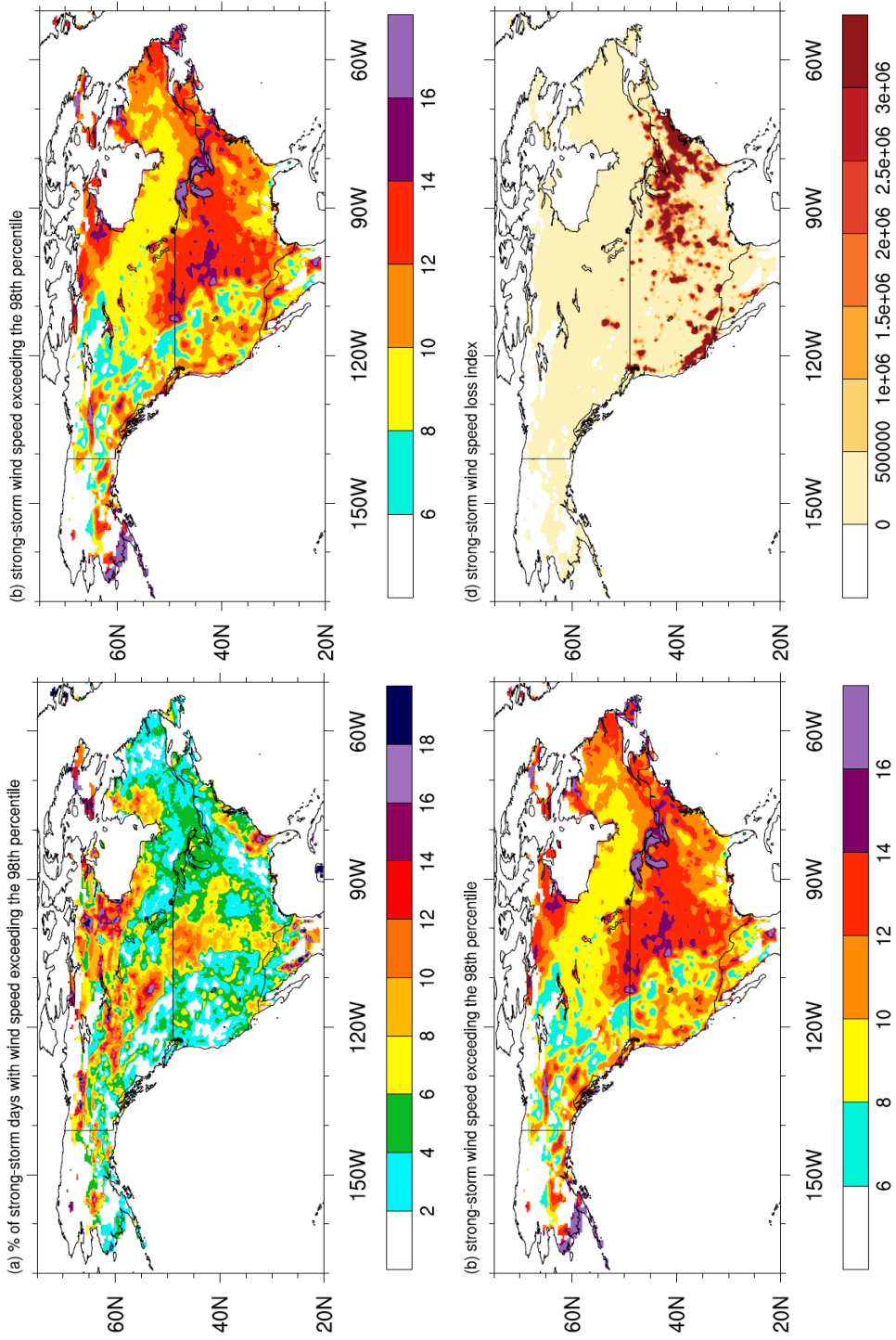
Figure 2.12: Analysis of intense near-surface wind speeds in DJF for 1980-2010 in North America. (a) Percent of strong-storm days with wind speeds exceeding the local 98th percentile. Shaded intervals are 2%. (b) Mean strong-storm wind speeds exceeding the local 98th percentile. Shaded intervals are 2 m s^{-1}. (c) 2010 population number with an interval of 1e4 people. (d) The strong-storm wind speed loss index with an interval of 5e5 and all positive values shaded.

Intense near-surface winds do not necessarily imply damage, unless they occur over populated areas. Fig. 2.12c presents the 2010 population number obtained from the LandScan Global Population Project following the methodology in Dobson et al. (2000), which is used for the calculation of the storm loss index presented in Section 2.1.4. Following Eq. (2.5), the storm loss estimate (Fig. 2.12d) highlights the regions that are most vulnerable to damages from very high storm winds. Within North America, these areas include the eastern US spanning from the Midwest to the east coast states and the southwestern US coast. A comparison with Fig. 2.12a reveals that storm wind loss in these areas is associated with up to 16% of strong storms in winter.

2.3.2   Precipitation

Figure 2.13 presents the relation between the storm tracks and CFSR surface precipitation. Figs. 2.13a and 2.13b show the precipitation distributions related to all-storm tracks and to strong-storm tracks, respectively. Hatched marks indicate statistical significance ($p < 0.05$). Consistent with the findings in Hawcroft et al. (2012), the all-storm and strong-storm precipitation maxima are found in the North Pacific and North Atlantic Oceans as well as along the west coast of North America. Secondary precipitation maxima are found in the southeastern United States. Overall the storm tracks leave greater imprints in the precipitation in the North Atlantic than in the North Pacific, possibly associated with the warmer waters that favor increased baroclinic instability and deep convection (see Figs. 2.4a, 2.8).

(a) CFSR PR during all storm activity

(b) CFSR PR during strong storm activity

(c) strong-storm PR - all-storm PR

(d) ratio of strong-storm PR to all-storm PR

(e) % contribution of strong-storm PR to all-storm PR

47
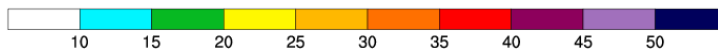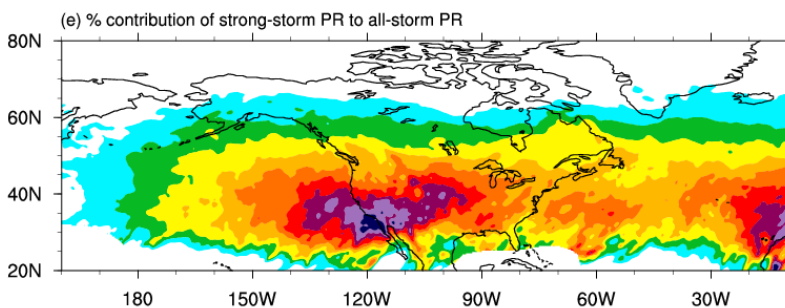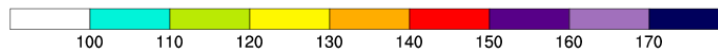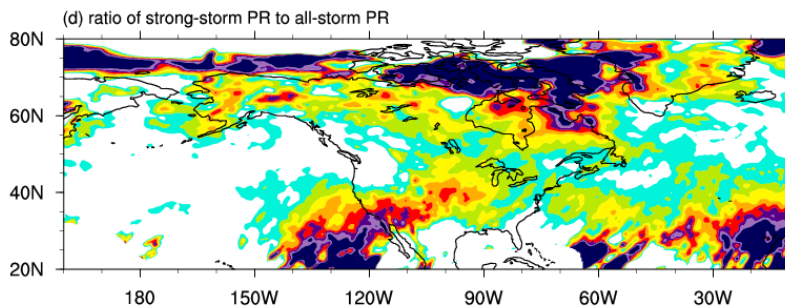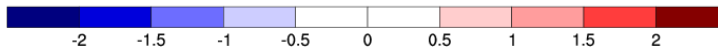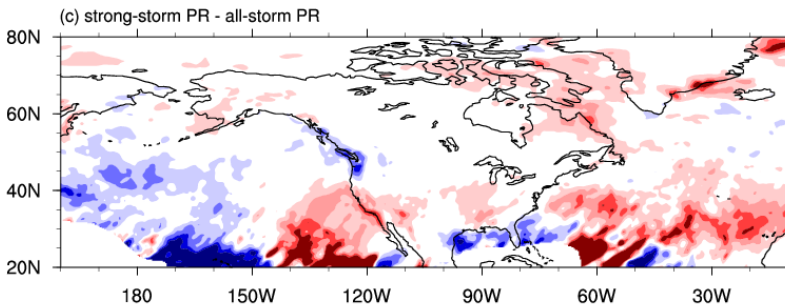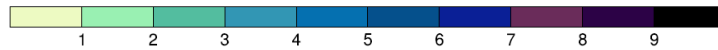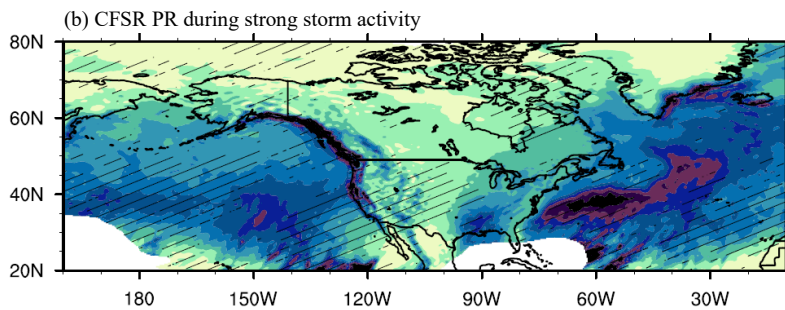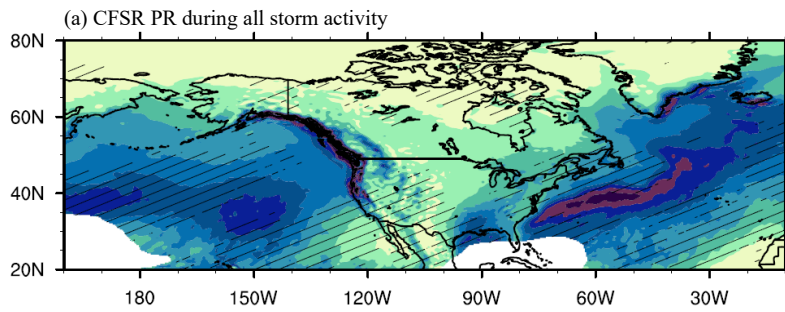
Figure 2.13: Analysis of CFSR precipitation rates (PR) during DJF for 1980-2010. (a) The mean precipitation during all storm activity, and (b) the mean precipitation during strong storm activity. In (a) and (b), shaded intervals are 1.0 mm day^{-1}, and hatched marks indicate statistical significance (p < 0.05). (c) The difference between strong-storm precipitation and all-storm precipitation with an interval of 0.5 mm day^{-1}. (d) The ratio (%) of strong-storm precipitation to all-storm precipitation with an interval of 10% and values exceeding 100% are shaded. (e) Percent contribution of strong storms to all-storm precipitation with an interval of 5%. For all panels, areas outside the all-storm track regions are masked out.

The difference and ratio between the strong-storm and all-storm track precipitation (Figs. 2.13c and 2.13d respectively) indicate the noticeable increases in precipitation that result from the fewer but stronger storms. These increases are evident over the oceans where the storm tracks are most intense. The percent contribution of strong-storm precipitation to the all-storm precipitation (Fig. 2.13e) shows that strong storms represent about 16% of all storms, yet they contribute 30-50% of the precipitation associated with the Pacific and NAA storm tracks (discussed further below).

As expected, precipitation associated with strong-storm activity in the eastern Pacific Ocean is more intense than that associated with all-storm activity (Figs. 2.13a-c). Precipitation increases during strong-storm activity towards the US west coast (Figs. 2.13c-d) and contributes to almost half of the all-storm precipitation in the region (Fig. 2.13e), exposing local fishing and other maritime operations to potential damage. Further increases are found as North America's land contrasts and orographic effects come into play: in the western US, increases of 50% are found during strong storm activity (Figs. 2.13d-e). This supports the notion that cyclones aloft lead to large accumulations of precipitation upstream of great mountain ranges and other high orography (Garreaud 2007). Farther east, strong-storm tracks are also associated with

more intense precipitation rates (Fig. 2.13c-d), contributing to over 30% of the all-storm precipitation (Fig. 2.13e). Orography in the northeastern United States can further boost the precipitation from strong storms. Similar results are found in the western North Atlantic where the enhanced strong-storm precipitation contributes to 30% of the all-storm precipitation (Figs. 2.13c-e).

The susceptibility to damage from strong-storm track-related heavy precipitation, i.e., precipitation rates exceeding the local 98th percentile, is investigated for North America (Fig. 2.14). The percent of strong-storm days with precipitation rates exceeding the local 98th percentile is presented in Fig. 2.14a. Distributions of heavy precipitation related to the all-storm and strong-storm tracks are shown in Figs. 2.14b and 2.14c, respectively. The heaviest precipitation related to the all-storm and strong-storm tracks is found along the west coast and in the southeastern US (Figs. 2.14b-c). The strong-storm tracks in particular likely play key roles in shaping the precipitation distribution in the southeastern US as the region experiences a relatively high percentage of strong-storm days with precipitation exceeding the 98th percentile (Fig. 2.14a). Along the west coast where there are fewer strong-storm days with heavy precipitation, it is likely that in addition to the strong-storm tracks, other factors such as topography and land-ocean contrasts may influence the distribution of heavy precipitation. In the central US, the high percentage of strong-storm days with heavy precipitation corresponds to low strong-storm precipitation rates (Figs. 2.14a,c). This indicates that in winter the region is relatively dry during strong-storm activity and is therefore less likely to experience loss associated with precipitation exceeding the 98th percentile.

(a) % of strong-storm days with PR exceeding the 98th percentile

(b) all-storm PR exceeding the 98th percentile

(c) strong-storm PR exceeding the 98th percentile

(d) strong-storm PR - all-storm PR

(e) % contribution of strong storm PR to all-storm PR
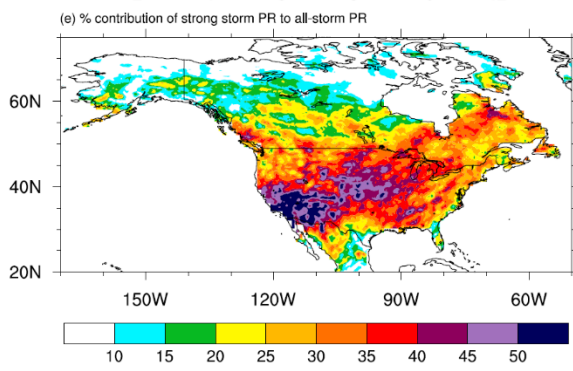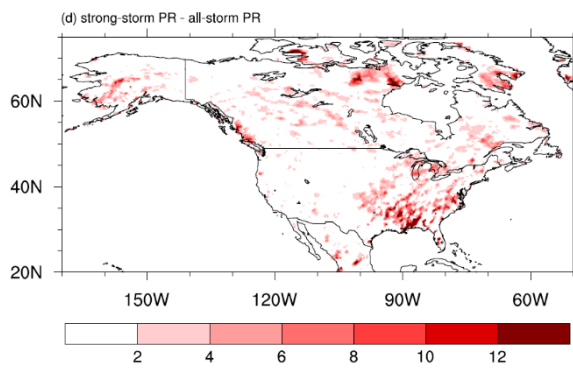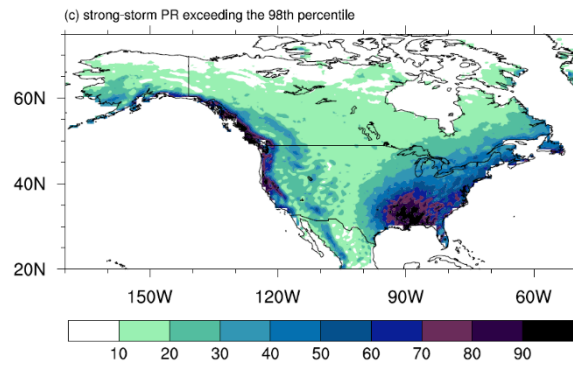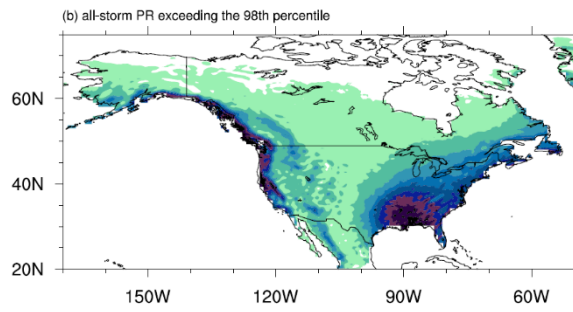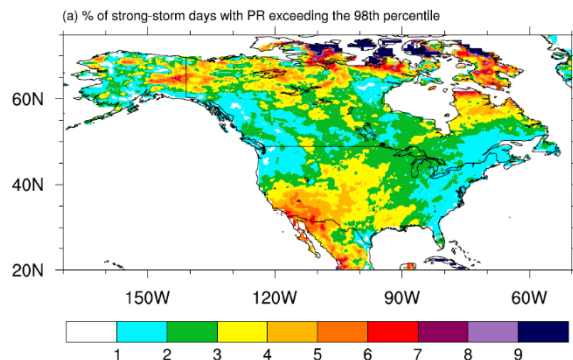
Figure 2.14: Analysis of CFSR intense precipitation rates (PR) in DJF for 1980-2010 in North America. (a) The percent of strong-storm days with precipitation exceeding the local 98th percentile. Shaded intervals are 1%. (b) The all-storm precipitation that exceeds the local 98th percentile. Shaded intervals are 10 mm day^{-1}. (c) As in (b) but for strong-storm precipitation. (d) The difference between strong-storm precipitation and all-storm precipitation. Shaded intervals are 2.0 mm day^{-1}. (e) Percent contribution of strong storms to all-storm precipitation with an interval of 5% and all values exceeding 10% shaded. Masking for all panels indicates areas where storm precipitation falls below the local 98th percentile.

Fig. 2.14d highlights the differences between the heavy strong-storm and all-storm track precipitation, and Fig. 2.14e presents the percent contribution of strong storms to all-storm precipitation that exceeds the 98th percentile. Substantial increases in precipitation rates during strong storm activity are found in the southeastern US and near the US east coast (Fig. 2.14d). Areas with the largest increases in heavy precipitation correspond to regions where strong storms contribute well over 30% of the all-storm precipitation (Fig. 2.14e), indicating their vulnerability to damage related to heavy strong-storm precipitation. The southeastern US is particularly vulnerable as precipitation is greatly enhanced during strong storm activity and contributes almost 50% of heavy all-storm precipitation in the region.

2.3.3   Reanalysis vs. Observed Precipitation

The precipitation blending algorithm in CFSR combines pentad CPC Merged Analysis of Precipitation (CMAP) and daily gauge precipitation analyses of varying spatial resolutions with background 6-hourly precipitation from the Global Data Assimilation System, GDAS (Saha et al. 2010b). The blending algorithm in CFSR is latitude dependent: in the tropics it tends to the CMAP analysis, in the mid-latitudes to a gauge analysis, and in the high latitudes to the model precipitation. Therefore, despite

CFSR including precipitation in its assimilation cycle, deviations from observations may occur. During 1999-2010, daily GPCP precipitation rates are considerably less intense than the daily reanalysis precipitation rates (not shown, but almost identical to the 1980-2010 reanalysis precipitation rates), particularly north of 60°N along the southern coastlines of Alaska and Greenland. As stated, this and other differences in winter precipitation between CFSR and GPCP may be due to multiple reasons, including the precipitation blending algorithm in CFSR but also inadequate satellite-driven estimations of precipitation at high latitudes included in the daily GPCP dataset (Bolvin et al. 2009).

We examine whether the relation of the strong-storm tracks with the daily reanalysis precipitation is maintained over North America when using precipitation derived from observations, that is, the daily precipitation from GPCP (Section 2.1.2.1). To this end, and despite that GPCP became available in 1996, the period 1999-2010 is examined to avoid any eventual spurious effects due to the 1998 discontinuity found in CFSR. Fig. 2.15 depicts the 1999-2010 daily precipitation distributions associated with the all-storm and strong-storm tracks for GPCP and relevant statistics. Figs. 2.15a and 2.15b respectively show precipitation associated with the all-storm and strong-storm tracks, with statistically significant precipitation rates found where the storm tracks are more intense (i.e., the eastern North Pacific and western North Atlantic Oceans and the eastern US). Comparison with the reanalysis precipitation (Figs. 2.15a-b) indicates that they share similar spatial distributions with local maxima over the eastern North Pacific Ocean, the western North Atlantic Ocean, the west coast of North America, and the southeastern United States. Nevertheless, the GPCP precipitation does exhibit weaker

(a) GPCP PR during all storm activity

(b) GPCP PR during strong storm activity

(c) strong-storm PR - all-storm PR, GPCP

(d) ratio of strong-storm PR to all-storm PR, GPCP

(e) % contribution of strong-storm PR to all-storm PR, GPCP
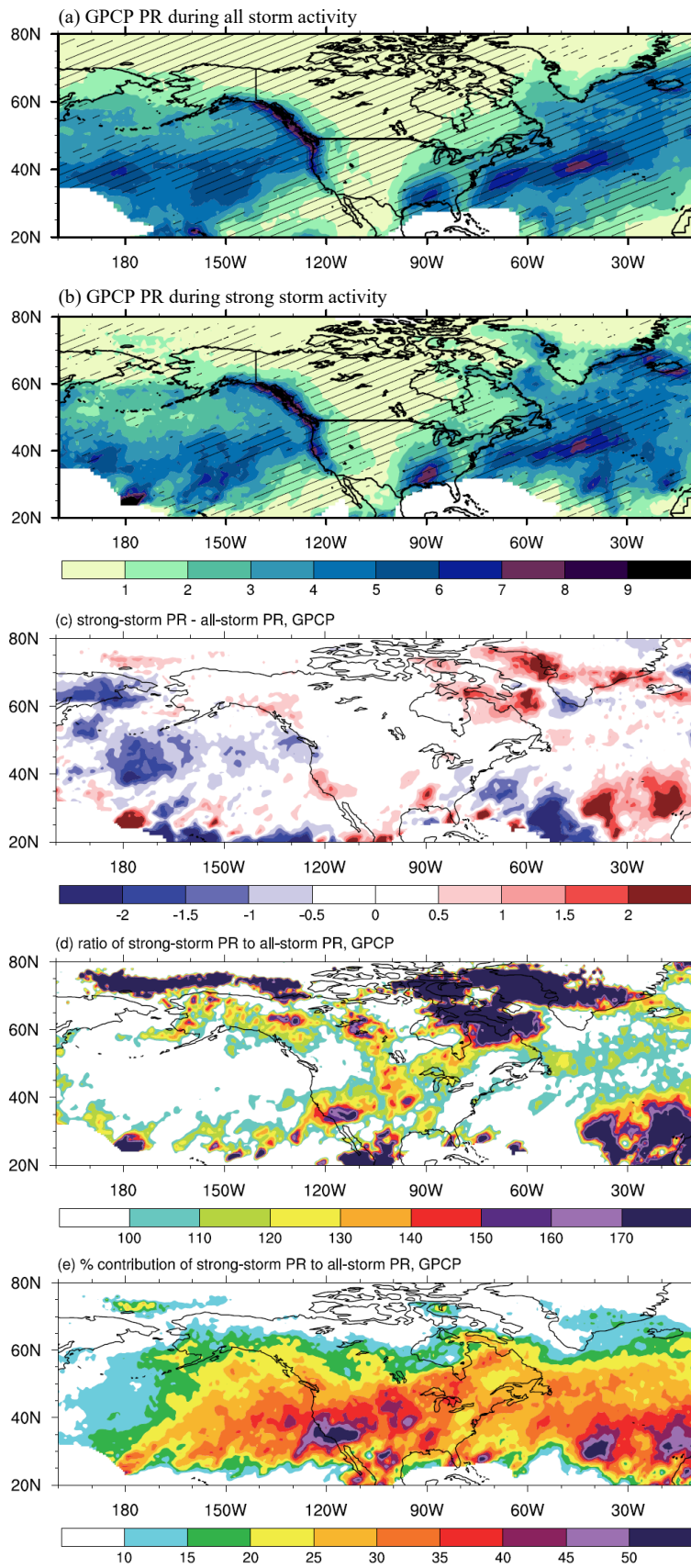
Figure 2.15: As in Fig. 2.13 but for GPCP precipitation for 1999-2010.

intensities, particularly in the Pacific and NAA storm track regions over the oceans. It is likely that the discrepancy in magnitude results from uncertainties in the oceanic observations of precipitation described in Adler et al. (2012).

Similar inferences can be noted in the difference (Fig. 2.15c) and ratio (Fig. 2.15d) of the observed precipitation related to the all-storm and strong-storm tracks. Differences in the reanalysis and observed precipitation metrics are noted particularly in the western North Atlantic Ocean where the observed precipitation related to the strong-storm tracks is shown to decrease (Fig. 2.15c). As already stated, the uncertainties in oceanic observations may play a role in this discrepancy. Over land, the observed precipitation differences and ratios in Figs. 2.15c and 2.15d show increases along the US west coast and in the southeastern US, consistent with the reanalysis (see Figs. 2.13c-d). The contribution of strong storms to the observed all-storm precipitation is presented in Fig. 2.15e. As depicted in the reanalysis (Fig. 2.15e), observations show that strong storms contribute over 30% of the all-storm precipitation over land and the oceans.

We also analyze the relation of the storm tracks with precipitation from GPCP that exceeds the local 98th percentile in North America (Fig. 2.16). Comparison of the reanalysis (Figs. 2.16b-e) and observational metrics reveal similarities despite the weaker GPCP intensities. The intense precipitation observed over the continent (Figs. 2.16a-b) corresponds qualitatively well with the reanalysis, in particular over the eastern US and along the North American west coast where the precipitation is further enhanced during strong-storm activity (Fig. 2.16c). According to Fig. 2.16d, the strong-storm tracks contribute over 30% of the all-storm precipitation that exceeds the 98th

percentile in regions where large increases are observed. The results indicate that the eastern US and west coast of North America are most prone to damage from heavy strong-storm precipitation, consistent with the findings using CFSR (Section 2.3.2). In general, we find that the reanalysis precipitation distributions related to the all-storm and strong-storm tracks are consistent with observations.

2.3.4   Storm Tracks and the 1998 CFSR Data Discontinuity

It was earlier stated that the reanalysis data show a discontinuity in the wind and precipitation fields in October 1998 thought to be due to the ingestion of data from ATOVS at the time. For instance, after 1998 there is a marked decrease in the intensity of low-level winds in the tropics and an increase in the global average precipitation (Chelliah et al. 2011; Wang et al. 2011). We investigate what impact, if any, this jump has on the results. To this end, the subset periods of 1980-1998 (hereafter, the early period) and 1999-2010 (hereafter, the later period) are analyzed. Table 2.1 (Section 2.1.2) displays relevant strong-storm statistics for the early and later periods to assess any change in the strong winter storm tracks that could impact the North American climate. The statistics are normalized to units per season and include the number of strong storms identified, the mean intensity of the strong storms, and the average maximum intensity reached by the strong storms during each period. Furthermore, each decade between 1980 and 2010 is examined to explore the possibility of a trend in the storm tracks regardless of the discontinuity.
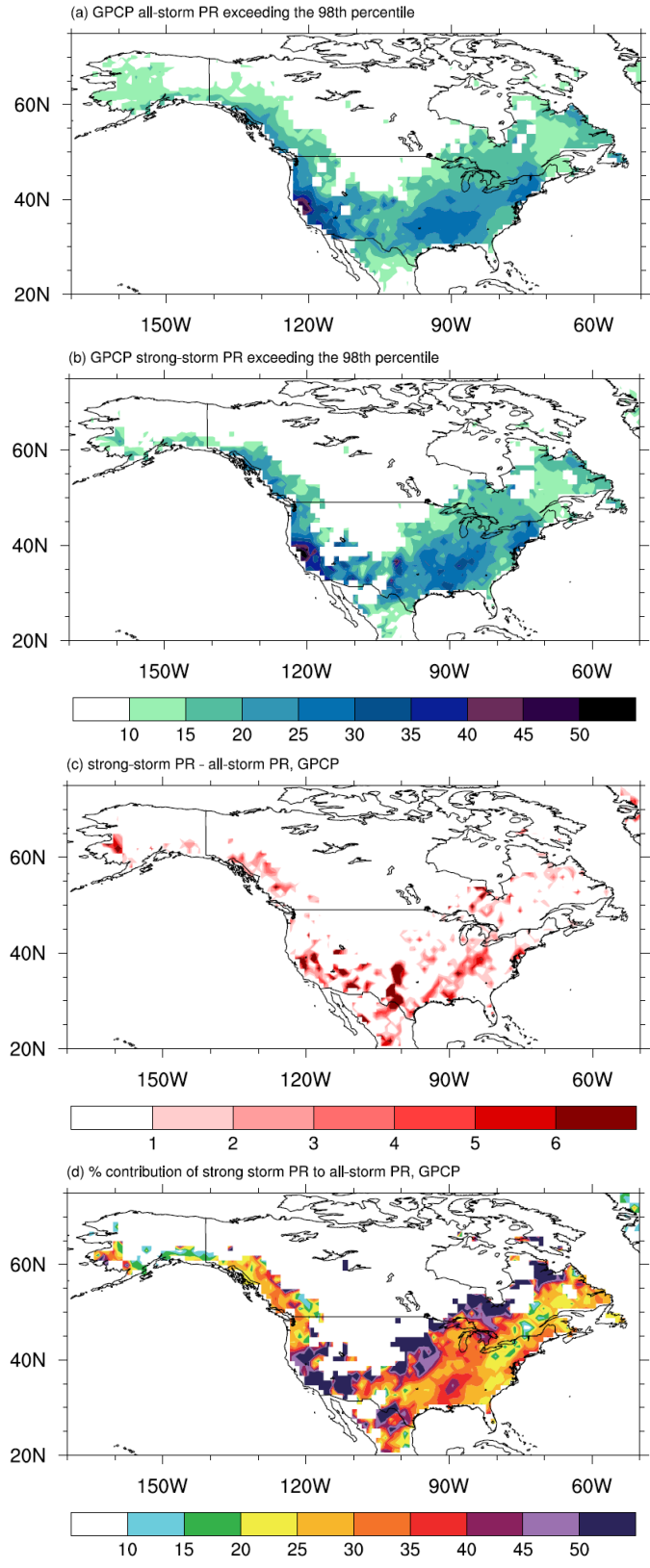
Figure 2.16: As in Figs. 2.14b-e but for GPCP precipitation for 1999-2010.

The more important feature noted in Table 2.1a is that no noticeable variations are found in the statistical means between the early and later periods and among the decades within 1980-2010. This indicates that the CFSR discontinuity does not significantly influence NH storm track behavior. Further, the effect of the discontinuity on the Pacific and NAA strong-storm tracks separately is investigated (Tables 2.1b-c), and it is found again that the behavior of each of the storm tracks is unaffected.

Similar results are found for the relation between the strong-storm tracks and the near-surface wind and precipitation distributions, and thus are not shown. Again, it was found that the 1998 CFSR discontinuity has little or no influence on the results corresponding to North American high impact weather. The wind speed associated with strong-storm tracks in each of these periods resembles that for the entire period and the same is true for the strong-storm precipitation. In summary, it is found that the CFSR discontinuity does not affect any of the features discussed here.

2.4   *Summary and Conclusions*

The behavior of strong winter storm tracks and their imprint on storm track-related weather in North America were discussed using 31 years of data from the Climate Forecast System Reanalysis and 12 years of precipitation data from the Global Precipitation Climatology Project. It was found that a data discontinuity in October 1998 in CFSR did not affect the behavior of the Northern Hemisphere storm tracks, nor did it influence their relation with North American winter weather. Storms were defined as maxima in potential vorticity and objectively tracked through their lifecycles

57

following a Lagrangian approach. Two types of storm tracks were discussed: the first one, "all-storm tracks", includes all extratropical cyclones whose maximum PV intensities exceed a low threshold of T_{all} = 1 PVU; the second type, "strong-storm tracks", only includes storms that achieve a maximum potential vorticity of at least T_{str} = 4.8 PVU, which is the value exceeding the mean intensity of storms comprising the Pacific and NAA storm tracks by one standard deviation. These more intense extratropical cyclones make up about 16% of all winter storms. Both all-storm tracks and strong-storm tracks were found to correspond well with those described in previous studies over the North Pacific and North Atlantic Oceans (as well as a weaker one over the Mediterranean Sea). In addition to detecting larger structures like the mean intensity of the storm tracks, and because of the dependence of PV on higher order derivatives, small-scale features of the storm tracks were easily differentiated, i.e., regions of cyclogenesis and cyclolysis. The cyclogenesis pattern showed that strong storms generally develop near low-level baroclinic zones. The cyclolysis pattern revealed that the strong storms tend to dissipate in the eastern North Pacific Ocean, the western North Atlantic Ocean near eastern Canada, and a secondary area over the central United States. The symbiotic relation between storm tracks and diabatic heating is evidenced by the large increases in diabatic heating associated with deep convective processes. The heating increases occur where the strong-storm tracks are most intense, in particular over the oceans.

We examined the average variability in the strong-storm tracks and related diabatic heating in winter to supplement our storm track analysis. The results suggest that strong-storm activity in the Pacific shifts poleward over time, with storm intensity

increasing in the east near the North American west coast. Further, statistically significant increases in strong-storm diabatic heating are also found over the northeastern North Pacific, suggesting that the poleward shift in heating induces similar shifts in baroclinicity that may contribute to the poleward shift in Pacific storm track activity (Yin 2005; Ma and Zhang 2018). Similarly, statistically significant increases in cyclone activity were found in the Atlantic sector on the poleward side of the NAA storm track. Local increases in strong-storm track-related heating were found over the western North Atlantic and likely play a role in enhancing strong-storm activity and strong-storm intensification in the region.

An analysis of the relation of strong-storm tracks to near-surface winds indicated that the winds shift eastward during strong-storm activity. Furthermore, the wind speeds increase over the oceans where the storm tracks are most intense, i.e., in the eastern North Pacific and western North Atlantic Oceans. Over North America, areas east of the Rockies exhibit large increases in wind speed during strong-storm activity. It was found that the precipitation associated with strong-storm tracks is most intense where they are strongest. Moreover, the strong-storm track-related precipitation is more intense than that related to the all-storm tracks, especially in the North Atlantic Ocean where the NAA storm track density is particularly high. While strong storms make up about 16% of all-storms, they contribute 30-50% of the all-storm precipitation over the oceans and over North America. Calculations based on an observed precipitation dataset (GPCP) confirm results based only on CFSR products and thus support the robustness of the findings.

The analysis of very high wind speeds and heavy precipitation related to the strong-storm tracks provided an inference of their destructive potential in North America. While the most intense strong-storm wind speeds were found in the central United States, areas most likely to experience the greatest storm wind-related loss span from the Midwest to the east coast states as well as along the southwestern US coast. Heavy precipitation is further enhanced during strong storm activity, with the largest increases occurring along the west coast, in the southeastern US, and near the US east coast. In these areas, strong storms contribute over 30% of the all-storm precipitation that exceeds the local 98th percentile, indicating their vulnerability to damages from heavy strong-storm track-related precipitation.

Our findings indicate that, despite representing a small fraction of all winter storms, strong-storm tracks leave a significant imprint on winter weather in North America. This imprint depends not only on dynamical features but also on the density of the population, thus showing the greatest loss in the eastern US and North American coasts. Over the water, it would be expected that oil platforms and maritime shipping and fishing craft are most vulnerable to storm-related damages just offshore of the US coast.

Chapter 3: Winter Storm Tracks and Related Weather in the CFS Weeks 3-4 Reforecasts for North America

Abstract: *This chapter examines to what extent the NCEP Climate Forecast System (CFS) weeks 3-4 reforecasts reproduce the CFS reanalysis storm track properties, and if so, whether the storm track behavior can contribute to the prediction of related winter weather in North America. The storm tracks are described by objectively tracking isentropic potential vorticity (PV) anomalies for two periods (base, 1983-2002; validation, 2003-2010) to assess their use in advancing S2S prediction in a more realistic forecast mode. Statistically significant positive PV biases are found in the storm track reforecasts. Removal of systematic errors is found to improve general storm track features. CFSRR reproduces well the observed intensity and spatial distributions of storm track-related near-surface winds, with small yet significant biases found in the storm track regions. Removal of the mean wind bias further reduces the error on average by 12%. The spatial distributions of the reforecast precipitation correspond well with the reanalysis, although significant positive biases are found across the contiguous US. Removal of the precipitation bias reduces the error on average by 25%. The bias-corrected fields better depict the observed variability and exhibit additional improvements in the representation of winter weather associated with strong-storm tracks (the storms with more intense PV). Additionally, the reforecasts reproduce the characteristic intensity and frequency of hazardous strong-storm winds. The findings suggest a potential use of storm track statistics in the advancement of subseasonal-to-seasonal weather prediction in North America.*

In Chapter 2, it was found that stronger storms (those with high PV maximum intensity) represent about 16% of all winter storms but contribute in certain regions of North America about 30%-50% of the total storm precipitation (Lukens et al. 2018). Moreover, strong-storm tracks in winter have a significant imprint on near-surface winds and precipitation that can induce considerable structural and economic loss in North America (Lukens et al. 2018).

In this chapter, we evaluate NH winter storm track behavior and related weather in the NCEP CFS Reanalysis and Reforecasts (CFSRR) at sub-monthly (weeks 3-4) time scales for North America. Reforecasts, or retrospective forecasts, are historical predictions of past events used for the calibration and skill assessment of operational model forecasts. The conceptual analysis described in this chapter contrasts weeks 3-4 CFS reforecasts with the CFS reanalysis to assess the use of storm track reforecasts in advancing S2S prediction when working in forecast mode. While winds and other variables (e.g., temperature) may offer more predictive power overall, the intention of this work is to measure the predictive power of one variable: PV and the storm tracks defined by it. Two questions are addressed: (1) Can CFS weeks 3-4 reforecasts reproduce the dynamic properties of storm tracks? (2) If so, does the information carried in those properties contribute to the prediction of the expected severe weather at those time scales in North America?

Chapter 3 is based on the publication Lukens and Berbery (2019). The structure of Chapter 3 is as follows: Section 3.1 describes the datasets, storm tracking methodology, and performance metrics. Section 3.2 discusses the storm tracks' properties as identified in CFSRR at subseasonal scales, and the advantages of

removing the systematic bias. Section 3.3 discusses the storm track-related weather reforecasts and corresponding results from the bias correction, while Section 3.4 describes a similar analysis but for weather related to strong storms. Section 3.5 focuses on the impact of the bias correction on storm track-related winds on the hybrid level 1 surface, and Section 3.6 summarizes the findings and implications.

3.1 *Data and Experimental Design*

3.1.1 CFSR Reforecasts (CFSRR)

CFSRR (Saha et al. 2014a) is a reforecast dataset created at NCEP for calibrations and skill assessments of operational forecasts produced by NCEP's CFS version 2 model (CFSv2; Saha et al. 2014b,c). Nine-month reforecasts are generated using CFSR data as initial conditions that are 5 days apart, and they are archived every 6 hours on a 1° x 1° latitude-longitude grid. Relative to the CFSR system, modifications were made to the atmosphere and land models used to produce the reforecast data to mollify growing biases found in relevant variables (Saha et al. 2014c).

This study focuses on the analysis of a specific range within the S2S gap in predictability, i.e., the weeks 3-4 reforecasts taken from the 9-month retrospective prediction runs initialized at 0000 UTC. *Weeks 3-4* is defined as the period of historical reforecasts that extend from days 14 to 28 from the initialization date. For instance, November 15 initial conditions are used to generate reforecasts for December 1-15, December 1 initial conditions are used to generate reforecasts for December 16-31, and so on for DJF.

The 28-year period is divided into a 20-year base period (1983-2002) where biases are computed, and an 8-year validation period (2003-2010) where bias corrections are applied to test if the bias-corrected CFS weeks 3-4 reforecasts improve the representation of storm tracks when working in forecast mode.

3.1.2 Climate Prediction Center (CPC) Unified Gauge-based Daily Precipitation

The CPC unified gauge-based analysis of daily precipitation for the contiguous United States (CONUS) (Xie et al. 2010) is an observational precipitation dataset that is part of a suite of products in the CPC Unified Precipitation Project. The Project combines all precipitation sources at the CPC to create a consistent suite of products that have improved quality relative to similar gauge-based analyses (Xie et al. 2010). Datasets are constructed from inputs of quality controlled gauge and satellite data using the optimal interpolation (OI) objective analysis technique (Xie et al. 2007; Chen et al. 2008). The data over CONUS are taken from a combined number of about 8,000 daily precipitation reports and are archived on a 0.25° x 0.25° latitude-longitude grid, with daily accumulations ending at 12Z (Chen et al. 2008). CPC daily precipitation observations over CONUS are examined for 28 NH winters in DJF (1983-2010). Prior to plotting the CPC precipitation means are re-gridded to 1° x 1° for comparison with the coarser resolution weeks 3-4 reforecasts.

3.1.3 Storm Tracking and Statistical Analysis Methods

Following the methodology of Hoskins and Hodges (2002), storms are identified as PV maxima that exceed a certain threshold and are objectively tracked throughout their life cycles. Prior to the identification and tracking of storms, the data were filtered to a spectral T42 resolution to reduce noise. Following Chapter 2, the 320-K isentrope is chosen as the level of analysis as it resides in the mid-to-upper troposphere near the upper-level jet stream where characteristics of cyclones are often identified (e.g., Hoskins and Hodges 2002). After the tracking of storms is completed, spatial and temporal filters are applied to remove short-duration storms, leaving only those that last at least 2 days and travel farther than 1000 km (Hodges 1999; Hoskins and Hodges 2002).

For the methodology in Chapter 2, PV anomalies on the 320-K surface (PV_{320}) are considered to be extratropical cyclones (or storms) if their intensities exceed the low threshold of 0.5 PVU. This allows for the retention of a large number of storms in the analysis while still capturing weak cyclogenesis features (see Fig. 2.2). Further, an additional filter is also applied to remove any weak storms with a maximum intensity smaller than a relatively low threshold T_{all} as defined by Eq. (2.2). Table 3.1 shows the values used to compute T_{all} for the reanalysis and uncorrected reforecasts. Both thresholds were obtained from the base period 1983-2002 and are used for both the base period and validation period diagnostics. Differences in the thresholds for the two datasets are due to differences in both the average PV maximum (PV_x) and PV_x standard deviation.

Table 3.1: Values of average PV$_{320}$ maximum ($\overline{PV}_x$) and PV$_x$ standard deviation (SD) used to compute all-storm threshold T$_{all}$ for the reanalysis and weeks 3-4 reforecasts. Thresholds are obtained from all identified cyclones in the NH winter in the base period 1983-2002. Units are PVU

NH 1983-2002 Units: PVU	$\overline{PV}_X$	(PV$_X$)$_{SD}$	T$_{all}$
Reanalysis	3	1.3	1
Reforecasts	3.3	1.7	0.75

Once all storms in the all-storm tracks are identified, a number of statistics can be derived to describe the main properties of the storm tracks, including track density, genesis density, lysis density, and mean intensity statistics. These statistics are defined in Section 2.1.2 and further details on their calculations are discussed in Hodges (1996, 2008).

The approach of Lukens et al. (2018) that is presented in Chapter 2 is used to relate diabatic heating, near-surface winds, and precipitation to the storm tracks. Every 6 hours, diabatic heating and near-surface winds are related to the storm tracks if they are found within a 5° circular area around each cyclone center, and for precipitation a circular area of 12° around each storm center is chosen. To highlight the mid-latitude storm track regions in figures depicting the storm track-related weather, grid points are masked if the average number of storms falls below 0.5 storms per unit area per month.

The root mean squared error (RMSE) is used to assess the accuracy of the reforecasts of storm track intensity and storm track-related weather relative to the reanalysis, that is, by measuring how well the seasonal variability is represented in the reforecasts:

$$RMSE = \sqrt{\frac{1}{n}\sum_{i=1}^{n}(Y_i - X_i)^2} \, , \qquad\qquad (3.1)$$

where X and Y are the storm track PV intensities or related weather variables for the reanalysis and the reforecasts respectively averaged for each winter i, and where n is the total number of winters in the period. Lastly, we examine the ratio (RSR) of the RMSE of the reforecasts to the standard deviation (SD) of the reanalysis. In general, lower RSR values are indicative of a better model performance (Moriasi et al. 2007), and we adopt this concept in our findings for the validation period.

3.2   *All-Storm Tracks in the Reforecasts*

3.2.1   PV Intensity

Following Eq. (2.2), the minimum PV_x intensity threshold to identify all storms in the reanalysis is 1 PVU, while the threshold for all storms in the reforecasts is 0.75 PVU (see Table 3.1). According to Eq. (2.2), the higher values of the reforecast $\overline{PV}_x$ are compensated by the higher values of $(PV_x)_{SD}$, resulting in the lower threshold. The differences between CFSR and CFSRR diagnostics will be the subject of our analysis in this section.

The bias in storm track intensity will be computed as:

$$Bias = \frac{1}{n}\sum_{i=1}^{n}(Y_i - X_i), \qquad\qquad (3.2)$$

where X and Y are the storm track PV intensities for the reanalysis and the reforecasts respectively averaged for each winter i, and where n is the total number of winters in the 1983-2002 period.

Figure 3.1 presents the winter mean PV_{320} intensity over all the points along the all-storm tracks in the base period 1983-2002. In the reanalysis (Fig. 3.1a), the mid-latitude storm tracks are most intense over the eastern North Pacific and western North Atlantic Oceans as well as over the western United States. Over land, an intensity maximum is found over the Rocky Mountains and likely represents a combination of the reinvigoration of westerly Pacific cyclones after they are deflected southward and the rapid development of new cyclones east of the mountain range (Brayshaw et al. 2009; Chang 2009). The intensity maximum in western North America is primarily an upper-level feature (Hoskins and Hodges 2002) that leads to surface cyclone generation farther east. This is supported by Fig. 2.10 (Fig. 7 of Lukens et al. (2018)) that shows stronger surface storm winds farther east of the upper-level intensity maximum.

A similar characterization of winter storm track intensity in CFSRR is done for the weeks 3-4 reforecasts (Fig. 3.1b). While the spatial distribution of intensity maxima resembles that in the reanalysis, the magnitude is greater virtually everywhere in the mid-latitude storm track regions. The difference between the reanalysis and the reforecast PV_{320} intensity (Fig. 3.1c) represents the statistically significant (p-value < 0.05) winter average systematic error or bias as given by Eq. (3.2). The reforecasts exhibit large overestimations of the strength of the storm tracks in the lower mid-latitudes over the oceans and in the high latitudes over northeastern Canada. Significant overestimation is also found in the southwestern and northeastern United States.

In order to assess whether a more realistic description of the storm track intensity in the reforecasts is possible, the PV_{320} systematic bias is then removed from each reforecast at every forecast time that storm centers are identified, and the

All-Storm-Track Mean PV Intensity for 1983-2002

(a) Reanalysis PV

(b) PV Reforecast

(c) Bias in PV

(d) Bias-corrected PV Reforecast
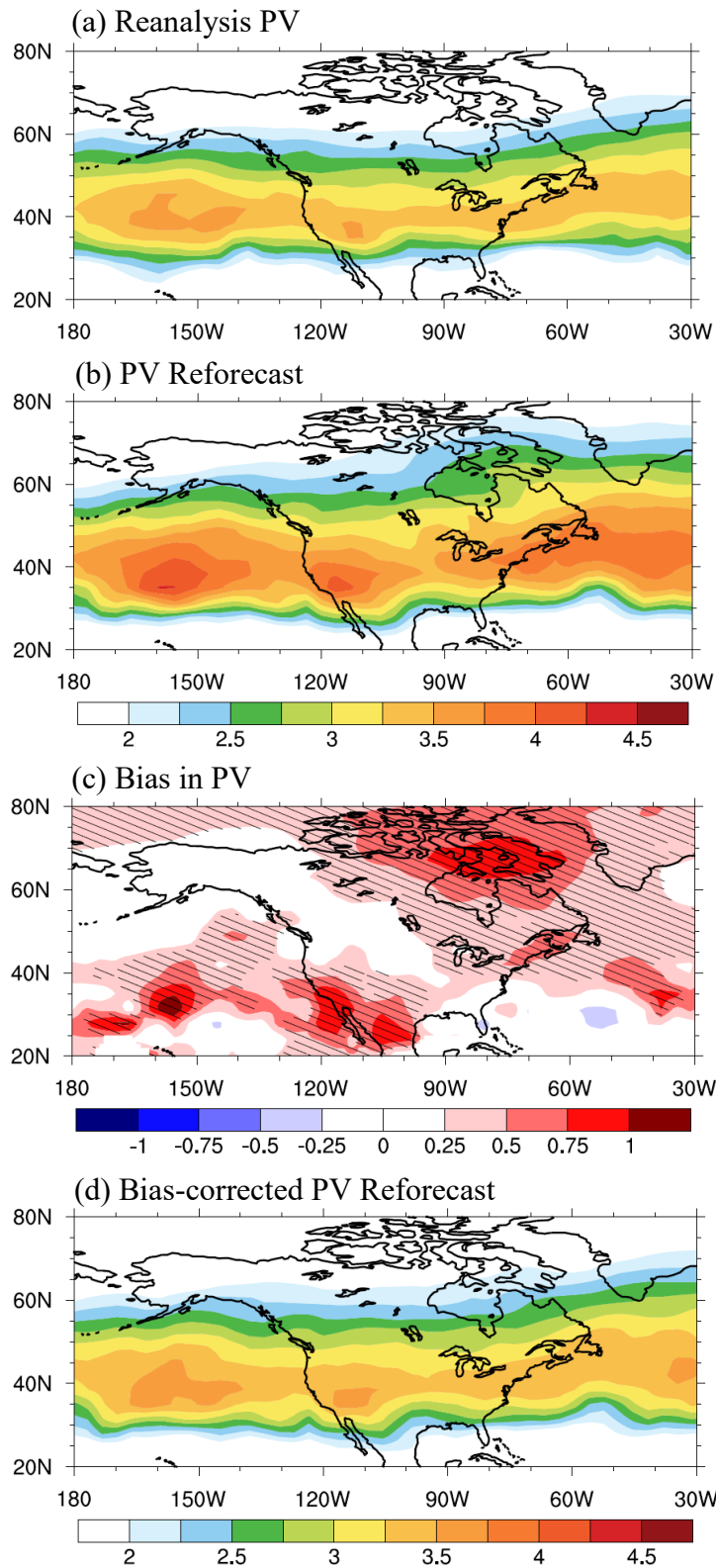
Figure 3.1: Mean PV intensity of points along the all-storm tracks during DJF for the base period 1983-2002. (a) CFS reanalysis; (b) weeks 3-4 reforecast; (c) bias (reforecast minus reanalysis), where hatched regions are statistically significant ($p < 0.05$); (d) bias-corrected weeks 3-4 reforecast. Contour interval for all panels is 0.25 PVU. Areas with less than 0.5 storms per 10^6 km^2 per month in CFSR are masked.

diagnostics are recomputed. If the intensity of a bias-corrected cyclone at a given time step falls below the minimum intensity threshold (0.5 PVU), then the cyclone at that time step is not retained in the bias-corrected storm track analysis. All cyclones that are retained are used to calculate new statistics of bias-corrected storm track behavior. The bias correction applied to the reforecasts is found to reduce the error in the all-storm track intensity and results in the adjusted intensity reforecast shown in Fig. 3.1d. Notably, the corrected reforecast exhibits a closer resemblance to the storm track intensity in the reanalysis in both magnitude and spatial distribution (see Fig. 3.1a).

The mean PV_{320} intensity over all the points along the all-storm tracks in the validation period (2003-2010) is shown in Fig. 3.2. The reanalysis (Fig. 3.2a) corresponds well with that for the base period 1983-2002 (see Fig. 3.1a), despite slightly higher intensities in the mid-latitudes over the oceans. As in the base period, the uncorrected weeks 3-4 reforecasts in the validation period (Fig. 3.2b) overestimate the storm track intensity in the mid-latitudes, particularly over the oceans. When the 1983-2002 bias is removed from each of the 2003-2010 reforecasts and the mean all-storm track intensity is recomputed for the validation period, the results show improvements (Fig. 3.2c). Although some overestimation in the intensity still remains, the bias correction reduces a considerable portion of the error in the mid-latitudes indicating the effectiveness of the approach.

All-Storm-Track Mean PV Intensity for 2003-2010
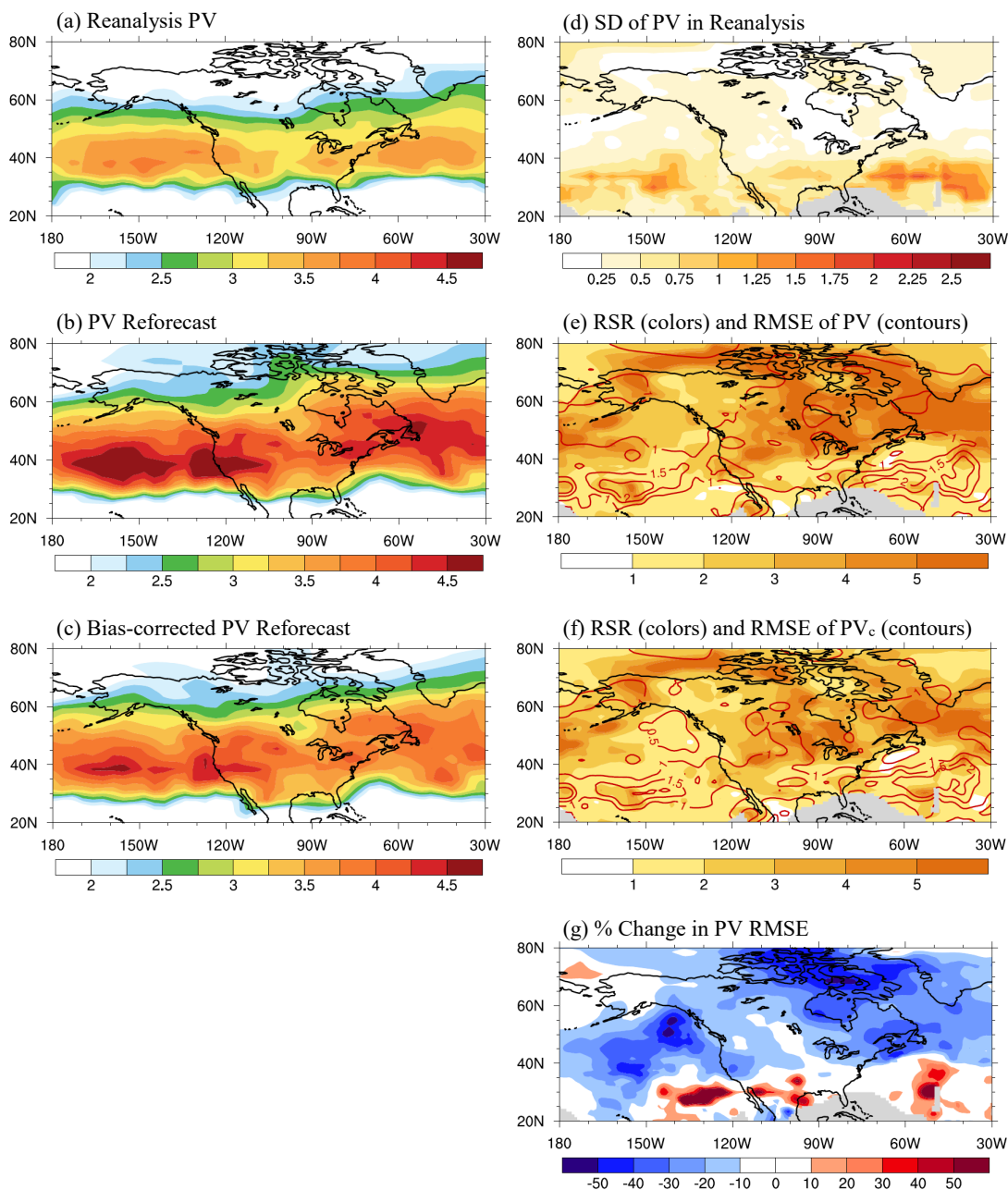
Figure 3.2: Mean PV intensity of points along the all-storm tracks during DJF for the validation period 2003-2010. Left column: (a) CFS reanalysis PV; (b) PV in weeks 3-4 reforecasts; (c) bias-corrected PV (PV_c) in weeks 3-4 reforecasts. Right column: (d) Standard deviation (SD) of reanalysis PV; (e) RMSE of weeks 3-4 reforecast PV (contours at 0.5 PVU interval) and RSR (color shades; interval 1); (f) as in (e) but for the bias-corrected PV_c; (g) Percent change in RMSE after PV bias is removed from reforecasts, shown at an interval of 10%. RSR is the ratio of RMSE of reforecast PV to SD of reanalysis PV. Panels (a)-(d) are shown at an interval of 0.25 PVU. Areas in panels (d)-(g) with less than 0.5 storms per 10^6 km^2 per month in CFSR are masked (gray shade).

Figures 3.2d-g describe the performance of the reforecasts before and after the PV bias correction. The SD of PV intensity (Fig. 3.2d, color shades) is highest in the lower mid-latitudes over the oceans and elsewhere is quite low (< 0.5 PVU). Following Eq. (3.1), the RMSE of the uncorrected reforecasts (Fig. 3.2e, contours) is high throughout the storm track regions relative to the SD. This is reflected in the ratio RSR for PV intensity (Fig. 3.2e, color shades) that depicts large magnitudes over the northeastern North Atlantic Ocean and North America where statistically significant biases are found (see Fig. 3.1c). The bias correction reduces the relatively large RMSE and RSR in these regions (Fig. 3.2f), indicating improved CFSRR performance in terms of storm PV. A decrease (increase) in the percent change in RMSE (Fig. 3.2g) highlights areas where the representation of all-storm track intensity improves (worsens) in the reforecasts after the removal of the corresponding bias. Small errors in storm track intensity that are found in the northeastern North Pacific Ocean (Fig. 3.2e) are reduced by 30%-50% (Fig. 3.2g). Larger errors that are found over the North Atlantic Ocean and over land (Fig. 3.2e) are reduced by 10%-30% in the mid-latitudes and by as much as 50% in the high latitudes (Fig. 3.2g). Biases remain in areas over the oceans in the lower latitudes where the storm track density is quite low (< 1 storm per unit area per month). Because these errors are found outside of the main activity storm track regions, they are not representative of characteristic mid-latitude storm track behavior and as such can be disregarded for the purposes of our study.

3.2.2 Storm Track Properties in the Validation Period 2003-2010

The all-storm track density statistics that represent characteristic winter storm track behavior in the reanalysis and in the bias-corrected weeks 3-4 reforecasts are presented in Figure 3.3 for the validation period 2003-2010. Note that by correcting the intensities, other statistics like cyclogenesis are also adjusted. For the reanalysis, the track density (Fig. 3.3a) and the genesis and lysis densities (Figs. 3.3b and 3.3c, respectively) are similar to those from previous studies (e.g., Hoskins and Hodges 2002; Lukens et al. 2018). The zonally-oriented Pacific storm track and the SW-NE oriented North American-Atlantic storm track are clearly highlighted in the track density, with the Rocky Mountains in western North America acting as a dynamic barrier between the two tracks (Brayshaw et al. 2009; Chang 2009). Regions of cyclogenesis (Fig. 3.3b) are found upstream of storm track intensity maxima (see Fig. 3.2a), with a high number of cyclones developing over the central North Pacific Ocean. As well, many cyclones develop over land in central Canada, near the east coast of North America, and over the North Atlantic Ocean. High densities of cyclogenesis features near the east coast are representative of local nor'easter storms that tend to develop there in winter (Davis and Dolan 1993). Cyclolysis features in the reanalysis (Fig. 3.3c) are found in the downstream sectors of the storm tracks, particularly over the eastern North Pacific Ocean near the North American west coast and over the North Atlantic Ocean in the higher mid-latitudes near the Canadian east coast. Over land, storms tend to dissipate in the northern US near the Great Lakes.

The intensity bias correction is found to generally improve these features, and the results are presented in Figs. 3.3d-f that show the density statistics for the bias-

All-Storm Track Density Statistics for 2003-2010
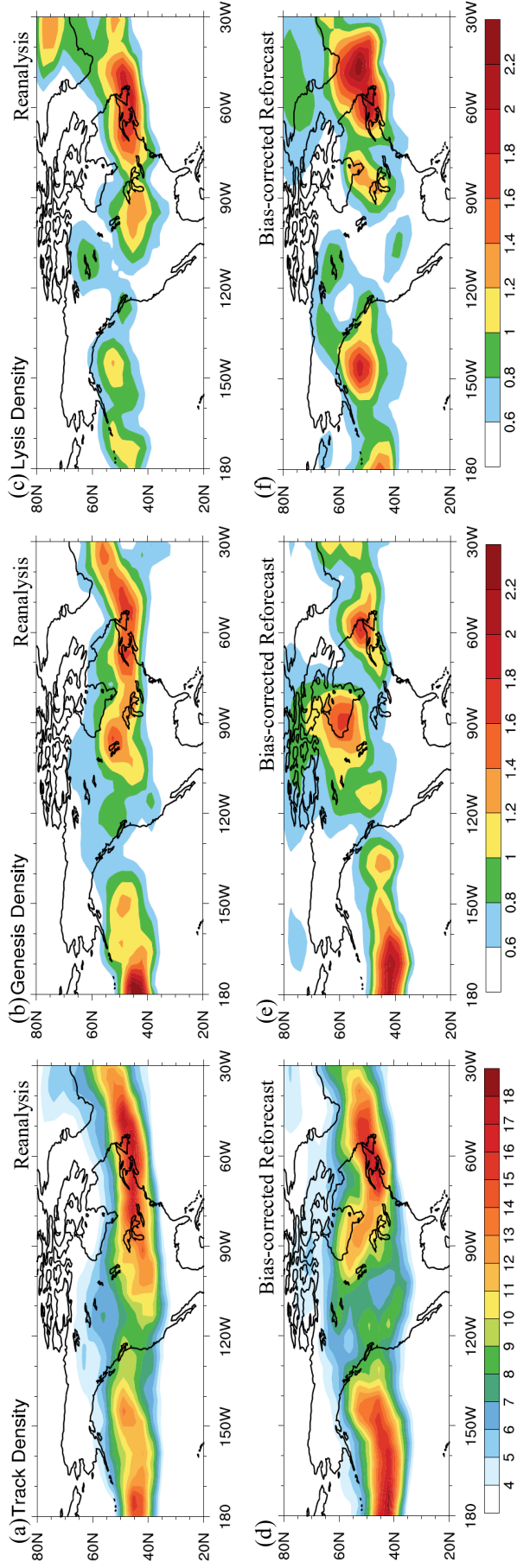
Figure 3.3: Density statistics of NH all-storm tracks during DJF for the validation period 2003-2010. Top row is for CFSR and bottom row is for the bias-corrected weeks 3-4 reforecasts. Left (a,d), middle (b,e), and right (c,f) columns respectively show track, genesis, and lysis densities. Units for all panels are storms per 10^6 km^2 per month. Track densities are shown at intervals of 1, while genesis and lysis densities are shown at intervals of 0.2. Areas with less than 0.5 storms per 10^6 km^2 per month in CFSR are masked.

corrected reforecasts for 2003-2010. The Pacific and NAA storm tracks in the track density bias-corrected reforecast (Fig. 3.3d) share similar spatial distributions to those in the reanalysis (see Fig. 3.3a), with the reforecast exhibiting a slightly higher concentration of cyclone activity in the North Pacific Ocean. The oceanic features shown in the reforecasts of genesis density (Fig. 3.3e) and lysis density (Fig. 3.3f) resemble those in the reanalysis, with differences in magnitude found in the genesis density in the North Atlantic Ocean and in the lysis density in the northeastern North Pacific Ocean.

Over land, the magnitudes of the density features between the reanalysis and bias-corrected reforecasts are similar, although the features in the reforecasts are displaced to the north and east. The displacements reveal regional discontinuities that remain in the reforecasts after the bias is removed, specifically in the track density in the west over the Rocky Mountains and in the genesis and lysis densities over eastern Canada near the Great Lakes. This is perhaps indicative of the differences between the forecast model and the reanalysis, which would require further study.

Storm tracks and extratropical diabatic heating exhibit a co-dependence where each mutually maintains the other by way of baroclinic instabilities (Hoskins and Valdes 1990). The diabatic heating maintains the mean baroclinicity needed to sustain storm activity aloft, while the storms transport and redistribute the heating as they propagate along the storm tracks. We next examine to what extent the reforecasts represent this observed symbiotic nature in winter. Figure 3.4 presents the 900-100-hPa vertically averaged diabatic heating related to the winter all-storm tracks during the validation period 2003-2010, where the diabatic heating is computed as the residual

Diabatic Heating related to PV in All-Storm Tracks for 2003-2010
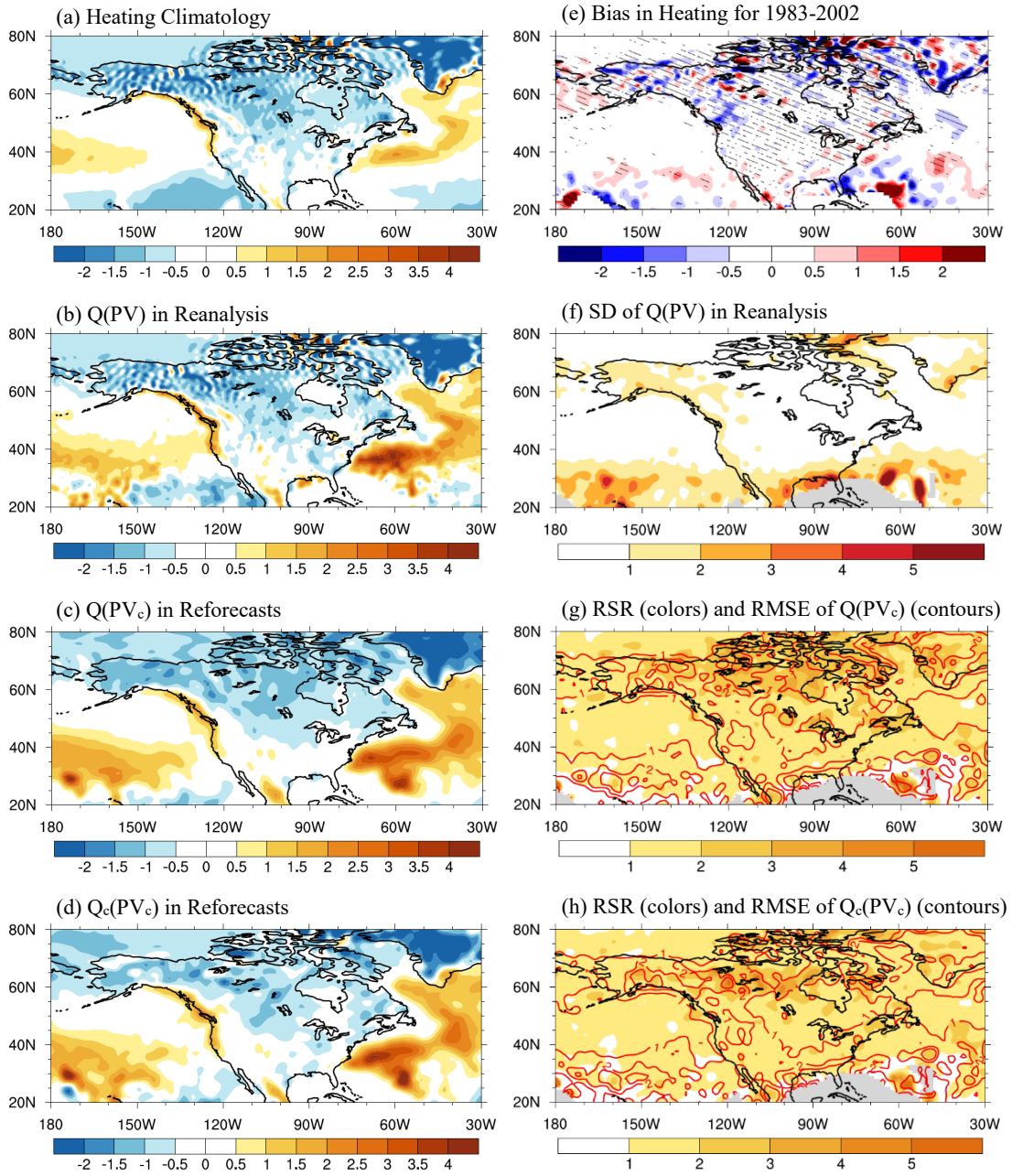
Figure 3.4: Mean vertically averaged 900-100-hPa residual diabatic heating related to the all-storm tracks during DJF for the validation period 2003-2010. Left column: (a) Climatology, (b) CFS reanalysis heating (Q) associated with reanalysis potential vorticity (PV); (c) weeks 3-4 reforecast heating associated with bias-corrected reforecast PV (PV_c); (d) bias-corrected weeks 3-4 reforecast heating (Q_c) associated with reforecast PV_c. Right column: (e) Base period 1983-2002 bias in heating, with hatch marks indicating statistical significance ($p < 0.05$); (f) Standard deviation (SD) of reanalysis Q(PV); (g) RMSE of weeks 3-4 reforecast $Q(PV_c)$ (contours at 2 m s^{-1} interval) and RSR (color shades; interval 1); (h) as in (g) but for the bias-corrected $Q_c(PV_c)$. RSR is the ratio of RMSE of reforecast $Q(PV_c)$ to SD of reanalysis Q(PV). Panels (a)-(e) are shown at an interval of 0.5 K day^{-1}, while panels (f)-(h) are shown at an interval of 1 K day^{-1}. Areas with less than 0.5 storms per 10^6 km^2 per month in CFSR are masked in white near Florida, US in panels (a-e) and in gray shades in panels (f-h)).

in the thermodynamic energy equation, following Eq. (2.4) (Barlow et al. 1998; Holton 2004). The 2003-2010 climatology (Fig. 3.4a) and all-storm track-related heating in the reanalysis (Fig. 3.4b) correspond well with previous studies (e.g., Chan and Nigam 2009; Lukens et al. 2018). The climatology exhibits positive heating rates over the central North Pacific and western North Atlantic Oceans near regions of low-level baroclinic instability (see Fig. 2.4a), as well as along the North American west coast. The reanalysis all-storm track-related heating shares similar spatial patterns to the climatology but exhibits higher heating rates over the oceans where the storm tracks are more intense (see Fig. 3.2a), in particular over the western North Atlantic.

The all-storm track-related heating in the reforecasts (Fig. 3.4c) resembles the reanalysis throughout the storm track regions. Small differences in intensity are found over the oceans, with slightly higher heating rates in the reforecasts found over the eastern North Pacific and slightly lower rates found over the western North Atlantic. The results suggest that the weeks 3-4 reforecasts represent well the diabatic heating related to the all-storm tracks.

To gauge whether any additional value can be extracted from the reforecasts, the mean base period heating bias (Fig. 3.4e) is removed from the validation period reforecasts, resulting in the bias-corrected all-storm heating presented in Fig. 3.4d. The bias is small in the storm track regions but statistically significant in parts of the North Atlantic Ocean as well as over land. The bias-corrected reforecasts of all-storm heating exhibit minor improvements in the storm track regions.

Figures 3.4f-g present statistical comparisons of the all-storm track-related diabatic heating in the uncorrected and bias-corrected reforecasts. The standard

77

deviation of all-storm heating in the reanalysis (Fig. 3.4f) shows that the heating is most variable in the lower mid-latitudes outside of the storm track regions, corresponding with regions of high variability in all-storm track PV (see Fig. 3.2d). The RMSE of the all-storm heating reforecasts (Fig. 3.4g, contours) is close to the reanalysis SD throughout the storm track regions, as evidenced by the low values of the corresponding ratio RSR (Fig. 3.4g, color shades). Removal of the all-storm heating bias slightly reduces the RMSE and RSR values over land but has little impact over the oceans (Fig. 3.4h). The results imply that the reforecasts already capture some of the variability in all-storm track-related heating. Further, the bias correction of all-storm heating has a minor positive effect over land where statistically significant errors are found, but elsewhere provides no additional benefit.

3.3   All-Storm Track-Related Weather in the Reforecasts

Near-surface weather in North America is largely influenced by the development and intensification of extratropical cyclones. In this section, the weather-related features associated with the all-storm tracks will be examined to assess to what extent the reforecasts reproduce those observed in the reanalysis. If they do reproduce what is observed, it will imply that the information carried in the reforecasts of storm tracks could be useful for predictive aims.

In Section 3.2, after the PV_{320} intensity bias was computed and removed from the storm intensity reforecasts, the all-storm track statistics were redone and a new set of tracks was obtained. In this section, the uncorrected reforecasts of surface winds and precipitation (i.e., the original values from the reforecasts) are related to the bias-

corrected storm tracks discussed in Section 3. The resultant weather distributions are used to compute reforecast climatologies of winter weather associated with the all-storm tracks in North America. While the PV bias correction improves the results relative to the relation of uncorrected PV with uncorrected weather reforecasts (not shown), it is found that the bias of winds and precipitation also need to be removed to improve the results (more on this below). This is done by removing the base period (1983-2002) weather biases from the instantaneous all-storm winds and precipitation in the base period and validation period (2003-2010).

As in the case for storm track intensity, new climatologies of all-storm track-related winds and precipitation are computed from the corrected fields. If the corrected precipitation rates (PR) associated with a storm at a particular time step fall below zero, then the precipitation rate at that grid point is set equal to zero, as is done in Zhu and Luo (2015). This occurred less than 10% of the time in CONUS. For winds, the u- and v-components are separately corrected, so the potential for a change in sign is allowed, and the wind speed is calculated after the components have been corrected. Fig. 3.5 shows that the bias correction of wind components (Fig. 3.5a) yields a lower RMSE relative to a more typical correction of wind speed (Fig. 3.5b) (e.g., Sweeney et al. 2013; Holman et al. 2017).

3.3.1 Near-surface Winds

In Chapter 2 Lukens et al. (2018), the CFSR winds in the model's hybrid level 1 (H1) were used to represent the near surface winds. In this chapter, for both CFSR and CFSRR we use the 1000 hPa winds as a proxy of the near-surface winds (mostly
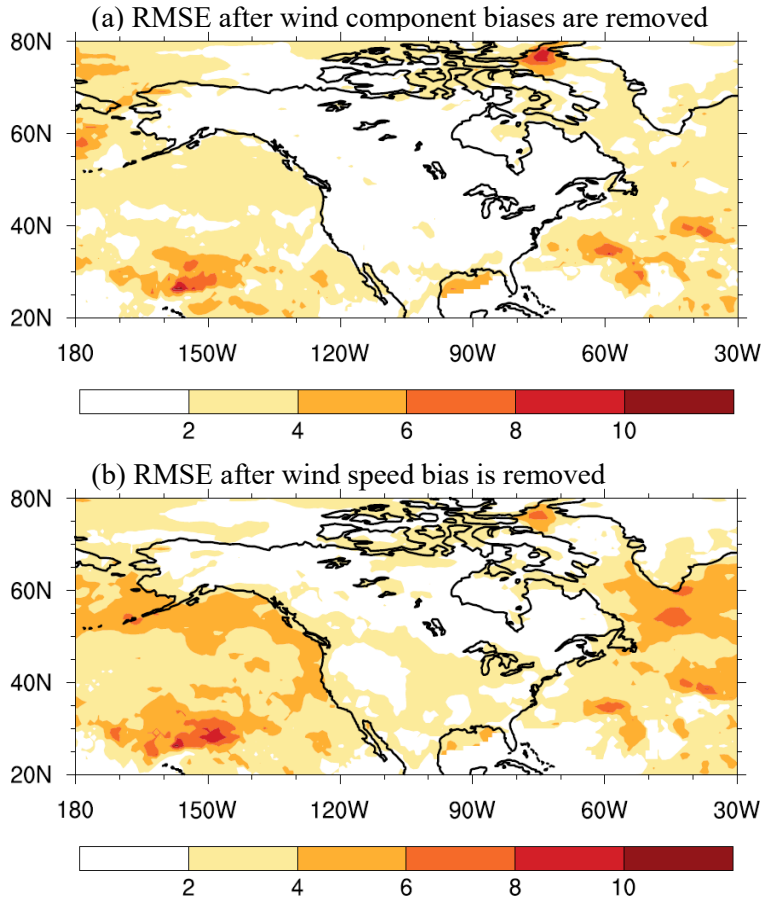
Figure 3.5: Root mean squared error of all-storm track-related wind speed during DJF for the validation period 2003-2010 after removal of (a) wind component biases, and (b) wind speed bias. Areas with less than 0.5 storms per 10^6 km^2 per month in CFSR are masked in white in the lower mid-latitudes equatorward of 30°N.

valid except over high topography). The reason is that the CFSRR H1 winds exhibit a yet unexplained behavior north of 30°N. Fig. 3.6 shows that while for CFSR latitudinal wind profiles at 1000 hPa and H1 (curves in red) remain close to each other, the CFSRR winds at level H1 exhibit a substantial departure from the 1000 hPa winds (profiles in blue). This behavior is observed at all longitudes for all years in the period. We are unaware of any previous study documenting this behavior in CFSRR, and understanding its reasons is outside the scope of this work. Still, we explore the use of
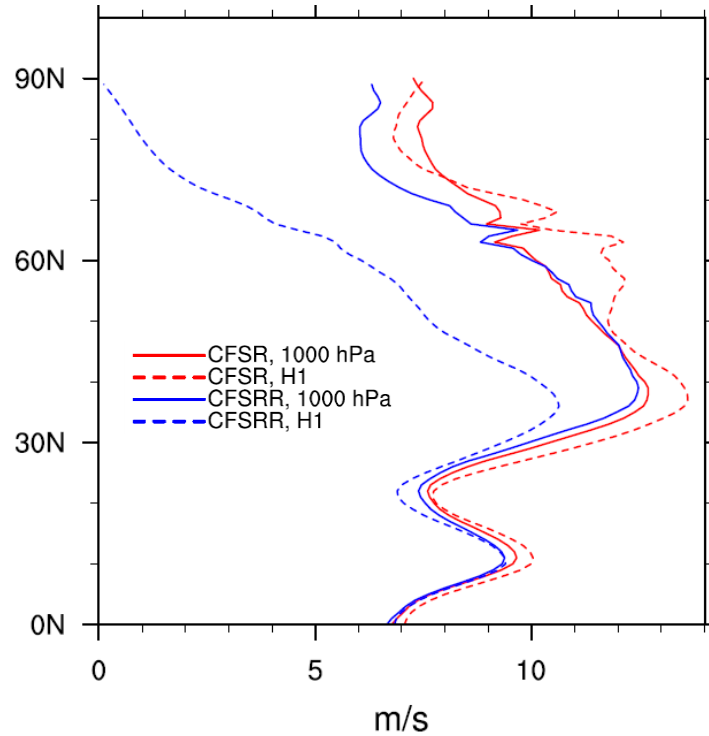
Figure 3.6: Latitude vs. climatological wind speed averaged along the longitude 170°W during DJF for 1983-2010. Solid lines indicate 1000 hPa winds, while dashed lines indicate winds on the hybrid level 1 surface. CFSR is shown in red colors, and the weeks 3-4 reforecasts are shown in blue colors. Units are m s^{-1}.

the bias correction with respect to the hybrid level 1 winds to examine whether the H1 wind reforecasts might be useful for S2S prediction after removing the larger errors. This analysis is discussed in Section 3.5.

We examine the relation of winds on the 1000 hPa surface to the winter all-storm tracks. Figure 3.7 presents the time average of all the winds found within 5 degrees of each point along every cyclone trajectory that shape the all-storm tracks for the base period 1983-2002. In general, near-surface winds are stronger over the oceans than land due in part to a lower value of surface drag over water (Holton 2004). Storm tracks act to enhance the relative strength of the winds in any region (ocean or land), in particular where the storm tracks are more intense (see Chapter 2, Figs. 2.10 and 2.11

Winds at 1000 hPa related to PV in All-Storm Tracks for 1983-2002

(a) V(PV) in Reanalysis
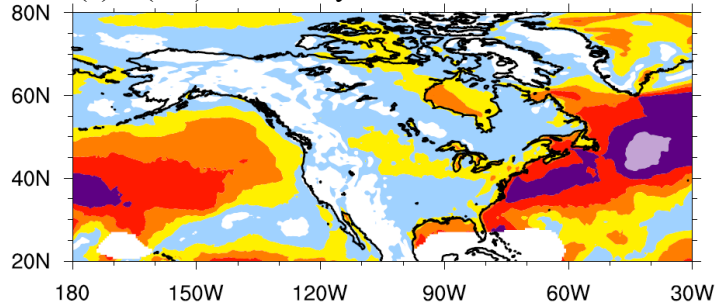
(b) V(PV$_c$) in Reforecasts
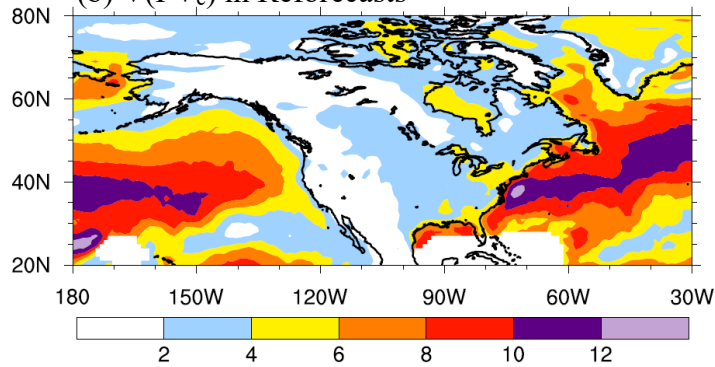
(c) Bias in Winds
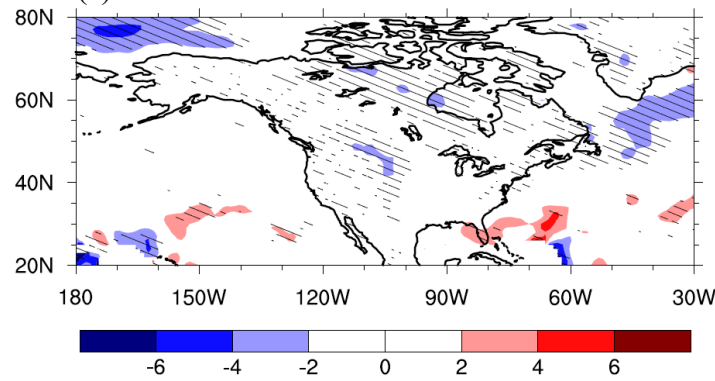
(d) V$_c$(PV$_c$) in Reforecasts
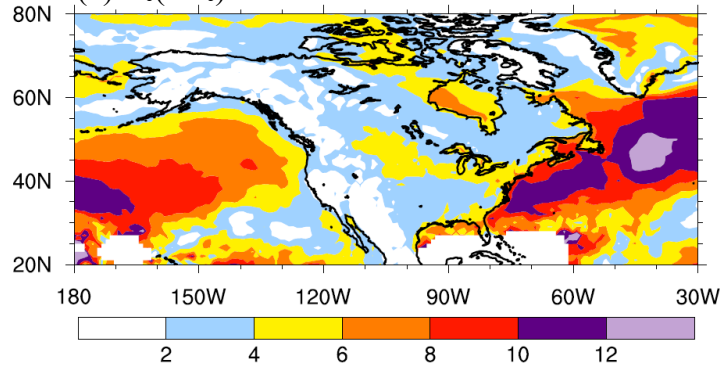
Figure 3.7: Mean all-storm track-related wind speed on the 1000 hPa surface during DJF for the base period 1983-2002. (a) CFS reanalysis wind speed (V) associated with reanalysis potential vorticity (PV); (b) weeks 3-4 reforecast wind speed associated with bias-corrected reforecast PV (PV_c); (c) wind bias (reforecast minus reanalysis), where hatched regions are statistically significant ($p < 0.05$); (d) bias-corrected weeks 3-4 reforecast wind speed (V_c) associated with reforecast PV_c. Contour interval for all panels is 2 m s^{-1}. Areas with less than 0.5 storms per 10^6 km^2 per month in CFSR are masked.

(Lukens et al. 2018, Figs. 7 and 8)). The reanalysis of all-storm winds (Fig. 3.7a) reflects these relations, exhibiting amplified wind speeds over the oceans and North America. Specifically, local maxima are found in the central North Pacific Ocean and across the North Atlantic Ocean. Over land, the strongest winds are found in eastern North America between the Rocky Mountains and the US east coast.

We next evaluate to what extent the reforecasts represent storm track-related winds. The uncorrected wind reforecasts related to the bias-corrected storm tracks (Fig. 3.7b) are found to represent well the all-storm track-related wind speeds in the mid-latitudes for 1983-2002. However, following Eq. (3.2), small yet statistically significant negative biases are found in the storm track regions of the wind reforecasts (Fig. 3.7c), specifically in the northeastern sector of the North Atlantic Ocean and near the Rocky Mountains over land. A bias correction is performed where the local systematic error in the near-surface wind field is removed from the all-storm wind reforecasts. Notably, the removal of the wind bias for 1983-2002 yields a corrected reforecast for the base period (Fig. 3.7d) that bears a closer resemblance to the reanalysis.

We test the validity of the approach as it pertains to all-storm track-related winds by removing the average systematic error for 1983-2002 from each of the reforecasts for 2003-2010 and recalculating the related storm track near-surface winds.

83

The results are presented in Fig. 3.8. Fig. 3.8a shows that the all-storm winds in the reanalysis for the validation period 2003-2010 are statistically significant and are slightly stronger than those for the base period (see Fig. 3.7a), particularly in the western North Atlantic Ocean. As is the case for the base period wind reforecasts, the reforecasts for the validation period (Fig. 3.8b) are similar to the all-storm track-related winds in the reanalysis, with weaker but statistically significant wind speeds found in the North Atlantic Ocean and eastern North America. The wind bias for 1983-2002 (see Fig. 3.7c) is then removed from the reforecasts of all-storm track-related winds for 2003-2010. The resultant bias-corrected reforecast presented in Fig. 3.8c shows some improvement over the oceans as well as over land in the eastern US where the storm wind speeds are statistically significant.

A statistical comparison of the all-storm wind reforecasts before and after the bias correction shows that the reforecasts already closely match the reanalysis (Figs. 3.8d-g). As in the case of the PV SD (see Fig. 3.2d), the SD of all-storm winds in the reanalysis is highest over the oceans in the lower mid-latitudes (Fig. 3.8d). Following Eq. (3.1), the RMSE of uncorrected all-storm winds (Fig. 3.8e, contours) is larger than the SD in those regions as well as in the northeast ocean basins and over land in eastern North America. The corresponding ratio RSR of all-storm winds is generally low (Fig. 3.8e, color shades), particularly in the lower mid-latitudes where the SD is highest, suggesting that the uncorrected reforecasts already somewhat capture the variability in all-storm track-related winds.

The all-storm wind reforecasts further improve after the base period wind bias is removed, as evidenced by the reduced RMSE of the bias-corrected reforecast winds

Winds related to PV in All-Storm Tracks for 2003-2010
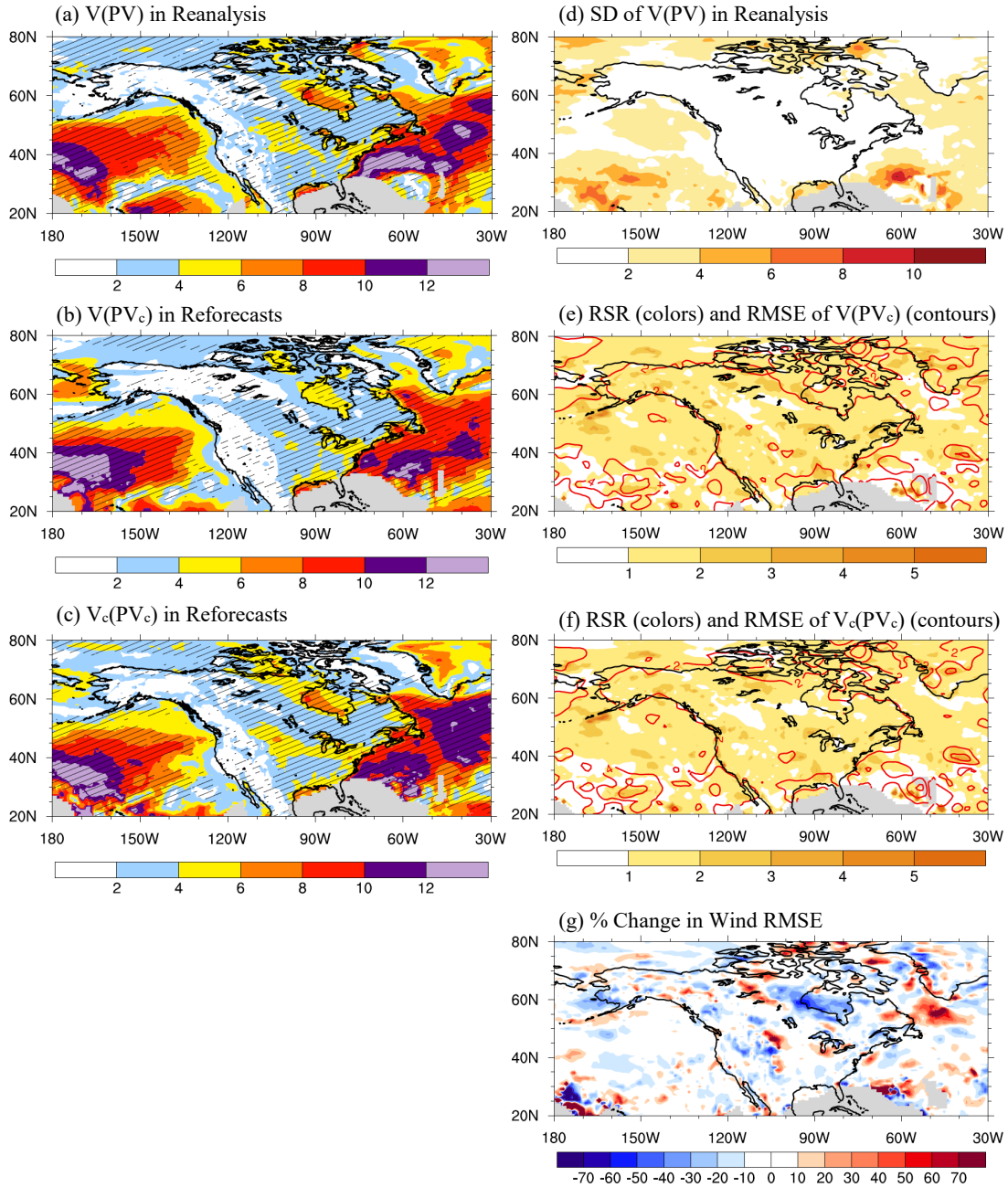
Figure 3.8: Mean all-storm track-related wind speed on the 1000 hPa surface during DJF for the validation period 2003-2010. Left column: (a) CFS reanalysis wind speed (V) associated with reanalysis potential vorticity (PV); (b) weeks 3-4 reforecast wind speed associated with bias-corrected reforecast PV (PV_c); (c) bias-corrected weeks 3-4 reforecast wind speed (V_c) associated with reforecast PV_c. Hatched marks in (a)-(c) indicate statistical significance ($p < 0.05$). Right column: (d) Standard deviation (SD) of reanalysis V(PV); (e) RMSE of weeks 3-4 reforecast $V(PV_c)$ (contours at 2 m s^{-1} interval) and RSR (color shades; interval 1); (f) as in (e) but for the bias-corrected $V_c(PV_c)$; (g) Percent change in RMSE after wind bias is removed from reforecasts, shown at an interval of 10%. RSR is the ratio of RMSE of reforecast $V(PV_c)$ to SD of reanalysis V(PV). Panels (a)-(d) are shown at an interval of 2 m s^{-1}. Areas with less than 0.5 storms per 10^6 km^2 per month in CFSR are masked (gray shade).

(Fig. 3.8f, contours) and the low values of the corresponding RSR (Fig. 3.8f, color shades). Areas of improvement are further highlighted by negative values in the change in the wind RMSE (Fig. 3.8g). The small error in all-storm wind speed is reduced on average by about 12% in the storm track regions. Specifically, decreased errors are found in the lower mid-latitudes over the eastern North Pacific and western North Atlantic Oceans as well as in the eastern United States. Additionally, the removal of the 1983-2002 wind bias from the 2003-2010 reforecasts reduces the error in estimation in the high latitudes outside of the main regions of storm activity where the bias is statistically significant. In summary, the findings indicate that the CFS weeks 3-4 reforecasts already contain useful information for the prediction of near-surface storm winds at weeks 3-4 time scales, with the bias correction providing additional minor improvements.

3.3.2 Precipitation

The relation of winter precipitation at the surface in CONUS to the all-storm tracks is examined next. The time average of all precipitation in CONUS that is found within 12 degrees of each point along every cyclone trajectory that shape the all-storm tracks for the base period 1983-2002 is presented in Fig. 3.9. In the CPC gauge-based daily precipitation analysis (Fig. 3.9a), precipitation rates associated with the all-storm tracks are highest near the North American west coast where they exceed 7 mm day^{-1} and in the southeastern United States where they reach 6 mm day^{-1}.

In the corresponding uncorrected weeks 3-4 reforecast (Fig. 3.9b), precipitation related to the bias-corrected all-storm tracks is overestimated. Specifically, the

Precipitation related to PV in All-Storm Tracks
for 1983-2002

(a) CPC PR(PV) in Reanalysis
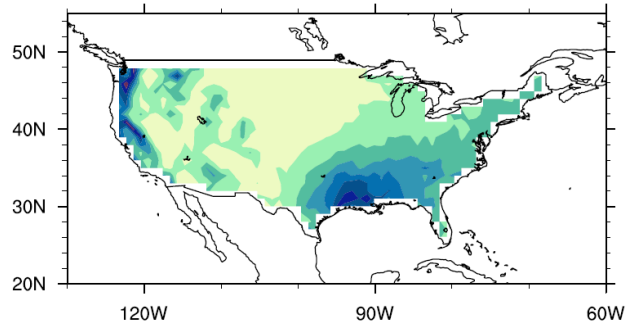
(b) PR(PV$_c$) in Reforecasts
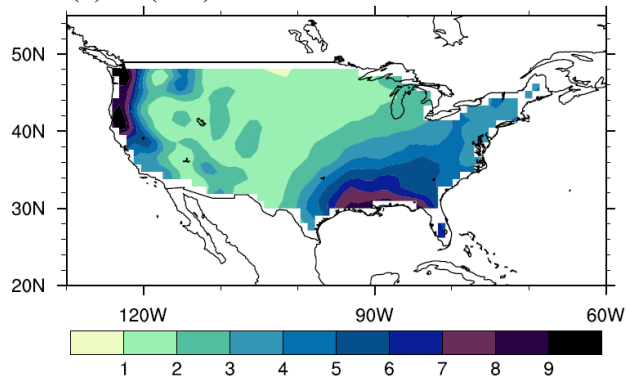
(c) Bias in PR
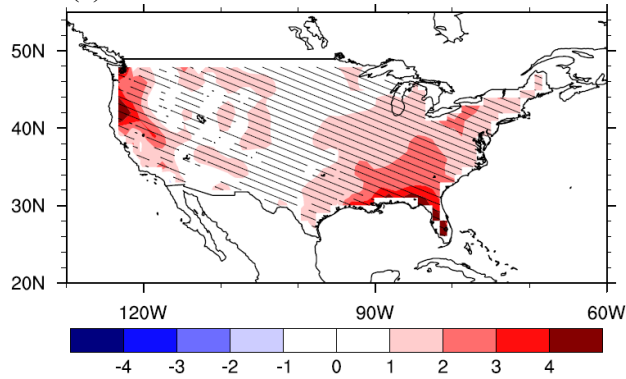
(d) PR$_c$(PV$_c$) in Reforecasts
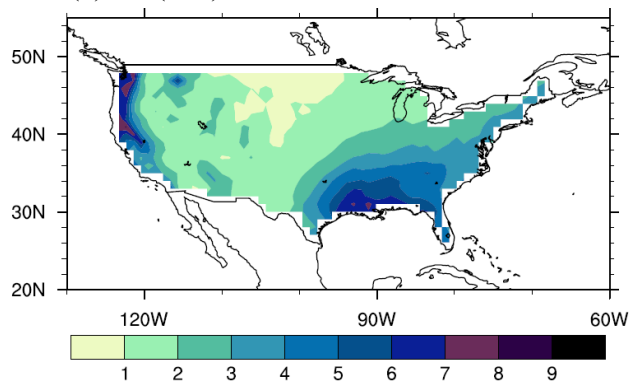
Figure 3.9: Mean all-storm track-related daily precipitation rates (PR) during DJF for the base period 1983-2002 in the contiguous US (CONUS). (a) CPC gauge-based analysis PR associated with reanalysis potential vorticity (PV); (b) weeks 3-4 reforecast PR associated with bias-corrected reforecast PV (PV_c); (c) PR bias (reforecast minus CPC analysis), where hatched regions are statistically significant ($p < 0.05$); (d) bias-corrected weeks 3-4 reforecast PR (PR_c) associated with reforecast PV_c. Contour interval for all panels is 1 mm day^{-1}. Areas outside CONUS are masked.

uncorrected reforecasts tend to overestimate precipitation in the eastern US and near the west coast. This is more clearly seen in Fig. 3.9c that highlights statistically significant biases in the reforecasts for the base period, following Eq. (3.2). The removal of the bias yields the corrected all-storm precipitation associated with the bias-corrected storm tracks for 1983-2002 (Fig. 3.9d). As in the case of winds, the bias-corrected precipitation reforecasts better correspond with observations.

The approach is validated for the period 2003-2010, with the time average of winter precipitation over CONUS found within 12 degrees of all storm centers in the all-storm tracks being presented in Fig. 3.10. Reanalysis and reforecast storm precipitation rates are statistically significant in CONUS. The CPC analysis for the validation period (Fig. 3.10a) depicts a similar precipitation pattern to that for the base period (see Fig. 3.9a), with maxima found near the west coast of North America and in the southeastern United States. The uncorrected reforecast precipitation for 2003-2010 (Fig. 3.10b) exhibits large overestimations in these areas. The removal of the base period bias (see Fig. 3.9c) from the uncorrected reforecasts for the validation period yields improvements in the 2003-2010 precipitation reforecasts (Fig. 3.10c). The precipitation intensity in the bias-corrected reforecasts is reduced near the west coast and in the eastern US.

Precipitation related to PV in All-Storm Tracks for 2003-2010

(a) PR(PV) in Reanalysis

(b) PR(PVc) in Reforecasts

(c) PRc(PVc) in Reforecasts

(d) SD of PR(PV) in Reanalysis

(e) RSR (colors) and RMSE of PR(PVc) (contours)

(f) RSR (colors) and RMSE of PRc(PVc) (contours)

(g) % Change in PR RMSE

Figure 3.10: Mean all-storm track-related daily precipitation rates (PR) during DJF for the validation period 2003-2010 in the contiguous US (CONUS). Left column: (a) CPC gauge-based analysis PR associated with reanalysis potential vorticity (PV); (b) weeks 3-4 reforecast PR associated with bias-corrected reforecast PV (PV_c); (c) bias-corrected weeks 3-4 reforecast PR (PR_c) associated with reforecast PV_c. Hatched marks indicate statistical significance ($p < 0.05$). Right column: (d) Standard deviation (SD) of reanalysis PR(PV); (e) RMSE of weeks 3-4 reforecast $PR(PV_c)$ (contours at 1 mm day^{-1} interval) and RSR (color shades; interval 1); (f) as in (e) but for the bias-corrected $PR_c(PV_c)$; (g) Percent change in RMSE after PR bias is removed from reforecasts, shown at an interval of 10%. RSR is the ratio of RMSE of reforecast $PR(PV_c)$ to SD of reanalysis PR(PV). Panels (a)-(d) are shown at an interval of 1 mm day^{-1}. Areas in CONUS with missing values and less than 0.5 storms per 10^6 km^2 per month in CFSR are masked (gray shade).

The improvements are reflected in Figs. 3.10d-g that describe the performance of CFSRR before and after the bias correction. The standard deviation of precipitation in the reanalysis (Fig. 3.10d) is shown to be highest in the western and southeastern US where the precipitation rates are highest. Likewise, the uncorrected precipitation RMSE (Fig. 3.10e, contours) is largest in these regions, following Eq. (3.1). However, in the eastern US the corresponding ratio RSR (Fig. 3.10e, color shades) is lower where the precipitation rates are high and higher where the precipitation rates are low. The low RSR in regions with high precipation rates suggest the usability of the reforecasts without the correction. After the base period precipitation bias is removed from the validation period reforecasts, the RMSE in is reduced (Fig. 3.10f, contours) and gets closer to the magnitude of the standard deviation of reanalysis precipitation (see Fig. 3.10d). This is exemplified in the reduced RSR of the bias-corrected reforecasts (Fig. 3.10f, color shades) and suggests that the bias-corrected reforecasts better depict the general variability in precipitation in CONUS, although the correction appears to have little to no effect in regions with low RSR. The percent change in RMSE for precipitation (Fig. 3.10g) supports this finding, as it displays large reductions in error in regions with lower precipitation rates and smaller decreases in areas with high

precipitation rates. Further, the error in estimation is found to decrease by about 25% on average in CONUS, although large biases remain in the western and southeastern US where the all-storm precipitation rates are highest. Overall, the findings suggest that the removal of the precipitation biases from the reforecasts lead to RSR decreases in the storm tracks, improving the representation of the observed variability in all-storm track-related precipitation in the CFS weeks 3-4 reforecasts.

3.4 *Reforecasts of Strong-Storm Tracks and Related Weather*

This section will discuss a subset of all storms: those that achieve high PV intensities and shape what are called *strong-storm tracks*. Strong storms have the potential to produce high winds and heavy precipitation that can induce transportation interruptions, higher demands for power and emergency supplies, and an increased risk of damages and casualties (Kunkel et al. 2013; Wang et al. 2017). Moreover, strong-storm tracks have been found to have a significant imprint on winter weather in North America (Lukens et al. 2018).

Following a similar approach to that discussed in Section 3.1 and in Chapter 2, strong-storm tracks are shaped by storms with maximum PV intensities that exceed a threshold of T_{str} as defined by Eq. (2.3). T_{str} is calculated separately for the Pacific and NAA storm tracks for the validation period 2003-2010 only. The values used to compute T_{str} are the same for both storm tracks and are shown for the reanalysis and reforecasts in Table 3.2. Differences in T_{str} between the datasets are due to differences in $\overline{PV}_x$ and $(PV_x)_{SD}$, where the higher values in the reforecasts yield higher T_{str} thresholds. Following Eq. (2.3), a strong storm that develops in either the Pacific or

Table 3.2: Values of average PV$_{320}$ maximum $\overline{(PV_x)}$ and PV$_x$ standard deviation (SD) used to compute strong-storm threshold T$_{str}$ for the reanalysis, weeks 3-4 reforecasts, and bias-corrected weeks 3-4 reforecasts. Thresholds are obtained from all storms in Pacific (PAC) and North American-Atlantic (NAA) storm track regions in the validation period 2003-2010. Units are PVU.

PAC,NAA 2003-2010 Units: PVU	$\overline{PV}_X$	$(PV_X)_{SD}$	T$_{str}$
Reanalysis	3.8	1.1	4.9
Reforecasts	4.9	1.6	6.5
Bias-corrected Reforecasts	4.6	1.5	6.1

NAA storm track region in the reanalysis for 2003-2010 must achieve a maximum intensity of 4.9 PVU or greater (Table 3.2). The overestimation of all-storm track intensity found in the uncorrected reforecasts (Section 3.2) gives rise to a higher strong-storm threshold value of 6.5 PVU for storms. This value decreases to 6.1 PVU after the intensity bias is removed, reflecting the improvement in the reforecasts also discussed in Section 3.2.

Strong storms in the reanalysis are found to represent about 15% of all storms that develop in the Pacific and NAA storm track regions in 2003-2010. As in CFSR, strong storms in the uncorrected and bias-corrected reforecasts are found to represent about 15% of all storms that develop in either region, suggesting that the reforecasts capture the relative distribution of strong storms in winter despite overestimations in storm PV$_{320}$ intensity.

Characteristics of strong-storm track behavior are presented as density statistics in Fig. 3.11. The strong-storm density properties in the reanalysis (Figs. 3.11a-c) resemble those for the all-storm tracks (see Figs. 3.3a-c) and correspond well with those

Strong-Storm Track Density Statistics for 2003-2010
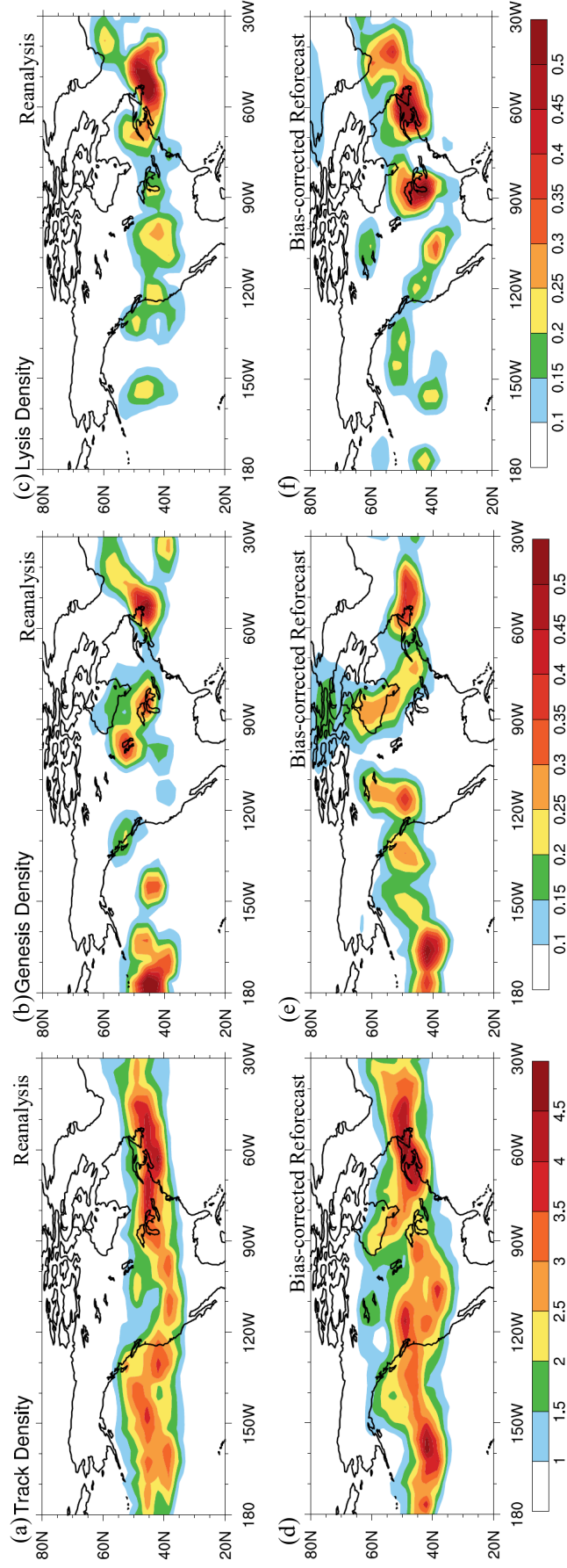
Figure 3.11: Density statistics of NH strong-storm tracks during DJF for the validation period 2003-2010. Top row depicts CFSR and bottom row is for bias-corrected weeks 3–4 reforecasts. Left (a,d), middle (b,e), and right (c,f) columns respectively show track, genesis, and lysis densities. Units for all panels are storms per 10^6 km^2 per month. Track densities are shown at intervals of 0.5, while genesis and lysis densities are shown at intervals of 0.05. Areas where strong storms are not found and where there are less than 0.5 storms per 10^6 km^2 per month in CFSR are masked.

presented in Chapter 2 and Lukens et al. (2018). The track density (Fig. 3.11a) exhibits high concentrations of strong-storm activity throughout the Pacific and NAA storm track regions, with the highest concentrations found over the North Atlantic Ocean. Strong-storm cyclogenesis features (Fig. 3.11b) are found upstream of track density maxima while cyclolysis regions are found downstream (Fig. 3.11c).

The PV intensity bias correction in the all-storm tracks (Section 3.2) is found to generally improve the strong-storm density features in the reforecasts, and the results are presented in Figs. 3.11d-f. The strong-storm track density in the bias-corrected reforecasts (Fig. 3.11d) shares similar spatial distributions to that of the reanalysis (see Fig. 3.11a), with the reforecasts displaying higher concentrations of storm activity over the eastern North Pacific Ocean and over land. Over the oceans, the cyclogenesis and cyclolysis features in the bias-corrected reforecasts (Figs. 3.11e and 3.11f respectively) resemble those of the reanalysis, although regional discontinuities remain in the reforecasts after the all-storm intensity bias is removed. This is particularly evident over land (a) in western (eastern) Canada where cyclogenesis features in the reforecasts are amplified (dampened) and displaced to the east, and (b) in the western US and the Great Lakes region where cyclolysis features in the reforecasts are amplified and displaced to the south.

3.4.1   Heating, Winds, and Precipitation

In this section, the relation between strong-storm tracks and winter weather variables in the weeks 3-4 reforecasts for the validation period (2003-2010) is assessed. This is done in the reforecasts by relating the uncorrected winds and precipitation to

the strong-storm tracks that are a subset of the *bias-corrected* all-storm tracks. Further, we relate the bias-corrected weather reforecasts (Section 3.3) to the bias-corrected strong-storm tracks to examine the effects of the bias correction of all-storm weather on the reforecasts of strong-storm weather. The average biases in all-storm weather reforecasts generally resemble the biases in the strong-storm weather reforecasts in the storm track regions, indicating that all-storm weather biases partially represent the errors in both all-storm and strong-storm track-related weather. This implies that the removal of all-storm biases can reduce a good portion of the error in the strong-storm reforecasts and lead to improved results. By removing one bias from all sets of storm tracks, the approach remains simple and fast, and this is beneficial for the rapid release of improved severe weather forecasts in operations.

Results from an analysis of diabatic heating related to the strong-storm tracks in the reanalysis and reforecasts during 2003-2010 (Fig. 3.12) are comparable to the results for all-storm track-related heating presented in Section 3.2 (see Fig. 3.4). The reanalysis (Fig. 3.12a) shows that the strong-storm tracks are associated with higher heating rates over the oceans relative to the all-storm tracks, corresponding with the findings in Chapter 2 and Lukens et al. (2018). The strong-storm heating in the weeks 3-4 reforecasts (Fig. 3.12b) closely match the reanalysis heating in spatial distribution and intensity. The corresponding RSR values are low (Fig. 3.12e) and indicate that the RMSE is close to the SD of strong-storm heating in the reanalysis as shown in Fig. 3.12d. The bias correction results in little to no improvement in the strong-storm heating reforecasts (Fig. 3.12c), and this is reflected in Fig. 3.12f that shows little change in the RSR and RMSE values for the bias-corrected reforecasts relative to the

Diabatic Heating related to PV in Strong-Storm Tracks for 2003-2010
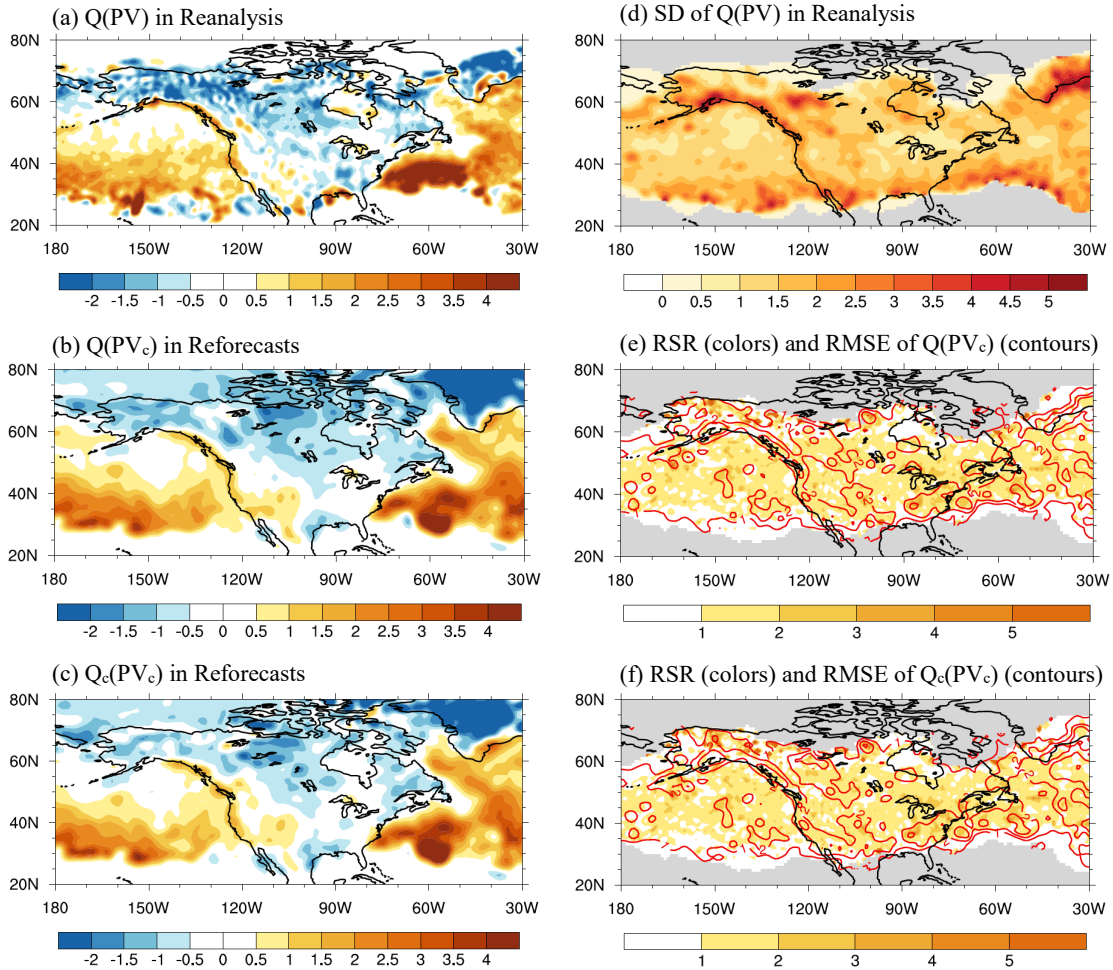
Figure 3.12: Mean vertically averaged 900-100-hPa residual diabatic heating related to the strong-storm tracks during DJF for the validation period 2003-2010. Left column: (a) CFS reanalysis heating (Q) associated with reanalysis potential vorticity (PV); (b) weeks 3-4 reforecast heating associated with bias-corrected reforecast PV (PV_c); (c) bias-corrected weeks 3-4 reforecast heating (Q_c) associated with reforecast PV_c. Right column: (d) Standard deviation (SD) of reanalysis Q(PV); (e) RMSE of weeks 3-4 reforecast $Q(PV_c)$ (contours at 2 m s^{-1} interval) and RSR (color shades; interval 1); (f) as in (e) but for the bias-corrected $Q_c(PV_c)$. RSR is the ratio of RMSE of reforecast $Q(PV_c)$ to SD of reanalysis Q(PV). Panels (a)-(d) are shown at an interval of 0.5 K day^{-1}, while panels (e),(f) are shown at an interval of 1 K day^{-1}. Areas with less than 0.5 storms per 10^6 km^2 per month in CFSR are masked.

uncorrected reforecasts (see Fig. 3.12e). The findings suggest that CFSRR already partially captures the observed variability in strong-storm diabatic heating, with the bias correction offering little to no additional improvement.Near-surface winds associated with the strong-storm tracks in the validation period 2003-2010 are presented in Fig. 3.13. The strong-storm track-related winds in the reanalysis (Fig. 3.13a) are statistically significant and found to be most intense over the oceans and in eastern North America, corresponding with the findings of Lukens et al. (2018). Moreover, they are stronger on average than the all-storm track-related winds (see Fig. 3.8a), specifically in the western North Atlantic Ocean where deep convective heating tends to add to the local baroclinicity and invigorate strong storms (Chang 2009; Lukens et al. 2018). The results presented here using PV to track cyclones are consistent with the findings from other studies that identify storms using sea level pressure (e.g., Leckebusch et al. 2008; Booth et al. 2015). Those studies found that strong surface winds are generally found to the south and southeast of the centers of storms that produce strong winds. This study shows that on average in winter, the strongest near-surface winds associated with cyclones (Fig. 3.13a) are often found south of strong-storm (or cyclone) track density maxima (see Fig. 3.11a).

The reforecasts of strong-storm track-related winds (Figs. 3.13b-c) are statistically significant and share similar patterns to the reanalysis (see Fig. 3.13a), as is the case of the all-storm winds (see Fig. 3.8). The uncorrected reforecast of strong-storm winds (Fig. 3.13b) exhibit slightly weaker wind speeds found in the northeastern North Pacific and western North Atlantic Oceans. The bias-corrected winds related to the strong-storm tracks are depicted in Fig. 3.13c. Improvements are found in the

Winds related to PV in Strong-Storm Tracks for 2003-2010
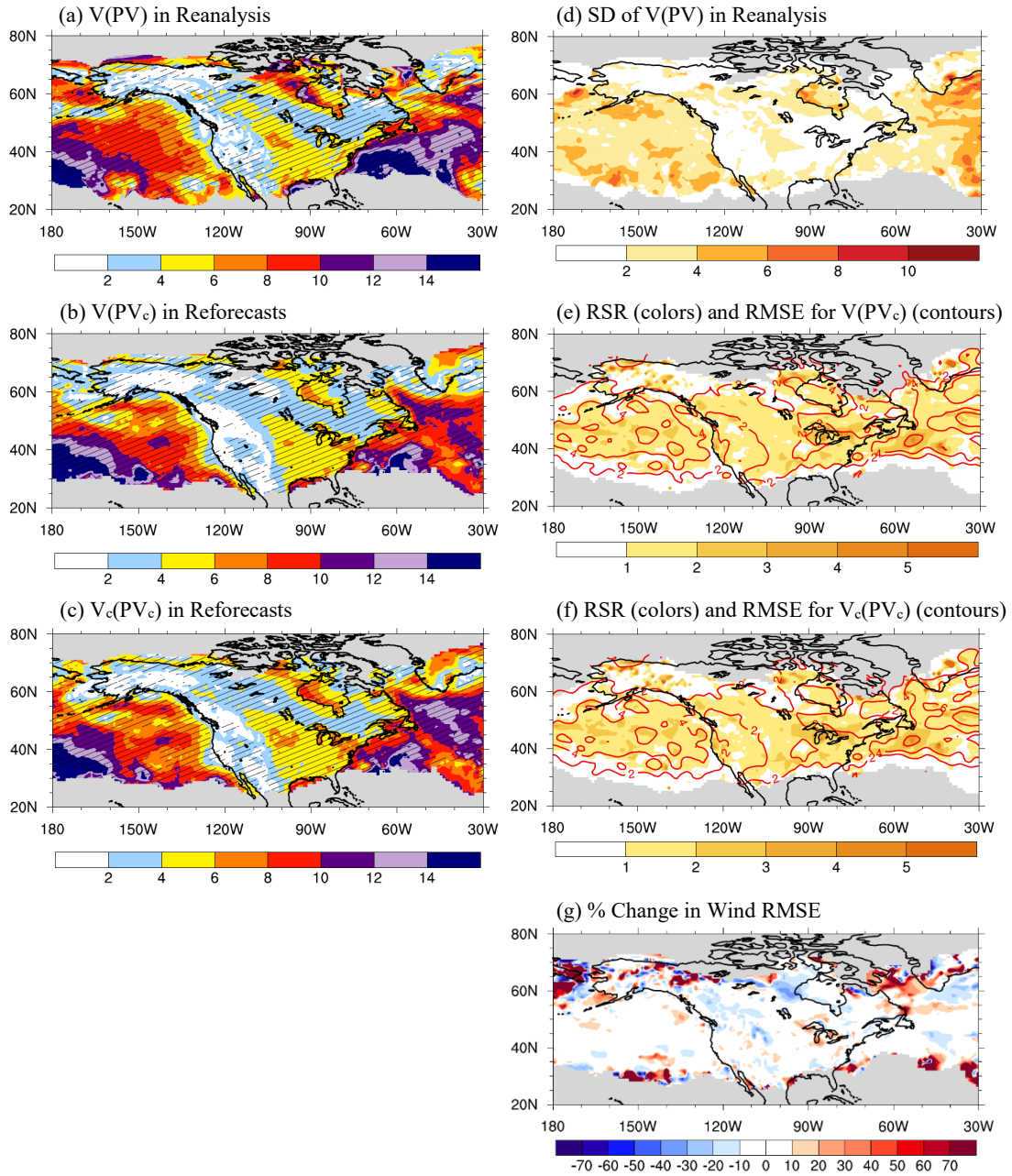
Figure 3.13: Mean strong-storm track-related wind speed on the 1000 hPa surface during DJF for the validation period 2003-2010. Left column: (a) CFS reanalysis wind speed (V) associated with reanalysis potential vorticity (PV) with $T_{str} = 4.9$ PVU; (b) weeks 3-4 reforecast wind speed associated with bias-corrected reforecast PV (PV_c) with $T_{str} = 6.1$ PVU; (c) bias-corrected weeks 3-4 reforecast wind speed (V_c) associated with reforecast PV_c with $T_{str} = 6.1$ PVU. Hatched marks indicate statistical significance ($p < 0.05$). Right column: (d) Standard deviation (SD) of reanalysis V(PV); (e) RMSE of weeks 3-4 reforecast $V(PV_c)$ (contours at 2 m s^{-1} interval) and RSR (color shades; interval 1); (f) as in (e) but for the bias-corrected $V_c(PV_c)$; (g) Percent change in RMSE after all-storm wind bias is removed from reforecasts, shown at an interval of 10%. RSR is the ratio of RMSE of reforecast $V(PV_c)$ to SD of reanalysis V(PV). Panels (a)-(d) are shown at an interval of 2 m s^{-1}. Areas with less than 0.5 storms per 10^6 km^2 per month in CFSR and where strong storms are not found are masked (gray shade).

northeastern North Atlantic Ocean and in eastern North America. Additional improvements are found at high latitudes over Canada near the Hudson Bay.

Figs. 3.13d-g present statistics of the strong-storm track winds. The SD of the reanalysis strong-storm track-related winds is relatively high over the North Pacific and central North Atlantic Oceans (Fig. 3.13d). Similarly, large RMSE values in the uncorrected strong-storm winds (Fig. 3.13e, contours) are found over water, in particular over the northeastern North Atlantic Ocean. Smaller errors are found over land in eastern North America. The ratio RSR for the uncorrected reforecasts (Fig. 3.13e, color shades) is generally low in the storm track regions, indicating that the RMSE is close to the SD. After the bias correction, the RMSE is further reduced, and the RSR remains low (Fig. 3.13f), suggesting that the bias-corrected reforecasts better capture the variability in strong-storm winds. This is reflected in the percent change in strong-storm wind RMSE (Fig. 3.13g) that shows decreases in error in the eastern North Atlantic Ocean and over land. The findings indicate that the reforecasts are already partially useful for the prediction of strong-storm track-related winds at the weeks 3-4 time scales, and the bias correction leads to further improvements in both the mid- and high latitudes.

Winter precipitation associated with the strong-storm tracks in the validation period 2003-2010 is presented in Fig. 3.14. Strong-storm track-related precipitation in the CPC gauge-based analysis (Fig. 3.14a) resembles the all-storm precipitation (see Fig. 3.10a) and is statistically significant in CONUS, with maxima found near the west coast and in the southeastern US. In general, winter precipitation is more intense during strong-storm activity. The uncorrected reforecast of strong-storm precipitation (Fig.

Precipitation related to PV in Strong-Storm Tracks for 2003-2010

(a) PR(PV) in Reanalysis

(b) PR(PV_c) in Reforecasts

(c) PR_c(PV_c) in Reforecasts

(d) SD of PR(PV) in Reanalysis

(e) RSR (colors) and RMSE for PR(PV_c) (contours)

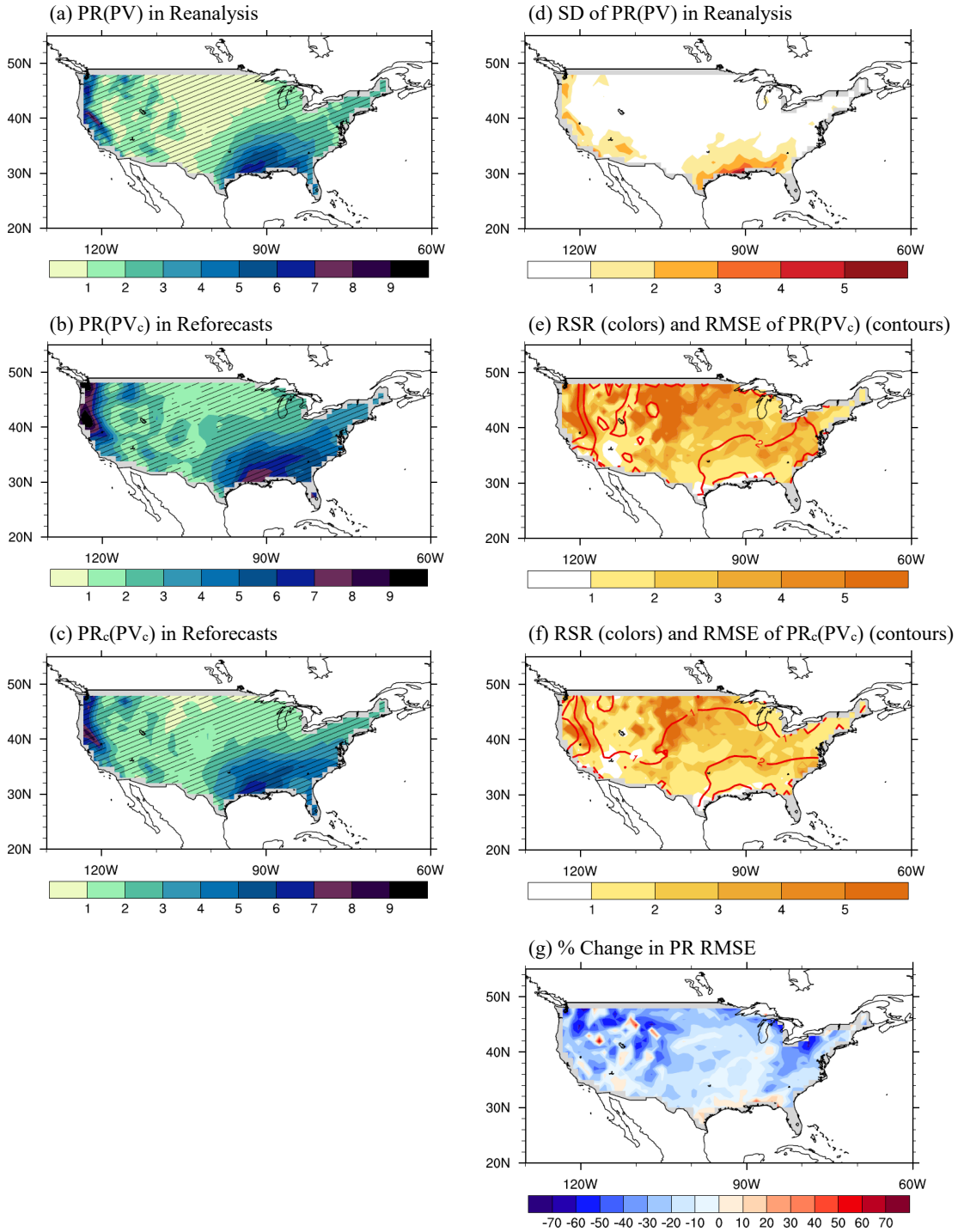(f) RSR (colors) and RMSE for PR_c(PV_c) (contours)

(g) % Change in PR RMSE

100
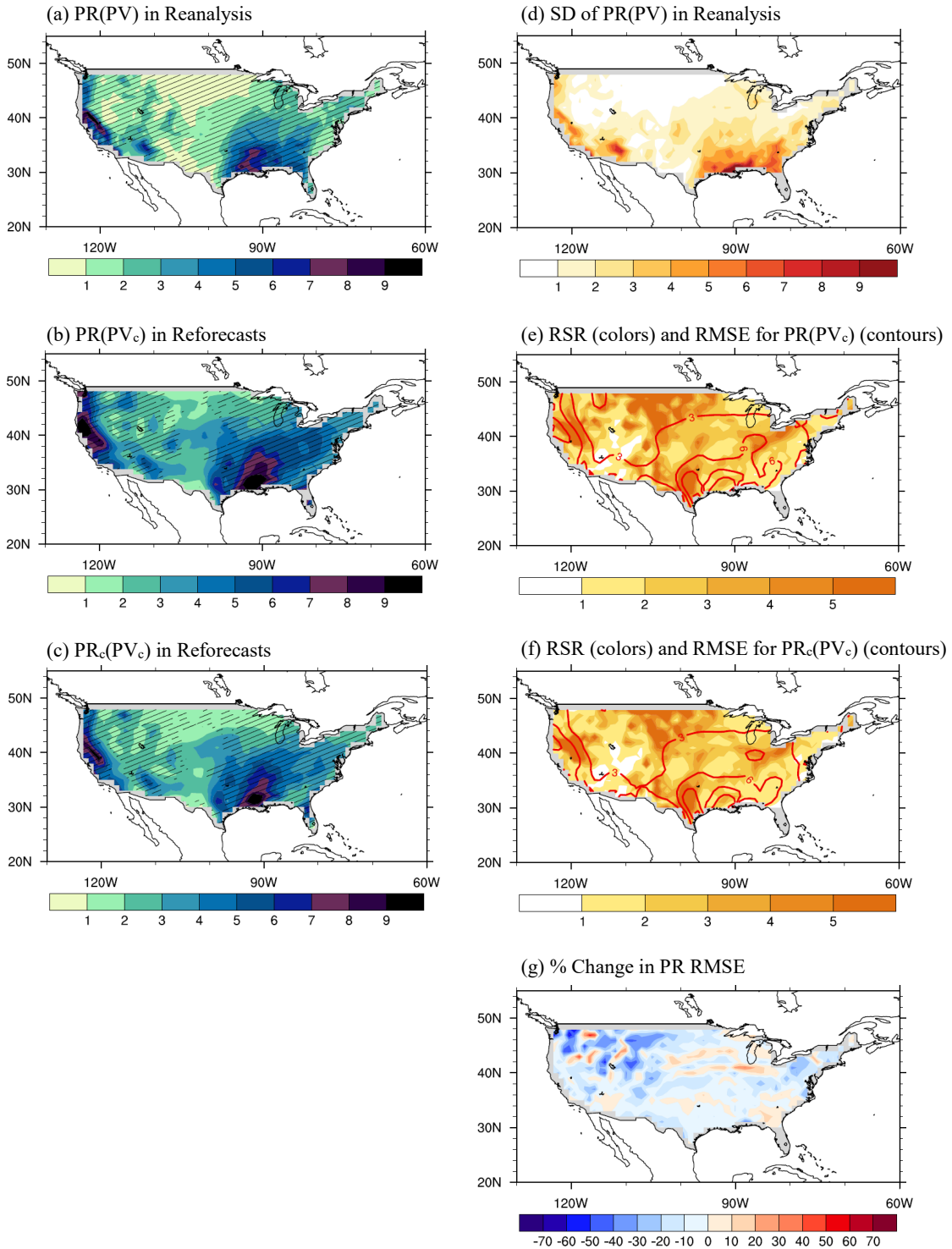
Figure 3.14: Mean strong-storm track-related daily precipitation rates (PR) during DJF for the validation period 2003-2010 in the contiguous US (CONUS). Left column: (a) CPC gauge-based analysis PR associated with reanalysis potential vorticity (PV) with T_{str} = 4.9 PVU; (b) weeks 3-4 reforecast PR associated with bias-corrected reforecast PV (PV_c) with T_{str} = 6.1 PVU; (c) bias-corrected weeks 3-4 reforecast PR (PR_c) associated with reforecast PV_c with T_{str} = 6.1 PVU. Hatched marks indicate statistical significance ($p < 0.05$). Right column: (d) Standard deviation (SD) of reanalysis PR(PV); (e) RMSE of weeks 3-4 reforecast PR(PV_c) (contours at 3 mm day^{-1} interval) and RSR (color shades; interval 1); (f) as in (e) but for the bias-corrected PR_c(PV_c); (g) Percent change in RMSE after all-storm PR bias is removed from reforecasts, shown at an interval of 10%. RSR is the ratio of RMSE of reforecast PR(PV_c) to SD of reanalysis PR(PV). Panels (a)-(d) are shown at an interval of 1 mm day^{-1}. Areas in CONUS with missing values and less than 0.5 storms per 10^6 km^2 per month in CFSR and where strong storms are not found are masked (gray shade).

3.14b) shares a similar spatial distribution to observations despite overestimations in precipitation intensity. Statistically significant strong-storm precipitation in the bias-corrected reforecasts is reduced (Fig. 3.14c) and more closely resembles observations. This is evident near the west coast and in the eastern United States.

The influence of the bias correction on strong-storm precipitation in CFSRR is depicted in Figs. 3.14d-g. As is shown for the all-storm precipitation, the SD of strong-storm precipitation is highest in the west and southeastern US (Fig. 3.14d). The RMSE of uncorrected strong-storm precipitation (Fig. 3.14e, contours) reveals large errors where the SD is high. The corresponding RSR (Fig. 3.14e, color shades) is larger in regions with low precipitation and lower in regions with high precipitation. The large RMSE and RSR are somewhat reduced after the bias correction (Fig. 3.14f). Despite the improvements, large biases in the corrected precipitation rates remain throughout much of CONUS. The percent change in RMSE for strong-storm precipitation (Fig. 3.14g) exhibits larger decreases in errors in regions that experience lower variability in strong-storm precipitation (see Fig. 3.14d). Smaller reductions in error are found in areas where the variability in strong-storm precipitation is high. The results suggest

that the bias correction in all-storm precipitation somewhat improves the representation of strong-storm precipitation in the weeks 3-4 reforecasts in CONUS. However, the reforecasts better capture the signal in precipitation in the all-storm tracks, suggesting that further analysis of more extreme precipitation is needed.

3.4.2 High Impact Weather related to the Strong-Storm Tracks

In this thesis, high impact or severe weather related to strong storms refers to hazardous winds or heavy precipitation. More specifically, following Klawa and Ulbrich (2003) hazardous near-surface wind speeds are those whose magnitudes exceed the 98th percentile (fall within the top 2%) of all wind speeds. Likewise, high impact/hazardous precipitation rates are defined as those that exceed the local 98th percentile, assuming that they are most likely to produce damage and loss.

For our computations, the 98% thresholds of wind and precipitation are obtained from all winds and precipitation for the base period (1983-2002) reanalysis regardless of the presence of storms, i.e., before any storm tracking is performed. Thresholds are computed for each winter and averaged to obtain a mean "climate" threshold. Then, strong-storm track-related winds or precipitation in the reforecasts during the validation period (2003-2010) are considered hazardous and likely to produce damages if they exceed the corresponding *climate* threshold. This is done in order to simulate forecast mode in operations. We also compute the reanalysis high impact weather cases for the validation period. In this way, reforecasts and reanalysis can be compared directly.

Figure 3.15 presents hazardous strong-storm wind intensity and frequency for the validation period 2003-2010. The reanalysis wind intensity (Fig. 3.15a) for strong storms is highest over the oceans affecting, e.g., maritime operations. On average, hazardous wind speeds over water are in the range from 18-26 m s^{-1} (~40-58 mph) over the open oceans near the continental coastlines. Over land, high impact winds related to the strong-storm tracks are found primarily in the central and eastern United States where they achieve speeds that exceed 14 m s^{-1} (~31 mph) on average.

Hazardous strong-storm wind speeds in 2003-2010 computed from the reforecasts are presented in Fig. 3.15b. The intensities of the winds correspond well with the reanalysis in the mid-latitudes, although they are slightly stronger in the storm track regions. This suggests that the reforecasts are capable of predicting high impact winds in winter in North America.

We further examine whether the bias correction has an effect on the prediction of high impact winds. Fig. 3.15c shows hazardous strong-storm wind speeds in the bias-corrected reforecasts. The bias-corrected reforecasts provide better areal coverage of hazardous strong-storm winds relative to the uncorrected reforecasts (Fig. 3.15b), although the wind magnitude does not noticeably change. This suggests that the bias correction has the potential to provide a more complete forecast of high impact strong-storm wind intensity at weeks 3-4 time scales.

It is of interest to examine not only the severe wind magnitudes but their frequency too. Frequency is defined as the percentage of time that the local 98th percentile threshold of wind speed is exceeded. The strong storm-no storm difference in frequency of high impact wind events in the strong-storm track regions is shown in

Hazardous Winds related to PV in Strong-Storm Tracks for 2003-2010
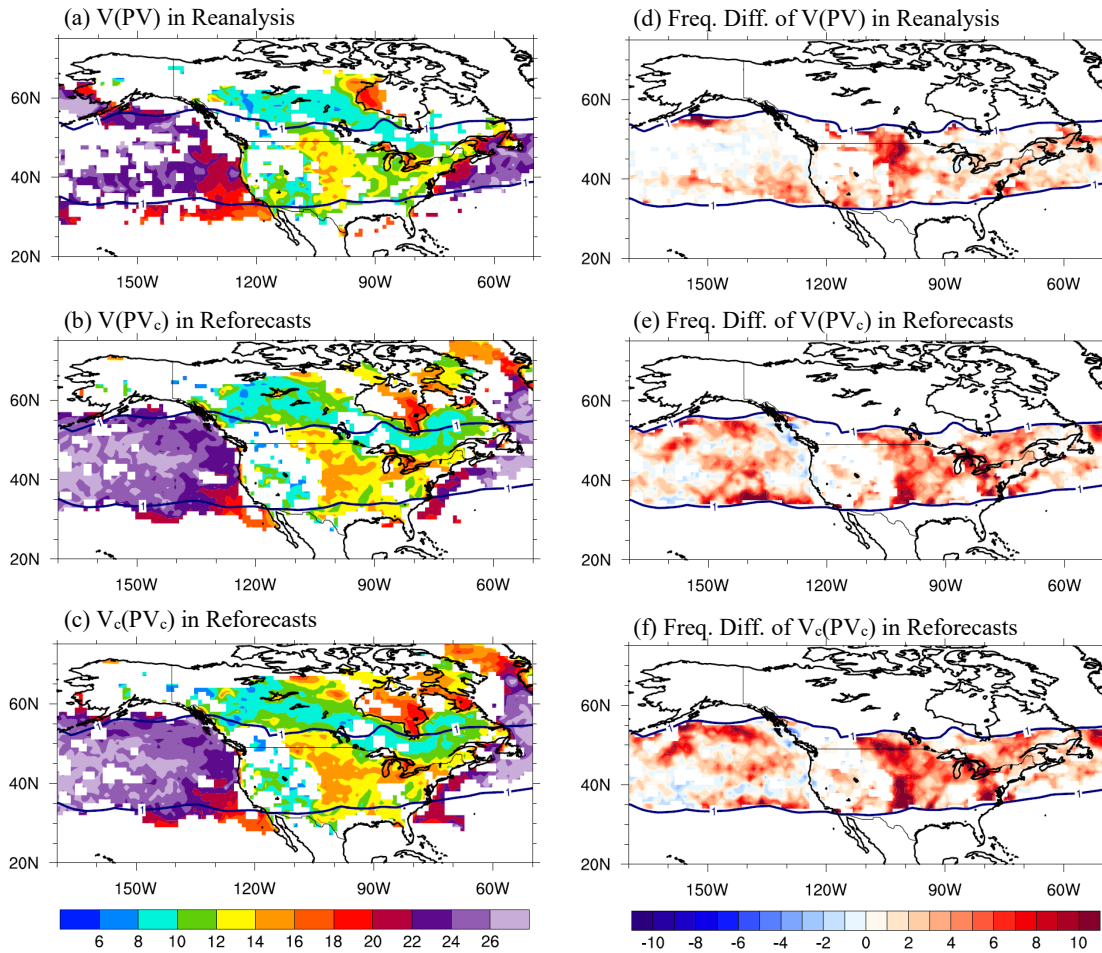
Figure 3.15: Mean hazardous near-surface winds related to the strong-storm tracks during DJF for 2003-2010. Wind speeds (V) that exceed the local 98th percentile are associated with (a) CFS reanalysis PV with T_{str} = 4.9 PVU, (b) bias-corrected reforecast PV (PV$_c$) with T_{str} = 6.1 PVU, and (c) bias-corrected reforecast PV$_c$ with T_{str} = 6.1 PVU. (d)-(f) as in (a)-(c) but showing the difference in frequency of hazardous wind events: difference in percentage of time that the local 98th percentile is exceeded between when strong storms are present and no storms are present. Contour interval for (a)-(c) is 2 m s^{-1}, and for (d)-(f) is 1%. In all panels, the mid-latitude strong-storm track density for CFSR is outlined by dark blue contours marking 1 strong storm per 10^6 km^2 per month. Panels (a)-(c) are masked where hazardous strong-storm winds are not found. In panels (d)-(f), areas outside of the strong-storm track regions are masked.

Figs. 3.15d-f. Not surprisingly, the frequency of high impact wind events in the

reanalysis increases when strong storms are present (Fig. 3.15d). This is particularly

evident over the oceans where the storm tracks are strong and over land in areas where

the winds are most intense. Wind frequency in the reforecasts is also shown to increase in the strong-storm track regions, with the bias-corrected reforecasts (Fig. 3.15f) providing better areal coverage of wind frequency relative to the uncorrected reforecasts (Fig. 3.15e). Further, the bias correction somewhat improves the change in frequency in the eastern North Pacific Ocean and central North America. In summary, we find that (a) during strong storms the frequency of hazardous wind events increases, and (b) the bias-corrected reforecasts reproduce better this increase relative to the uncorrected reforecasts.

As for heavy precipitation (not shown), the bias correction is found to offer little to no improvement in the representation of weeks 3-4 reforecasts of precipitation that exceed the local 98th percentile. Heavy precipitation intensity in the CPC gauge-based analysis resembles that shown in Fig. 14a, with the heavy precipitation intensity about one order of magnitude greater nearly everywhere in the mid-latitudes. Comparisons of the weeks 3-4 reforecasts versus the bias-corrected reforecasts reveal virtually no change in the magnitude of hazardous precipitation rates. Moreover, the reforecasts are found to underestimate the magnitude of precipitation intensity in the storm track regions relative to observations. Observations exhibit increases in the frequency of high impact precipitation events over CONUS when strong storms are present. The uncorrected and bias-corrected reforecasts overestimate precipitation frequency across CONUS, with the bias-corrected reforecasts exhibiting slightly lower values that are closer to observations (relative to the uncorrected reforecasts). The results imply that CFSRR is able to describe the spatial distributions but only the *relative* magnitudes of heavy strong-storm precipitation intensity and frequency at weeks 3-4 time scales.

In addition, we assess the dependence of the findings on the selected period of validation by conducting an identical strong-storm track analysis using a 20-year test base period (1991-2010) and an 8-year test validation period (1983-1990) in CFSRR (not shown). The results from the test analysis are generally consistent with those presented in this study. The reforecasts of storm track-related winds represent well the reanalysis, and the removal of systematic errors further improves the storm track-related weather reforecasts. Likewise, the reforecasts for the test validation period reproduce the characteristic hazardous strong-storm winds, again corresponding with this study's findings. Overall, the results of the test analysis indicate that our findings are robust.

3.5   *Analysis of Storm Track-Related Hybrid Level 1 Winds in the Reforecasts*

In Section 3.3 it was shown that the hybrid level 1 winds in the reforecasts exhibit a yet unexplained departure from the 1000-hPa winds in the reanalysis and reforecasts as well as from the reanalysis H1 winds (see Fig. 3.6). The results shown in Fig. 3.6 in particular prompt a related question: Can we extract any useful information on the prediction of storm track-related winds using the winds on the hybrid level 1 surface, despite their having large errors? In this section we attempt to answer this question by carrying out similar diagnostics to those presented for the 1000-hPa winds in Section 3.3.

We examine the relation of winds on the terrain-following hybrid level 1 surface to the winter all-storm tracks during the validation period 2003-2010 (Fig.

3.16). Fig. 3.16a shows that the all-storm winds in the reanalysis for the validation period 2003-2010 are statistically significant and stronger over the oceans where the storm tracks are more intense (see Fig. 3.2a), corresponding with the findings using 1000-hPa winds (Section 3.3). The all-storm track-related winds in the reforecasts (Fig. 3.16b) exhibit weaker wind speeds in the eastern North Pacific Ocean near the North American west coast, across the North Atlantic Ocean, and almost everywhere over land. Statistically significant negative biases in the H1 wind reforecasts for the base period 1983-2002 (Fig. 3.16d) emphasize the underestimation, following Eq. (3.2). Removal of the base period wind bias from the reforecasts of all-storm track-related H1 winds for the validation period 2003-2010 noticeably improves the reforecasts and increases the statistical significance in both ocean basins as well as over land east of the Rocky Mountains (Fig. 3.16c).

Figs. 3.16e-h present statistics of the all-storm H1 winds in the reanalysis and reforecasts. As is the case for the 1000-hPa winds, the SD of all-storm track-related H1 winds in the reanalysis is highest over the oceans in the lower mid-latitudes (Fig. 3.16e). Following Eq. (3.1), the RMSE of uncorrected all-storm H1 winds (Fig. 3.16f, contours) is relatively large in the northeast sectors of the North Pacific and North Atlantic Oceans as well as in the lower latitudes outside of the storm track regions. Over land, smaller errors in wind speed are found east of the Rocky Mountains. The corresponding RSR of all-storm winds is generally low (Fig. 3.16f, color shades), particularly in the lower mid-latitudes where the SD is highest. This suggests that the uncorrected reforecasts partially capture the variability in all-storm H1 winds, albeit to a lesser extent than for the winds at 1000 hPa. The bias correction reduces the RMSE

Hybrid Level 1 Winds related to PV in All-Storm Tracks for 2003-2010

(a) V(PV) in Reanalysis

(e) SD of V(PV) in Reanalysis

(b) V(PV$_c$) in Reforecasts

(f) RSR (colors) and RMSE of V(PV$_c$) (contours)

(c) V$_c$(PV$_c$) in Reforecasts

(g) RSR (colors) and RMSE of V$_c$(PV$_c$) (contours)

(d) Bias in Winds for 1983-2002

(h) % Change in Wind RMSE
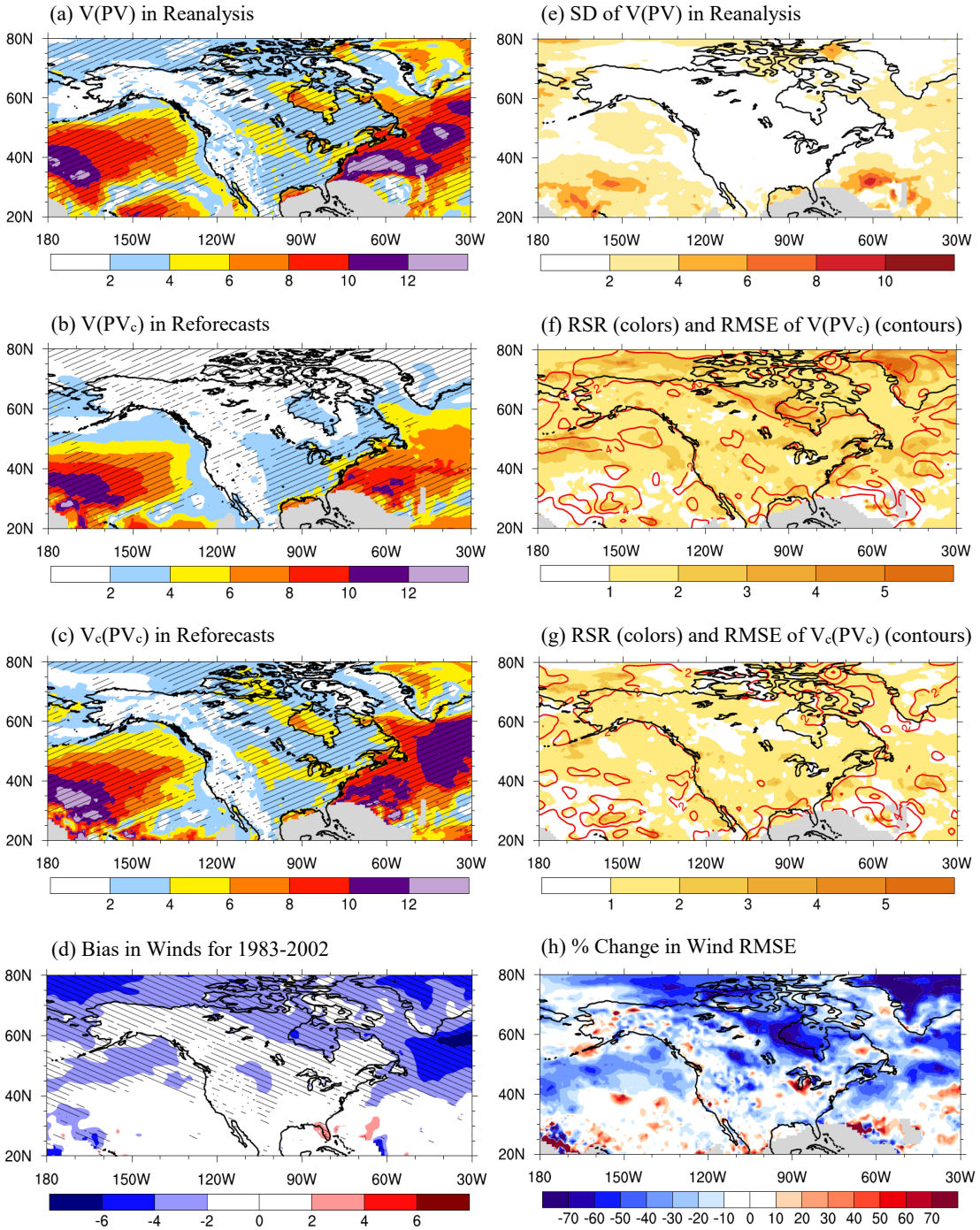
Figure 3.16: Mean all-storm track-related wind speed on the hybrid level 1 surface during DJF for the validation period 2003-2010. Left column: (a) CFS reanalysis wind speed (V) associated with reanalysis potential vorticity (PV); (b) weeks 3-4 reforecast wind speed associated with bias-corrected reforecast PV (PV_c); (c) bias-corrected weeks 3-4 reforecast wind speed (V_c) associated with reforecast PV_c; (d) wind bias for the base period 1983-2002 (reforecast minus reanalysis). Hatched regions in panels (a)-(d) are statistically significant ($p < 0.05$). Right column: (e) Standard deviation (SD) of reanalysis V(PV); (f) RMSE of weeks 3-4 reforecast $V(PV_c)$ (contours at 2 m s^{-1} interval) and RSR (color shades; interval 1); (g) as in (f) but for the bias-corrected $V_c(PV_c)$; (h) Percent change in RMSE after wind bias is removed from reforecasts, shown at an interval of 10%. RSR is the ratio of RMSE of reforecast $V(PV_c)$ to SD of reanalysis V(PV). Panels (a)-(e) are shown at an interval of 2 m s^{-1}. Areas with less than 0.5 storms per 10^6 km^2 per month in CFSR are masked (gray shade).

of the reforecast winds on the hybrid level 1 surface (Fig. 3.16g, contours), and its magnitude better corresponds with the reanalysis standard deviation as evidenced by the reduced RSR (Fig. 3.16g, color shades). This indicates that the bias-corrected reforecasts better depict the observed variability in all-storm track-related winds, and accordingly contain more useful information for the prediction of surface storm winds on the hybrid level 1 surface at weeks 3-4 time scales.

Negative values in the change in the RMSE further emphasize the improvements in the mid-latitude storm track regions over the oceans (Fig. 3.16h). The error in all-storm H1 wind speed is reduced on average by about 30% in the storm track regions. In the North Pacific Ocean the error is reduced by as much as 50%, and in the North Atlantic Ocean it is reduced by as much as 60%. Over land, the RMSE decreases by over 50% just east of the Rockies in the higher mid-latitudes and by 10%-40% near the eastern and southern coasts of the United States. Additionally, the removal of the base period H1 wind bias from the validation period reforecasts reduces the error in estimation in the high latitudes outside of the main regions of storm activity. In summary, the findings indicate that the CFS weeks 3-4 reforecasts of all-storm track-

related winds on the hybrid level 1 surface are improved once the bias in wind speed is removed.

We next assess the relation between strong-storm tracks and the hybrid level 1 winds in the weeks 3-4 reforecasts in the validation period 2003-2010 (Fig. 3.17). The strong-storm track-related winds in the reanalysis (Fig. 3.17a) are found to be most intense and statistically significant over the oceans and in eastern North America, again corresponding with the findings using the 1000-hPa winds (Section 3.3). The uncorrected reforecast of strong-storm H1 winds (Fig. 3.17b) shows generally weaker wind speeds in the mid-latitudes relative to the reanalysis in Fig. 3.17a. The bias-corrected winds related to the strong-storm tracks (Fig. 3.17c) are improved throughout the mid-latitude storm track regions, particularly in the northeastern oceans where the statistical significance has increased as well as in the southeastern US. Additional improvements are found at higher latitudes over Canada.

Statistics of the strong-storm H1 winds in the reanalysis and reforecasts are presented in Figs. 3.17d-g. The results for the hybrid level 1 wind analysis are similar to those for the 1000-hPa winds discussed in Section 3.3. Over the oceans, the SD of the reanalysis strong-storm H1 winds is relatively high (Fig. 3.17d), and the RMSE of uncorrected strong-storm winds is large (Fig. 3.17e, contours). Smaller errors are found over land. The RSR for the uncorrected reforecasts (Fig. 3.17e, color shades) is low in the storm track regions and is further reduced after the all-storm wind bias is removed (Fig. 3.17f). The percent change in strong-storm wind RMSE (Fig. 3.17g) exhibits decreases in error of 10%-50% over the northeast oceans and Canada.

Hybrid Level 1 Winds related to PV in Strong-Storm Tracks for 2003-2010
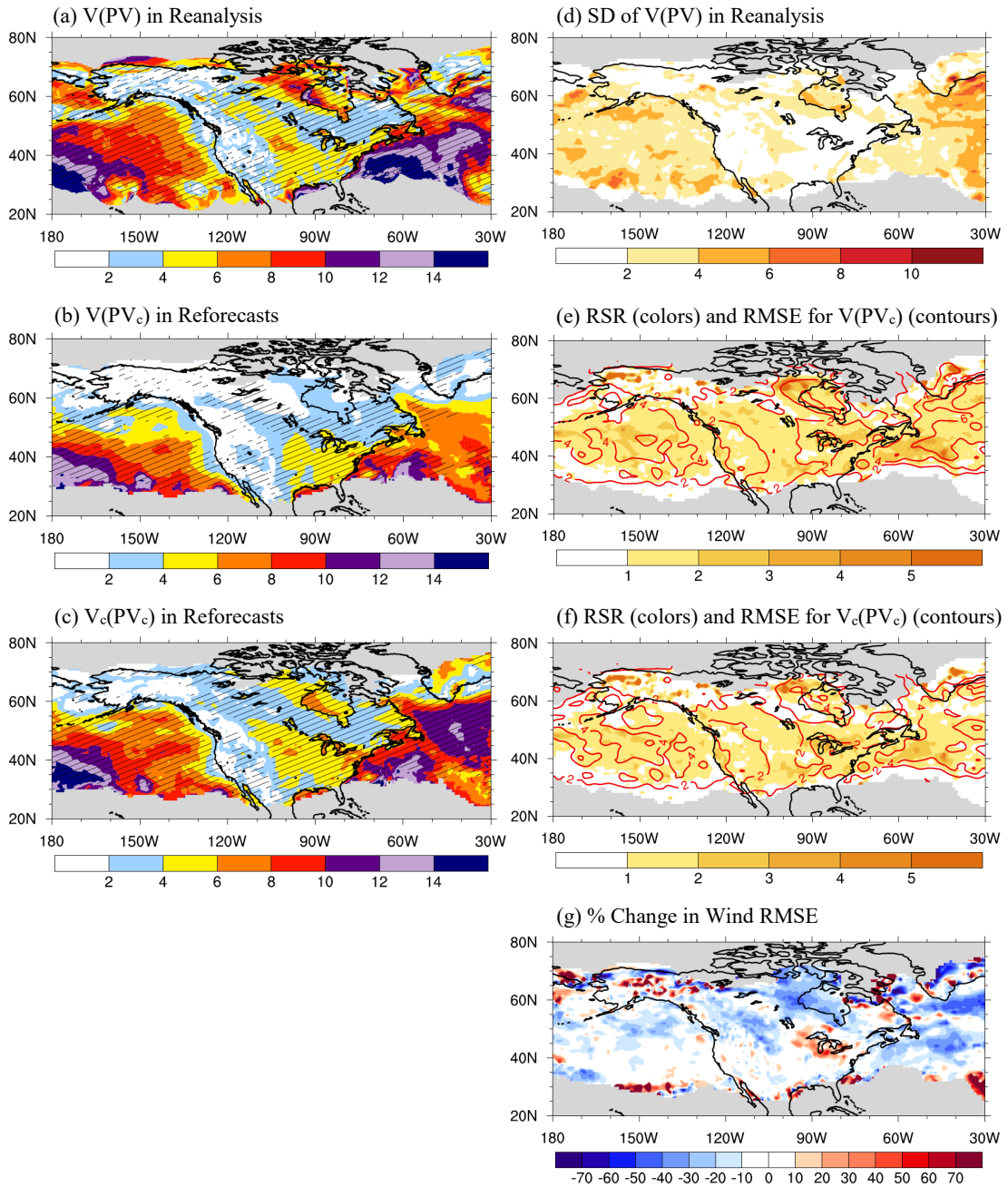
Figure 3.17: As in Fig. 3.13 but for winds on the hybrid level 1 surface.

The findings indicate that the bias correction improves the prediction of strong-storm winds on the hybrid level 1 surface at weeks 3-4 time scales.

Lastly, we examine the relation of high impact (top 2%) wind speeds at hybrid level 1 to the strong-storm tracks in 2003-2010 (Fig. 3.18). The reanalysis strong-storm winds on the hybrid level 1 surface (Fig. 3.18a) are most intense over the oceans and exhibit a similar range of wind speeds to the 1000-hPa winds. Over land, the high impact wind speeds related to the strong-storm tracks are highest in the eastern United States. The reforecasts (Fig. 3.18b) generally correspond with the reanalysis, although they exhibit much less areal coverage due to the negative bias in the wind reforecasts leading to fewer cases of H1 wind speeds that exceed the mean local 98th percentile. Some improvement in the H1 wind intensity is found over the oceans and over land east of the Rocky Mountains after the all-storm wind bias is removed (Fig. 3.18c). Moreover, the bias-corrected reforecasts provide better areal coverage of hazardous strong-storm winds at hybrid level 1, suggesting that the bias correction has the potential to improve the reforecasts of high impact strong-storm wind intensity at this level at weeks 3-4 time scales in North America. The strong storm—no storm difference in frequency of high impact wind speeds is also examined (Figs. 3.18d-f). As shown for the 1000-hPa winds, the frequency of high impact wind events on the hybrid level 1 surface increases in both the reanalysis (Fig. 3.18d) and reforecasts (Fig. 3.18e) when strong storms are present. The bias-corrected reforecasts (Fig. 3.18f) provide better areal coverage of wind frequency relative to the uncorrected reforecasts. In summary, we find that the bias correction improves the prediction of high impact wind events on the hybrid level 1 surface at weeks 3-4 time scales.

Hazardous Hybrid Level 1 Winds related to PV in Strong-Storm Tracks for 2003-2010
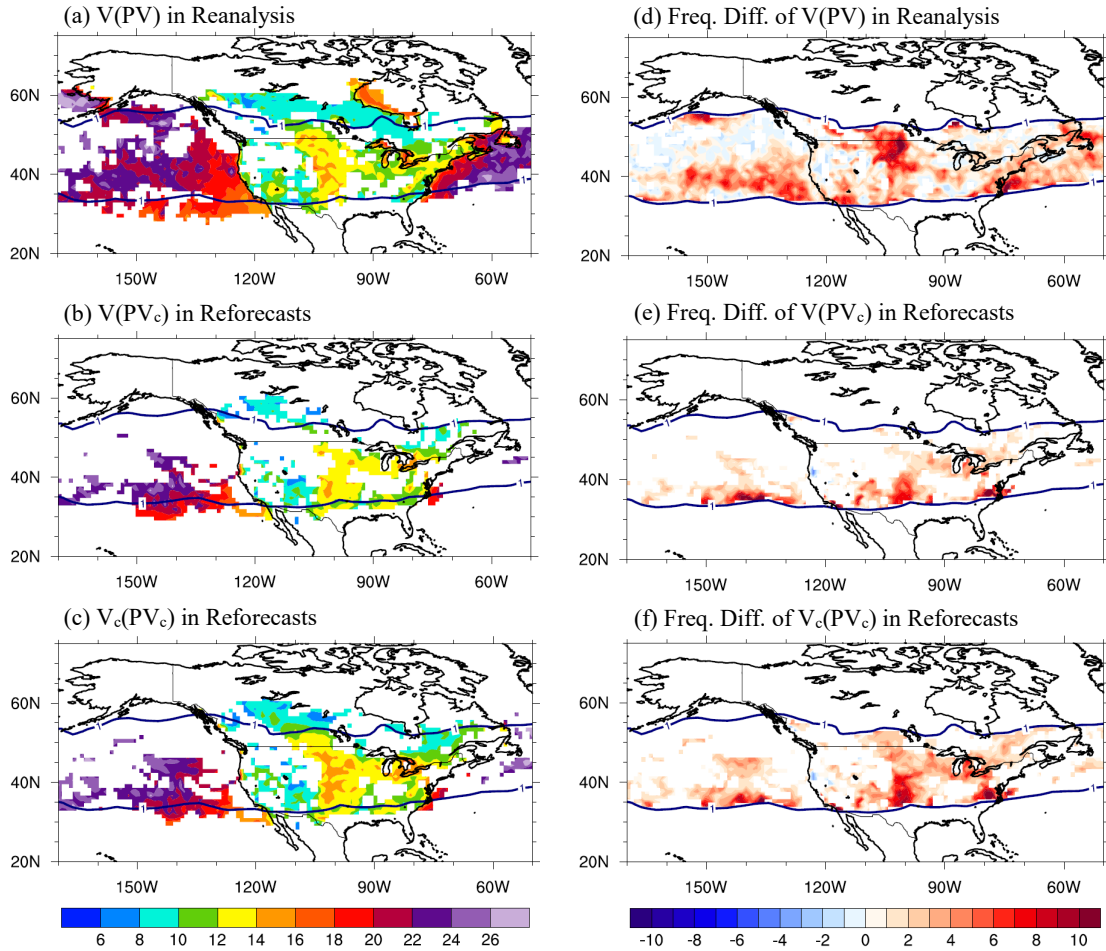
Figure 3.18: As in Fig. 3.15 but for winds on the hybrid level 1 surface.

3.6   *Summary and Conclusions*

The subseasonal-to-seasonal forecast range is considered a gap in operational weather prediction, and advancements at these time scales have the potential to provide valuable information for weather-related resource management decisions across environmental and economic sectors. To contribute to the understanding of S2S weather prediction in North America, we examined to what extent the CFSRR weeks

3-4 reforecasts reproduce the dynamic properties of storm tracks, and if the latter contribute to the prediction of the expected severe weather at those time scales.

The analysis was done for two categories of storm intensity: (a) all-storm tracks, which include all extratropical cyclones, and (b) strong-storm tracks, constituted by a subset of the more intense extratropical cyclones in terms of PV. The proportion of strong storms to all storms ranges between 15%-18% independent of region, period of analysis, and whether it was computed from reanalysis or reforecasts.

This study started by identifying the all-storm track properties as described from the CFS reanalysis in a 20-year base period (1983-2002). Similar diagnostics performed over the CFS weeks 3-4 reforecasts revealed statistically significant positive biases in PV_{320} intensity. Once the reforecasts were bias-corrected and storm tracks properties recomputed, the results were closer to those observed in the reanalysis. A good correspondence was found with previous studies that use different variables to identify storms (e.g., Hoskins and Hodges 2002; Hawcroft et al. 2016; Guo et al. 2017).

To assess the performance of the reforecasts in what would be a forecast mode in an 8-year validation period (2003-2010), we removed the 1983-2002 bias of PV_{320} intensity from the reforecasts. This correction reduced root mean squared errors in the PV intensity by as much as 50% in the oceanic storm track regions. Improvements were also found in other general features of the storm tracks including their track densities as well as the cyclogenesis, and cyclolysis densities, particularly in the eastern North Pacific and western North Atlantic Oceans. The results indicated that CFSRR is capable of reproducing the dynamics of storm track behavior at forecast weeks 3-4 after the

bias is removed, suggesting that reforecast storm tracks maintain enough signal to become potentially valuable for S2S weather prediction purposes.

Diabatic heating related to the storm tracks was examined to assess to what extent the reforecasts represent the observed symbiotic relation between storm tracks and diabatic heating. The weeks 3-4 reforecasts closely match the reanalysis in intensity and spatial distribution, with positive heating rates found over the oceans where the storm tracks are more intense. Small yet significant biases in heating intensity were found primarily over land. Removal of the average base period bias from the validation period reforecasts reduces the error in storm track-related heating over land but has little effect over the oceans. The findings indicate that the reforecasts already represent well the storm track-related heating in winter.

We next evaluated the relation of storm tracks to surface weather variables in the reforecasts to determine whether storm tracks are useful in the advancement of S2S weather prediction in North America. The spatial distributions of near-surface winds (winds at 1000 hPa) and precipitation associated with the reforecasts all-storm tracks in the base period (1983-2002) resemble those of the reanalysis. However, small yet significant biases were found in the magnitude of the winds, particularly in the northeastern North Atlantic Ocean and over land east of the Rocky Mountains. The small reforecast wind error in the validation period (2003-2010) was reduced on average by 12% by removing the base period wind bias. Specifically, our results showed that the error is reduced over the oceans where the storm tracks are strong as well as over land in the eastern US.

On the other hand, precipitation over the contiguous US is overestimated near the west coast and in the southeast. The removal of the 1983-2002 precipitation bias reduces the error in estimation for the validation period by 25% on average, although large biases remain where precipitation rates are highest. Further, after the biases are removed, the RMSE and ratio of the RMSE to the standard deviation decrease in the storm track regions, indicating that the bias-corrected reforecasts better represent the observed variability in storm track-related winds and precipitation.

The weeks 3-4 reforecasts represent well the strong-storm track-related high impact winds, as measured by wind intensity and frequency. It was shown that the reanalysis strong-storm winds are most intense over the open oceans and the eastern US. This is also reflected in the wind reforecasts in the regions of hazardous storm winds, with the bias correction resulting in better areal coverage of predicted high impact winds. The frequency of high impact wind events was found to increase in the reanalysis and reforecasts when strong storms are present, with the bias-corrected reforecasts able to better predict this increase in the eastern North Pacific Ocean and central North America relative to the uncorrected reforecasts. As for precipitation that exceeds the local 98th percentile, it is found that CFSRR is able to describe the spatial distributions and *relative* magnitudes of heavy strong-storm precipitation intensity and frequency at weeks 3-4 time scales, with the bias correction offering little to no additional improvement.

We also explored the use of hybrid level 1 wind reforecasts in the prediction of storm track-related winds. The spatial distributions of H1 winds associated with the all-storm tracks in the reforecasts for the validation period (2003-2010) resemble those at

1000 hPa. Relative to the reanalysis H1 winds, the magnitude of the reforecasts H1 winds is underestimated, particularly in the northeastern sectors of the oceans and over land east of the Rocky Mountains. The reforecast wind error was reduced on average by 30% by removing the base period H1 wind bias. Specifically, our results showed that over the oceans the error in the storm track regions decreases by 30%-60% and over land it decreases by 10%-50%.

Our findings indicate that CFSRR contains useful storm track-related information at weeks 3-4 time scales, supporting the potential contribution of storm track diagnostics to the advancement of subseasonal prediction of severe weather in North America. The bias correction has a minor positive impact on the prediction of storm tracks and related weather. As for storm winds on the hybrid level 1 surface, the bias correction noticeably improves the reforecasts by removing a large portion of the errors. Note that care should be taken regarding storm precipitation reforecasts, as the all-storm tracks better capture the signal in precipitation relative to the strong-storm tracks, suggesting further analysis will be needed.

The bias correction method used here is easily implemented, and this is useful for the rapid release of severe weather forecasts. Further, the approach can be applied to different operational model forecasts.

Chapter 4: Weeks 3-4 Prediction of Storm Tracks and Related Winter Weather in the CFSv2 Operational Forecasts for North America

Abstract: *The CFS version 2 (CFSv2) weeks 3-4 operational forecast performance is evaluated by identifying winter storms as PV_{320} anomalies and objectively tracking the temporal evolutions. Two periods of analysis are examined for winter (base: 2012-2016; validation: 2018) to assess the performance in forecast mode. The forecasts retain the ability to predict storm track properties as observed in CFSR and CFSRR, indicating that CFSv2 is generally able to characterize the evolution of winter storms in North America. Moreover, CFSv2 can predict similar latitudinal distributions of winter storms in both the Pacific and Atlantic regions. The storm intensity forecasts show statistically significant negative biases, which differ considerably from those in CFSRR. Negative PV biases are also present in the model climate and are apparently driven by mean static stability, with the relative vorticity component of PV acting as a secondary driver. CFSv2 reproduces well the observed variability in near-surface storm winds and the spatial distribution of storm precipitation. Small but significant wind biases are found in the storm track regions, and significant positive biases in storm precipitation are found throughout CONUS. Bias corrections further improve wind forecasts as well as precipitation forecasts where lower precipitation rates occur. In forecast mode, bias corrections yield minor improvements in the oceanic Atlantic sector only and not as well in the Pacific. The findings indicate that CFSv2 weeks 3-4 operational forecasts do contain useful storm track-related information and support that storm track characterization is valuable for operational S2S prediction.*

The key finding of Chapter 3 asserts that the CFS weeks 3-4 reforecasts contain useful storm track-related information for the advancement of S2S prediction in North America. Based on the findings in Chapter 3, we anticipate that the NCEP CFS version 2 (CFSv2) operational forecasts also contain useful information regarding storm track-related weather at weeks 3-4 time scales.

The study presented in this chapter evaluates the performance of CFSv2 operational forecasts from a storm-focused perspective for the advancement of S2S prediction of storm-related weather in North America. The work is based on the conceptual analysis in Chapter 3 and is expanded to include separate forecast assessments for each storm track (Pacific and Atlantic) that can influence North American weather. The main objectives are (a) to explore the application of storm track diagnostics in subseasonal-to-seasonal prediction in the CFSv2 *operational* forecasts in North America, and (b) to examine whether additional forecast information can be obtained by way of removing systematic errors in the storm tracks and related weather. Additionally, we investigate the origin of PV biases found in the storm track forecasts to better understand the characterization of PV in the model.

Chapter 4 is organized as follows. Section 4.1 provides an overview of the CFSv2 model and its use in operational experiments. Section 4.2 describes the data and analysis methods used here. Section 4.3 discusses the PV in the storm track forecasts and explores the origin of the PV biases. Section 4.4 discusses the storm track-related weather in the forecasts as constituted by near-surface winds and surface precipitation. Section 4.5 summarizes the findings.

4.1 Overview of CFSv2

The CFSv2 (Saha et al. 2014c) is the second version of the CFS operational forecast model at NCEP, and it became operational in March 2011. Since then, it has been upgraded and used for different opportunities. It is a coupled model that includes atmospheric, land surface, ocean, and sea ice components. The model employs upgraded data assimilation and forecast system components and produces global operational forecasts every 6 hours. The forecasts are archived on a 1° x 1° latitude-longitude grid at 64 vertical atmospheric sigma-pressure levels. Initial conditions for the model are provided by the real-time operational Climate Data Assimilation System version 2 (CDASv2; Saha et al. 2011; Saha et al. 2014c) analysis, which is the real-time continuation of CFSR.

The skill of CFSv2 forecasts of standard variables including precipitation, sea surface temperature, tropical convection, etc. has been previously evaluated at subseasonal and seasonal lead times (e.g., Saha et al. 2014c; Tian et al. 2017; Weber and Mass 2017). Over land the seasonal prediction of 2-m temperature is improved in the CFSv2 and is attributed to an increase in greenhouse gas concentrations that were missing in version 1 (CFSv1), while over the oceans sea surface temperatures are found to somewhat improve (Saha et al. 2014c). Based on reforecasts, the skill of CFSv2 is found to be generally higher than that for the original version of the CFS (CFSv1) (Saha et al. 2014c), and it is suggested that it is comparable with that of the European Centre for Medium-Range Weather Forecasts (ECMWF) System 4 (Kim et al. 2012). This is particularly evident for MJO prediction at a lead time of 1-2 weeks. CFSv2 forecast skill is largely dependent on the temporal lead time, season, and region of interest (Tian

120

et al. 2017). In DJF, precipitation in CFSv2 exhibits high skill in terms of consecutive days with precipitation throughout much of CONUS, with mean precipitation showing moderate skill in the southern parts of the US (Tian et al. 2017).

4.2   *Data and Methodology*

4.2.1   CFSv2 Operational Forecast Data

This study examines 6-hourly CFSv2 operational forecasts at the weeks 3-4 lead time taken from the 9-month prediction runs initialized at 0000 UTC. The 6-hourly operational analysis CDASv2 complements the CFSv2 forecasts and is considered "truth" for the purposes of this work. A 5-winter base period (2012-2016) is the main focus of analysis in this chapter where biases in the forecasts are identified. Bias corrections are applied to the base period and a 1-winter validation period (2018) to test for improvements in the representation of storm tracks and related weather in the CFSv2 in forecast mode. Note that the winter of 2016-17 is omitted from this study. This is because the weeks 3-4 forecasts for DJF 2016-17 were not made available by NCEP.

4.2.2   Analysis Methods

Following the methodology in Chapters 2 and 3 and in Hoskins and Hodges (2002), storms are identified as isentropic PV anomalies on the 320-K surface and tracked through time. The PV anomalies must exceed a low threshold of 0.5 PVU, and are further filtered to remove any storms that do not achieve a maximum intensity larger than T_{all}, a relatively low threshold defined by Eq. (2.2). Table 4.1 shows the values

Table 4.1: Values of average storm PV$_{320}$ maximum ($\overline{PV}_x$) and PV$_x$ standard deviation (SD) used to compute all-storm threshold T$_{all}$ for the operational analysis and weeks 3-4 forecasts. Thresholds are obtained from all identified cyclones in the NH winter in the base period 2012-2016. Units are PVU.

NH 2012-2016 Units: PVU	$\overline{PV}_X$	$(PV_X)_{SD}$	T_{all}
Analysis	3.2	1.4	1.1
Forecasts	2.4	1.1	0.75

used to compute T$_{all}$ for the operational analysis and weeks 3-4 forecasts. Both thresholds were obtained from the base period 2012-2016 and are used for both the base period and validation period diagnostics where forecast biases are removed in an attempt to enhance the performance of the operational model.

The properties of each storm track are described using statistics derived from the storm trajectories, and their computation is described in Chapters 2 and 3. To summarize, the track density shows the number of storms per unit area per month, representing the storm track pattern. The genesis and lysis densities represent the first and last detected points of the PV storms, respectively. The mean intensity statistic denotes the average strength of the storm tracks.

The relation of near-surface winds (winds at 1000 hPa) and surface precipitation to PV in the storm tracks in the forecasts is also investigated. Following Lukens et al. (2018) and as previously stated in Chapters 2 and 3, winds that are found within a 5-degree circular area around each storm center are considered to be associated with that storm center as this represents the area around the core of the storm where the winds are largely affected. Likewise, a 12-degree circular area is used for precipitation diagnostics, as this is the average size of a storm precipitation footprint.

A few statistics are used to assess the performance (deterministic skill) of the forecasts, including the root mean squared error (RMSE). Following Eq. (3.1), the RMSE measures the error in seasonal variation in the forecasts relative to what is observed. Additionally, the ratio (RSR) of the forecast RMSE to the SD of the operational analysis is used to evaluate how well the observed seasonal variability is represented in the forecasts. Lower RSR values indicate better model performance (Moriasi et al. 2007), with values less than 1 denoting that error variance is less than signal variance.

The mean absolute error (MAE) is computed for the validation period 2018. In general, the MAE represents the typical magnitude of forecast error, as it measures the absolute difference between the forecast means and the operational analysis means for the period. Lower values indicate smaller errors and larger values indicate larger deviations between the forecasts and observations. The MAE is computed following Eq. (4.1):

$$\text{MAE} = \frac{1}{n}\sum_{i=1}^{n}|Y_i - X_i| \qquad\qquad (4.1)$$

where X and Y are the storm track PV intensities for the reanalysis and the reforecasts respectively averaged for each winter *i*, and where *n* is the total number of winters in the period. Differences in the MAE quantify the change in error after bias corrections are applied.

4.3   *Storm Tracks in the Weeks 3-4 Operational Forecasts*

This section describes the properties of each storm track that can affect North American weather in the CDASv2 analysis (the extension of CFSR) and in the CFSv2

weeks 3-4 forecasts. The minimum thresholds that storms in the operational analysis and forecasts must achieve to be retained in the storm track analysis are shown in Table 4.1, following Eq. (2.2). Storms in the operational analysis and forecasts must achieve maximum intensities greater than 1.1 PVU and 0.75 PVU, respectively. The differences in the thresholds are due to differences in the mean PV values and standard deviations. The Pacific storm track is shaped by storms that develop over the North Pacific Ocean, and the North American-Atlantic (NAA) storm track is shaped by storms that develop over eastern North America and the western North Atlantic Ocean.

Figure 4.1 presents the number of winter storms per latitude in the NH for 2012-2016 (gray lines) and the percentage of those storms that develop in the Pacific region and in the Atlantic region (where red lines indicate the CDASv2 analysis and blue lines the CFSv2 forecasts). The latitude distribution of all NH storms in the forecasts closely matches the analysis (Fig. 4.1, gray colors), with the maximum number of storms found in the mid-latitudes around 45°N in both datasets. Distributions of the percentage of storms that develop in either storm track region in the forecasts closely match those in the analysis. High correlations between the datasets further illustrate the relationship: 0.87 in the Pacific region and 0.79 in the Atlantic region. The percent fraction of storms in the Pacific region ranges from about 10%-40% in both the analysis and forecasts (Fig. 4.1a), with the highest fraction of storms found around 40°N. Storms that develop in the Atlantic region represent about 5%-50% of all winter storms in either dataset (Fig. 4.1b), and the largest percentage of storms is found in the higher mid-latitudes around 50-60°N. In general, the results indicate that CFSv2 weeks 3-4 forecasts are able to predict the observed distributions of winter storms in each storm track region.
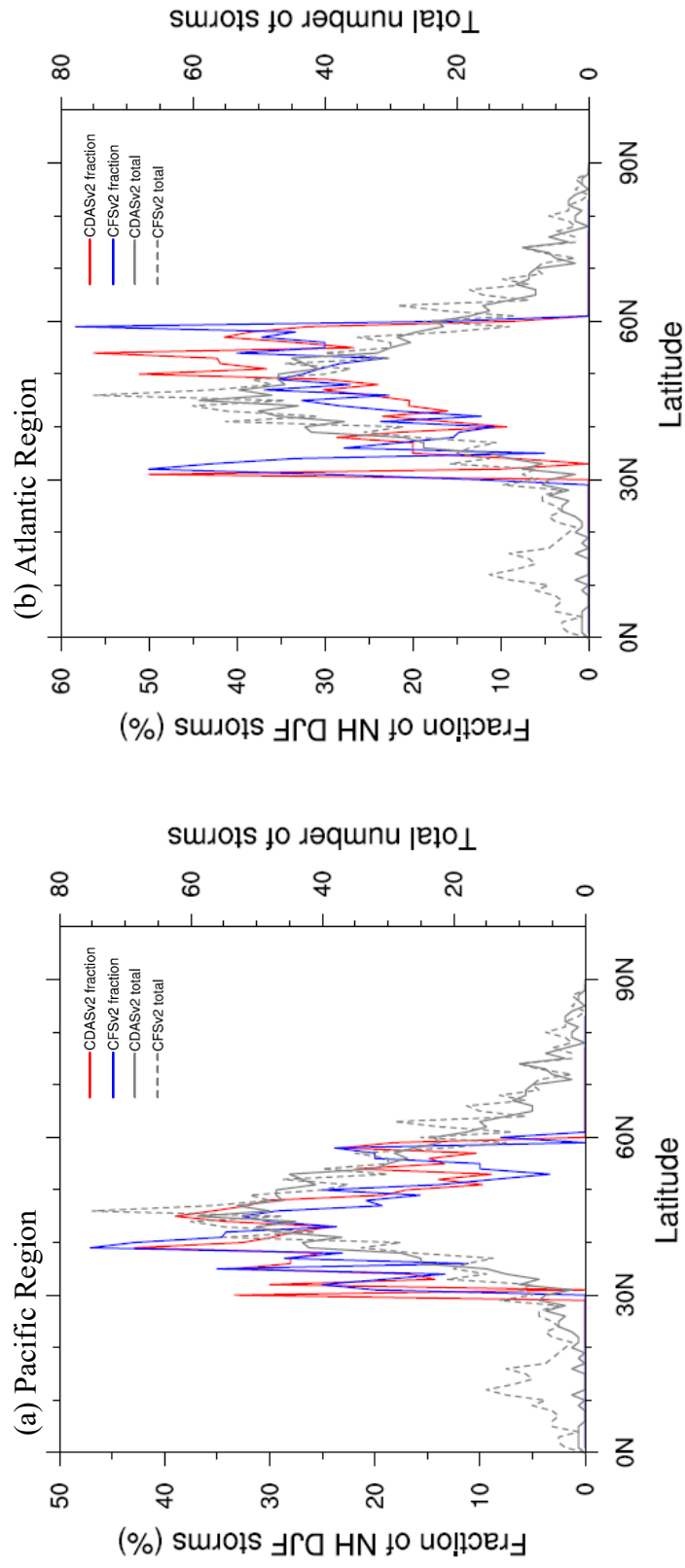
Figure 4.1: Number of storms versus latitude during DJF for 2012-2016 in the Pacific region (30-60°N, 150°E-130°W) (left column), and the Atlantic region (30-60°N, 120°W-20°W) (right column). (a) The percent fraction of all NH storms that develop in the Pacific storm track region at each latitude in the CDASv2 operational analysis is indicated by red colors, while the CFSv2 weeks 3-4 forecast fraction is indicated by blue colors. (b) as in (a) but for the NAA storm track region. Gray lines indicate the total number of storms in the NH in (solid lines) the analysis, and (dashed lines) the weeks 3-4 forecasts.

4.3.1   Storm Track Properties

Fig. 4.2 presents the trajectories of PV_{320} storms that develop in the storm track regions for 2012-2016. In the Pacific region in the operational analysis (Fig. 4.2a), storms tend to develop over the ocean and propagate eastward towards North America. As they move over land, the storms shift southeastward toward central North America. In the same region in the weeks 3-4 forecasts (Fig. 4.2b), storms follow a similar flow pattern to those in the analysis, with the forecasts exhibiting smoother trajectories. In the NAA storm track region in the analysis (Fig. 4.2c), the storm trajectories follow the SW-NE orientation of the storm track and extend northeastward from eastern North America toward Iceland. The storms tend to cluster around southeastern Canada/northeastern US, an "attractor" region that tends to exhibit increased baroclinic instability (see Fig. 2.4a), before dispersing across the mid-latitudes over the open ocean. The forecast storms follow a similar pattern (Fig. 4.2d).

From the storm trajectories we compute statistics (track, genesis, and lysis densities and mean PV intensity) that provide a more complete picture of the behavior of the Pacific and NAA storm tracks in the analysis and weeks 3-4 forecasts. Statistics for the Pacific storm track for 2012-2016 are presented in Fig. 4.3, and those for the NAA storm track are shown in Fig. 4.4.

Statistics representing storm track behavior in the Pacific region in the 2012-2016 CDASv2 analysis (Figs. 4.3a-d) correspond well with findings from previous studies (e.g, Hoskins and Hodges 2002; Lukens et al. 2018). The track density is highest over the North Pacific Ocean (Fig. 4.3a). The mean PV intensity of the Pacific storm track in the CDASv2 analysis (Fig. 4.3b) is strongest over the eastern North Pacific
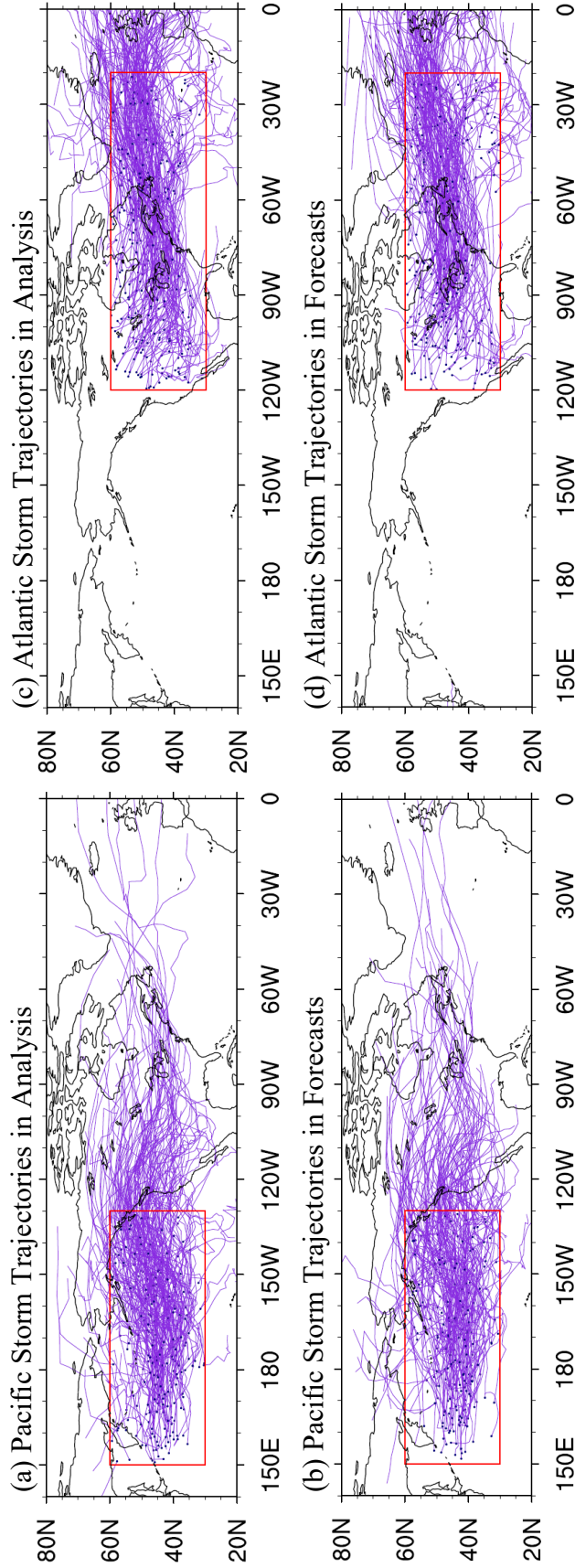
Figure 4.2: PV$_{320}$ storm trajectories during DJF for 2012-2016 that develop in (left column) the Pacific region (30-60N, 150E-130W), and (right column) the Atlantic region (30-60N, 120W-20W). Top row (a,c) displays the operational analysis, and bottom row (b,d) shows the weeks 3-4 operational forecasts. The regions of storm development in each basin are outlined in red.

Ocean and over land in the western United States. Cyclogenesis (Fig. 4.3c) is found upstream of track density and mean intensity maxima, while small scale lysis features are found downstream (Fig. 4.3d). In general, Pacific storms tend to develop over the central North Pacific Ocean and propagate northeastward where they intensify near the Canadian west coast. As they move over land, the storms shift southeastward due to the orographic effects of the Rocky Mountains (Brayshaw et al. 2009; Chang 2009). The PV storms that successfully propagate over the mountains are reinvigorated farther south, as indicated by the local track density maxima over land. These reinvigorated Pacific storms tend to propagate eastward, likely influenced by the dynamic flow of the NAA storm track in the region. In general, Pacific storms tend to dissipate in the northeastern North Pacific Ocean and over land between western Canada and the central US.

The Pacific storm track properties in the weeks 3-4 forecasts for 2012-2016 (Figs. 4.3e-h) resemble those in the operational analysis. Differences are found in the magnitudes. Specifically, the operational forecasts tend to underestimate the track density in the eastern North Pacific Ocean (Fig. 4.3e) and overestimate the number of developing storms in the central ocean (Fig. 4.3g). Moreover, cyclogenesis is noticeably underestimated relative to the analysis in the northeastern basin (see Fig. 4.3c). The lysis density in the forecasts (Fig. 4.3h) exhibits isolated cyclolysis features downstream of the track density maximum in agreement with the CDASv2 analysis (see Fig. 4.3d). These features are slightly displaced to the northeast over the ocean and western part of the continent relative to the analysis. As for the PV intensity (Fig. 4.3f), the forecasts share similar spatial distributions with the analysis, but exhibit lower
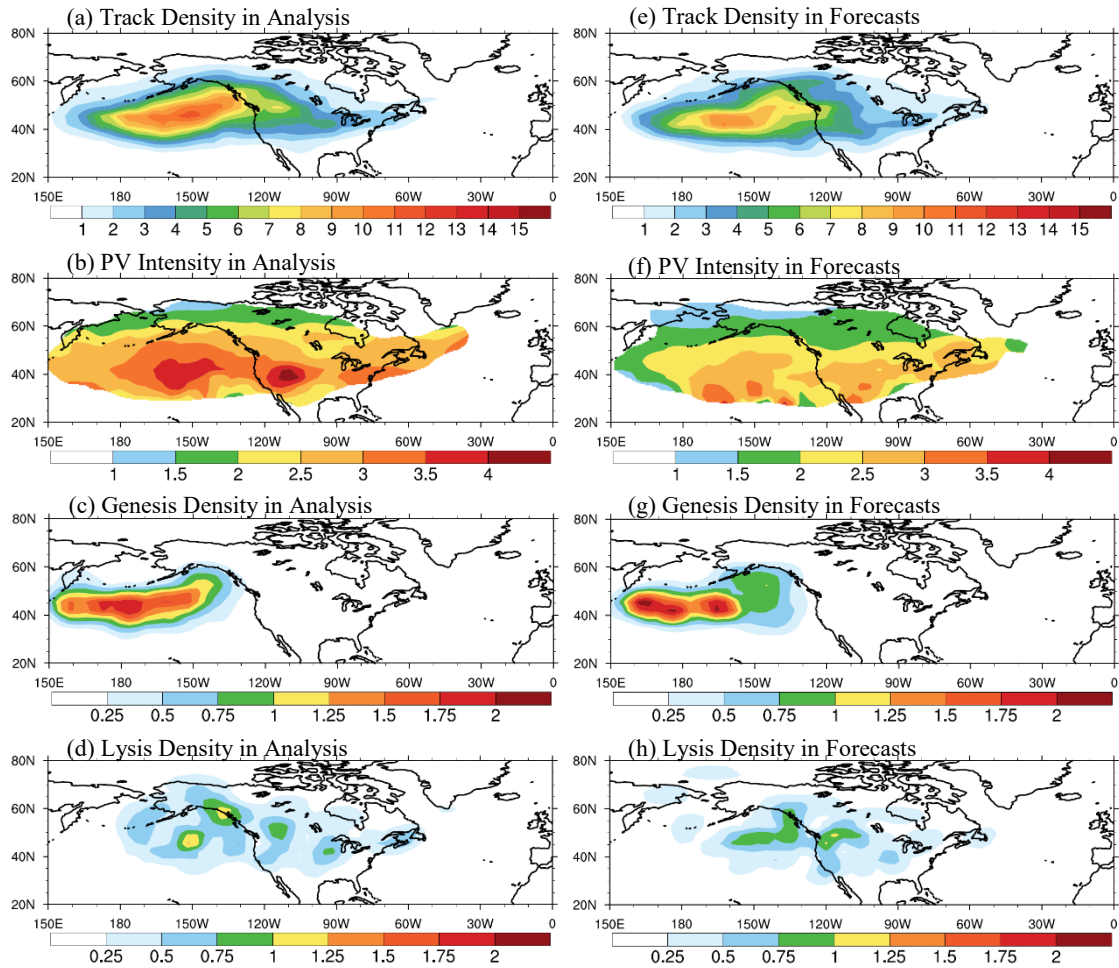
Figure 4.3: Density statistics of the Pacific storm track during DJF for 2012-2016. First and second columns depict the CDASv2 analysis and CFSv2 weeks 3-4 forecasts, respectively. Top (a,e), upper-middle (b,f), lower-middle (c,g) and bottom (d,h) rows respectively show track density, mean PV intensity, genesis density, and lysis density. Units for all density panels are storms per 10^6 km² per month. Track densities are shown at intervals of 1, while genesis and lysis densities are shown at intervals of 0.25. Intensity panels are shown at an interval of 0.5 PVU, with areas with fewer than 0.5 storms per 10^6 km² per month masked.

intensity values virtually everywhere in the region, indicating that the operational

forecasts underestimate the storm track intensity at weeks 3-4 time scales.

The North American-Atlantic storm track exhibits similar behavior (Fig. 4.4),

and is in good agreement with the findings presented in other studies (e.g., Hoskins and

Hodges 2002; Lukens et al. 2018). The storm track extends northeastward from eastern

North America to the northeastern North Atlantic (Fig. 4.4a) and is relatively strong throughout the region (Fig. 4.4b). The genesis (Fig. 4.4c) and lysis densities (Fig. 4.4d) show that over land storms tend to develop in eastern North America, with some dissipating before reaching the east coast. Over the North Atlantic Ocean near the east coast, storms either reinvigorate or newly develop before propagating northeastward, following the SW-NE orientation of the North American coast and nearby low-level baroclinic region (see Fig. 2.4a). Over the ocean, storms tend to dissipate south of Greenland and in the eastern basin near the United Kingdom. The weeks 3-4 forecasts exhibit similar NAA storm track properties (Figs. 4.4e-h). However, cyclogenesis features in the forecasts (Fig. 4.4g) exhibit higher magnitudes over land and lower values over the ocean near the east coast. Likewise, the lysis density features in the forecasts (Fig. 4.4h) show slightly higher magnitudes in the northeast ocean basin. As was found in the Pacific, the PV storm intensity is underestimated in the Atlantic region (Fig. 4.4f). Despite the discrepancies in magnitude, the findings generally support that the CFSv2 forecasts are able to reproduce observed winter storm track behavior in each storm track region at the weeks 3-4 lead time.

The negative bias in PV_{320} is more clearly seen in Fig. 4.5a that depicts the systematic error in the storm intensity forecasts for 2012-2016 (weeks 3-4 forecasts minus operational analysis), following Eq. (3.1). Large statistically significant negative biases in CFSv2 are found throughout the mid-latitudes, in particular in the northeastern ocean basins as well as over land. Following the methodology in Chapter 3, we remove the average storm PV_{320} bias in CFSv2 (relative to the CDASv2 analysis) from the intensity of each storm identified in the storm track forecasts in order to obtain a more
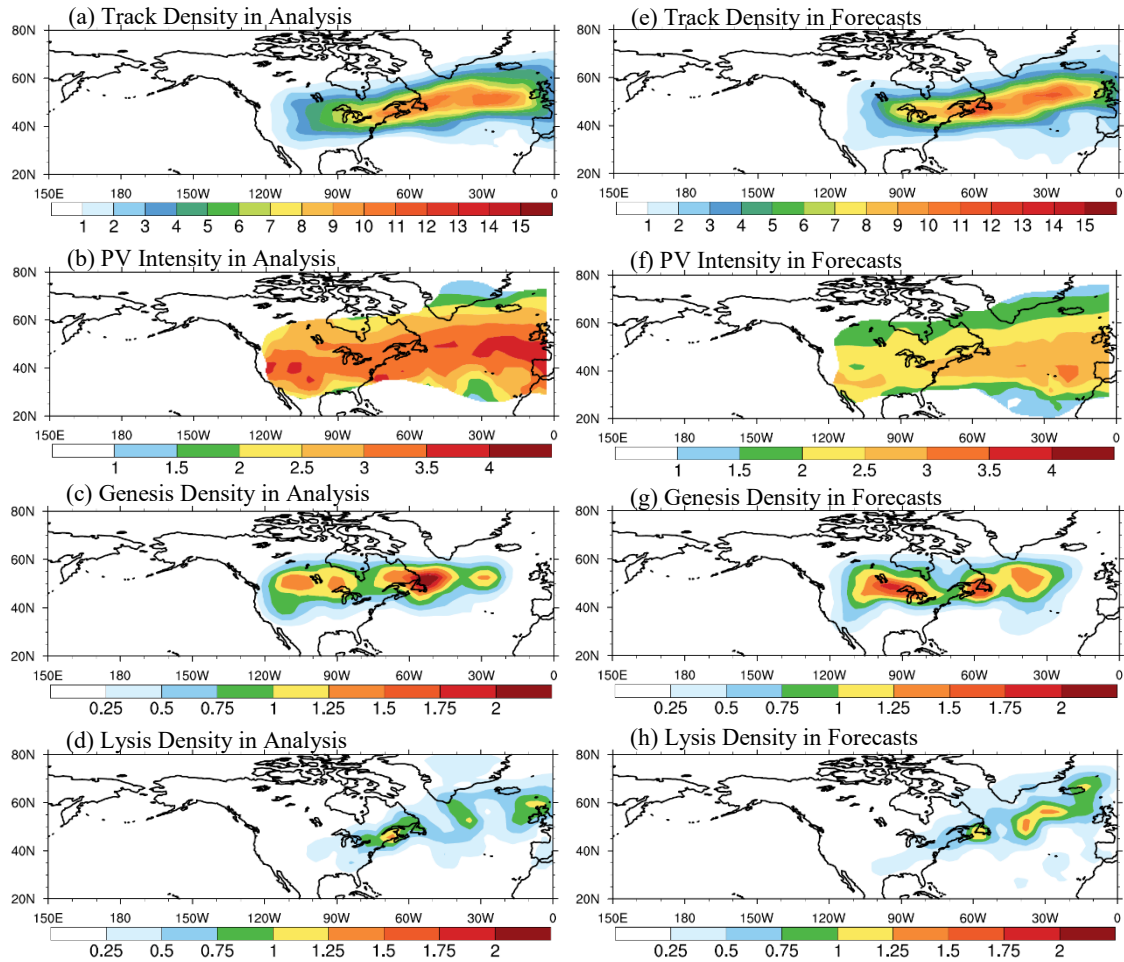
Figure 4.4: Density statistics of the North American-Atlantic storm track during DJF for 2012-2016. First and second columns depict the CDASv2 analysis and CFSv2 weeks 3-4 forecasts, respectively. Top (a,e), upper-middle (b,f), lower-middle (c,g) and bottom (d,h) rows respectively show track density, mean PV intensity, genesis density, and lysis density. Units for all density panels are storms per 10^6 km^2 per month. Track densities are shown at intervals of 1, while genesis and lysis densities are shown at intervals of 0.25. Intensity panels are shown at an interval of 0.5 PVU, with areas with fewer than 0.5 storms per 10^6 km^2 per month masked.

realistic representation of predicted storm track strength. Fig. 4.5b depicts the percent change in RMSE in the Pacific storm PV intensity after the bias is removed from the forecasts. The RMSE is shown to decrease considerably throughout the storm track region, in particular where the biases are large and the track density is high (see Fig. 4.3a). (Results are similar for the NAA storm track and thus are not shown.)

(a) PV Bias in CFSv2

(b) % Change in RMSE in Pacific
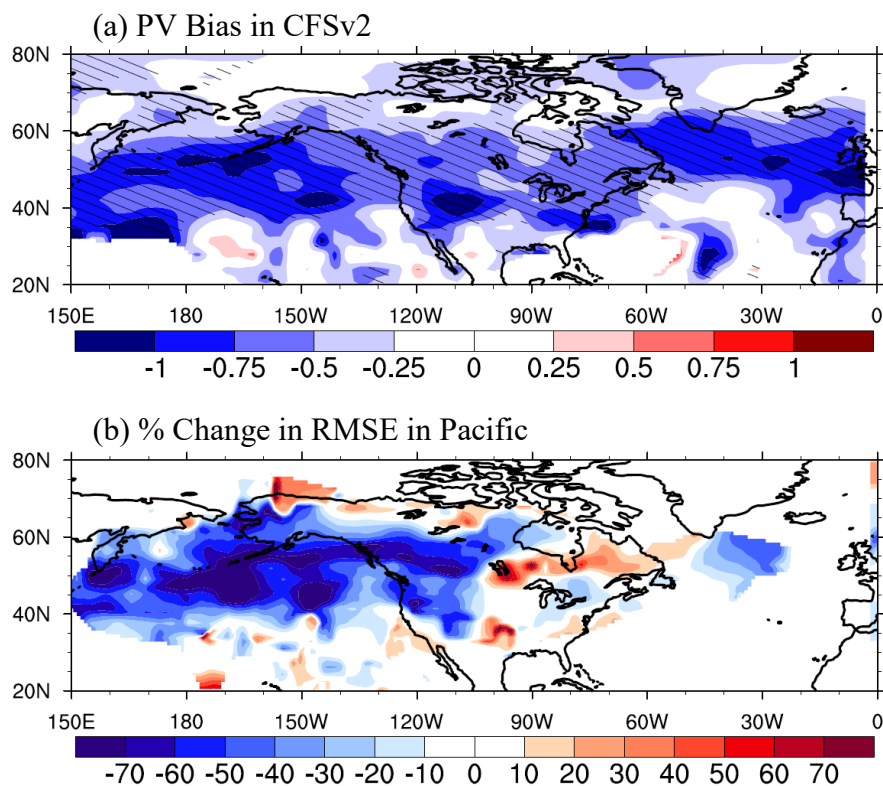
Figure 4.5: Error statistics of storm PV_{320} intensity at 320 K during DJF for 2012-2016. (a) Average bias in CFSv2 weeks 3-4 forecasts relative to CDASv2 analysis for 2012-2016, and (b) percent change in RMSE in the Pacific storm track region after PV bias is removed. Hatched marks in (a) indicate statistical significance ($p < 0.05$). Contour interval in (a) is 0.25 PVU, and in (b) is 10%. Areas with fewer than 0.5 storms per 10^6 km^2 per month are masked.

We have found that while removing the CFSv2 bias improves the PV intensity in the operational forecasts, it does not noticeably improve the representation of storm track density properties, which was our reasoning for correcting the PV in the analysis in Chapter 3. (The bias-corrected density forecasts are not shown as they share virtually the same values and spatial distributions as the original (uncorrected) densities presented in Figs. 4.3 and 4.4.) The lack of influence of the PV intensity bias correction on storm track behavior in the operational forecasts may be due in part to (a) the shorter forecast-observation period available, and (b) the improvements to the model after the

reforecasts were generated. Accordingly, we have opted not to correct the PV storm intensity forecasts in the analysis presented in this chapter. An advantage of omitting the PV bias correction in the forecasts is that the processing time of the bias correction approach is reduced, since only one correction is now performed (i.e., only the storm-related weather forecasts are corrected). A shorter processing time is more ideal for the rapid release of weather forecasts in operations.

4.3.2   Analysis of PV Biases in the Forecasts

Results from the analysis in Section 4.3.1 indicate that the weeks 3-4 forecasts exhibit negative biases in storm PV_{320}. We speculate that the bias may be related to errors in the mean forecast environment. This section presents other diagnostics in support of this argument.

That the CFSv2 operational forecasts exhibit a negative bias in PV at 320 K in the storm track regions relative to the operational analysis CDASv2 prompts a related question: Is this bias only apparent from a storm-focused perspective, or is it inherent to the model (i.e., its mean climate)? The results discussed in this section focus on the eastern Pacific storm track (the box 30-50°N, 180-130°W), but they are valid in the Atlantic region as well.

Consider Eq. (2.1) where $PV \equiv -g\left(\zeta_\theta + f\right)\left(\frac{\partial\theta}{\partial p}\right)$ (Hoskins et al. 1985; Holton 2004). We will examine the CDASv2 and CFSv2 mean horizontal PV_{320} and the mean vertical profiles of PV and its most relevant components: static stability $\frac{\partial\theta}{\partial p}$ and relative vorticity ζ_θ. Figure 4.6 presents average horizontal profiles of latitude versus mean PV_{320} in the Pacific region (at longitude 170°W). The weeks 3-4 operational forecasts

(CFSv2) (blue line) are shown to deviate from the CDASv2 analysis PV (red line) north of 30°N. The departure from the analysis state become larger with increasing latitude, and this behavior is observed at all longitudes. The results indicate that the PV_{320} mean climatology in CFSv2 exhibits biases consistent with those found in the PV_{320} storm intensity, suggesting that the biases are present at all times.

We next examine the vertical profiles of mean PV in the operational CFS[1] (Fig. 4.7). Figs. 4.7a-c contrast the vertical climatologies of PV, static stability, and relative vorticity respectively for 2012-2016 in the CDASv2 analysis (red curves) and the CFSv2 weeks 3-4 forecasts (blue curves). When compared to the CDASv2 analysis, the PV vertical profiles in the operational forecasts (Fig. 4.7a, blue curve) have a similar shape but exhibit clear biases. Levels above 200 hPa exhibit a positive PV bias, suggesting that stratospheric PV is overestimated in the forecasts. A negative bias is found in the 400-200 hPa layer where the mean PV_{320} surface tends to reside in the NH winter (see Fig. 2.1). The sign of the bias at these levels is consistent with that observed in the storm PV_{320} forecasts (see Fig. 4.5), suggesting that the bias in the storm track intensity reflects the internal model bias and is not an artefact of the storm tracking approach. The PV forecast profile exhibits very little bias below 400 hPa.

To explore the possible causes of the PV biases in the forecasts, we decompose the mean PV into its two main components and examine the corresponding profiles. Mean static stability and relative vorticity profiles are presented in Figs. 4.7b and 4.7c,

---

[1] To compare PV and its components in CDASv2 and CFSv2, an interpolation is needed. PV is provided on isentropic surfaces where its components are computed. The isentropic variables are then interpolated to pressure surfaces at each 6-hourly interval before computing the average at each vertical level for comparison. Missing values at levels near the surface are the result of the interpolation of near-surface isentropic levels that "intersect" the ground in pressure space.
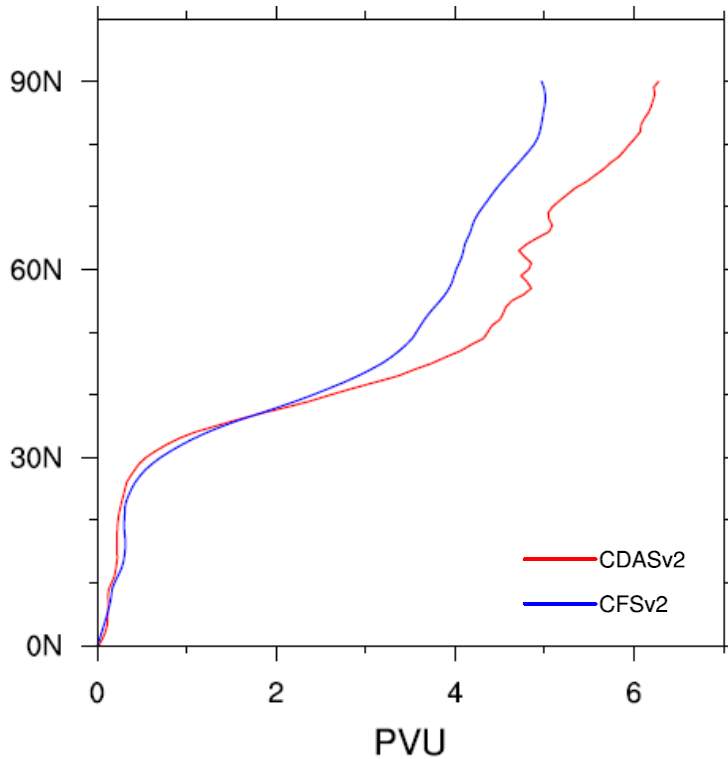
Figure 4.6: Latitude vs. PV climatology at 320 K during DJF for 2012-2016 in the Pacific region at longitude 170°W. Red colors indicate the CDASv2 operational analysis, and blue colors the CFSv2 weeks 3-4 operational forecasts. Units are PVU.

respectively. It becomes evident that the vertical shapes of the CDASv2 and CFSv2 PV profiles mostly respond to the structure of static stability (Fig. 4.7b). Moreover, at upper levels the stability forecasts exhibit biases of similar sign at the same levels as those in the mean PV forecasts (see Fig. 4.7a). As for the relative vorticity profiles (Fig. 4.7c), the analysis and forecasts share the same general shape and magnitude in the vertical, with the forecasts exhibiting a small positive bias throughout the free atmosphere (above 850 hPa). Below 850 hPa, the forecasts exhibit larger biases. The results suggest that biases in the static stability component of PV are the main drivers of the PV biases

135
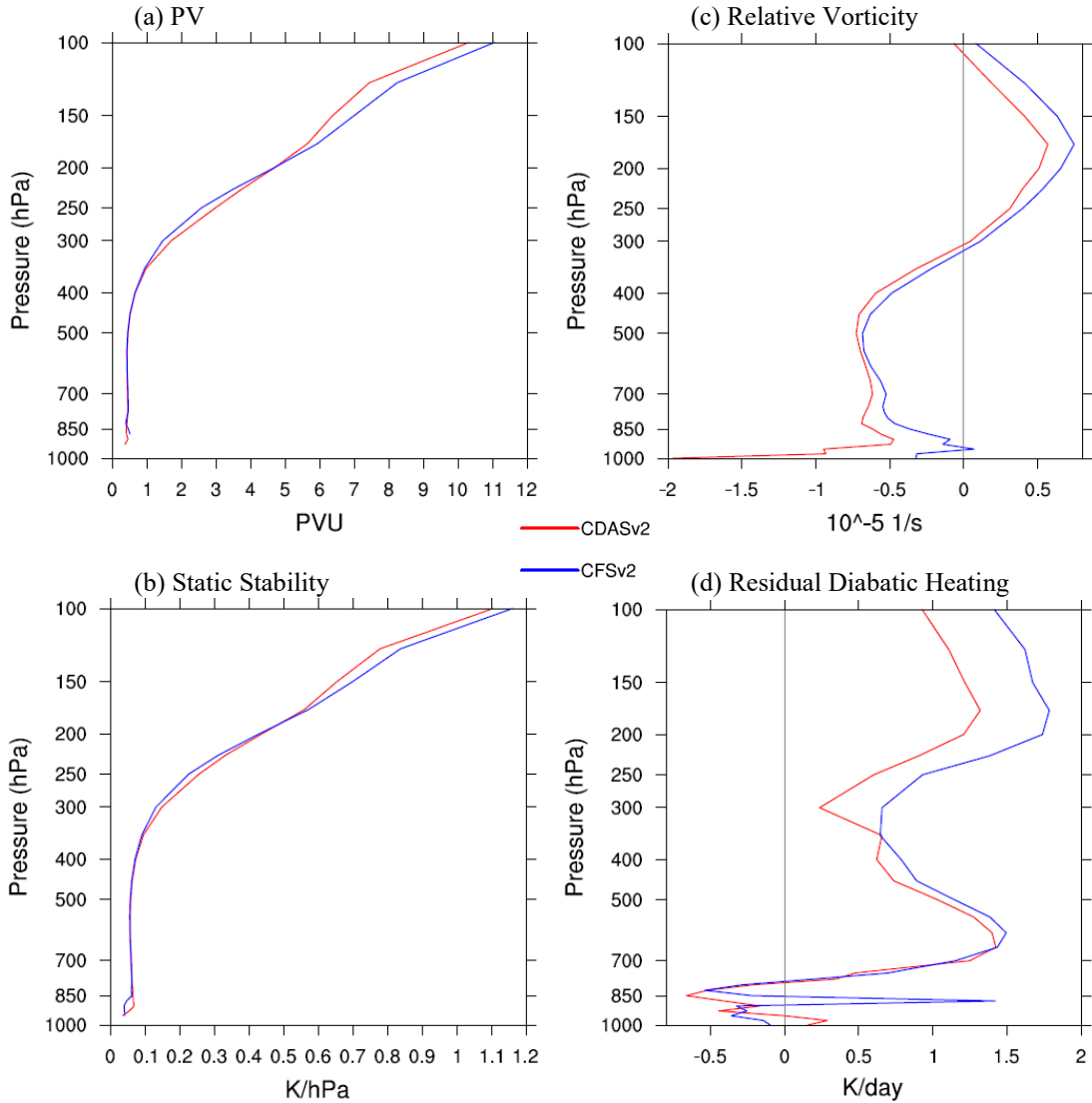
Figure 4.7: Vertical profiles of mean variables averaged for a box (30-50°N, 180-130°W) covering the eastern North Pacific Ocean during DJF for 2012-2016. (a) PV in units of PVU, (b) static stability in units of K hPa^{-1}, (c) relative vorticity in units of 10^{-5} s^{-1}, and (d) residual diabatic heating in units of K day^{-1}. Red colors indicate the CDASv2 analysis, and blue colors indicate the CFSv2 weeks 3-4 forecasts. Gray vertical lines in (c)-(d) denote a value of zero.

in the forecasts at upper levels, while at lower levels the relative vorticity and static stability biases seem to contribute in similar parts to the PV bias.

Lastly, we explore whether the biases in the PV forecasts could be related to differences in the vertical profile of diabatic heating computed as the residual in the

thermodynamic energy equation, following Eq. 2.4 (Barlow et al. 1998; Lukens et al. 2018, their Eq. 1). Fig. 4.7d shows that the 2012-2016 DJF analysis mean residual diabatic heating profile is in good agreement with previous studies (e.g., Chan and Nigam 2009). The mean forecast profile tends to have a similar shape to the operational analysis in the free atmosphere, with generally positive biases found above ~850 hPa. The larger forecast diabatic heating at upper levels may contribute in part to the reduced static stability in the forecasts, in turn, influencing the negative bias in PV at those levels. Near the surface, negative heating rates (cooling) in the forecasts are observed where heating rates are positive in the operational analysis. This could perhaps be indicative of biases in surface fluxes or the improper characterization of boundary effects in the CFSv2 operational model, which would require further study. Further attribution of the causes for the biases evident in Fig. 4.7, or their statistical significance, would require further investigation outside the scope of this work since it does not affect our conclusions.

In summary, the results show that the biases observed in the storm PV_{320} intensity forecasts are inherent in the mean PV field in the model. The negative bias in PV at upper levels seems to be dictated primarily by the static stability, while the velocity (relative vorticity) field appears to be a secondary driver. At lower levels, the PV components appear to more equally contribute to the small bias in PV. Diabatic heating errors may also contribute to the PV bias by way of reduced upper-level static stability.

Additionally, the above analysis was repeated to include CFSRR biases in order to explore whether the operational forecasts can be validated using the corresponding

reforecast data (not shown). The analysis is motivated by a recent study that found unexpected biases in the CFSv2 monthly forecast climatology relative to the reforecasts used to compute it (Tippett et al. 2018). Reforecasts are often used to diagnose the overall performance of operational forecasts (Smith and Livezey, 1999; Saha et al. 2014c; Pegion et al. 2019), and as such are assumed to accurately depict the behavior of the operational model. Thus, it has become standard practice to reduce operational forecast error by way of removing systematic errors in the reforecasts. The average PV bias in the CFS (i.e., CFSv2 and CFSRR) is dominated by the errors in CFSRR (see Fig. 3.1c), showing statistically significant positive values in the storm track regions. The CFSRR bias appears to be driven by an enhanced static stability component and weaker residual diabatic heating at upper levels that in part influences the positive bias in the reforecasts. Removal of the average bias in the CFS from the CFSv2 forecasts results in larger errors in PV that tend to degrade the forecast performance. The results suggest that when a bias correction is required, it should be done against a consistent analysis dataset (i.e., CFSv2 forecasts should be corrected against CDASv2 only, and CFSRR against CFSR only). Our analysis of storm track-related weather in Section 4.4 follows this idea.

The different heating and stability biases between CFSRR and those observed in the CFSv2 forecasts (see Fig. 4.7) may be due to upgrades to the GFS in 2015 and CFSv2 in 2011, after the reforecasts were generated (see Table 1.1). For example, relative to the reforecasts the operational forecasts may reflect different characterizations of SST gradients and surface fluxes in regions of large baroclinicity. This would require further investigation that is beyond the scope of this study.

4.4   Surface Weather Related to the Storm Tracks in the Forecasts

In this section we explore to what extent the forecasts for weeks 3-4 are able to capture the observed near-surface weather related to the storms tracks. Results presented in Section 4.3 indicated that the removal of the PV_{320} intensity bias from the operational forecasts does not noticeably improve the prediction of storm track behavior in either storm track region. As such, we evaluate the CFSv2 forecasts of storm track-related weather by associating 1000-hPa winds and surface precipitation with the PV in the original (uncorrected) weeks 3-4 forecasts.

To evaluate whether any additional improvement in the forecasts can be gained, we apply a bias correction following the methodology in Lukens and Berbery (2019) that is presented in Chapter 3. Results from Section 4.3.1 suggest that the bias correction works best if performed against a consistent analysis dataset. With this in mind, we remove the biases in the storm-related weather forecasts (relative to CDASv2) from the weather variables associated with each forecast storm identified every 6 hours. New statistics are computed using the bias-corrected forecasts.

4.4.1   Storm Track-Related Winds in the Base Period 2012-2016

We evaluate near-surface winds related to the storm tracks for the base period 2012-2016. Biases in the weeks 3-4 forecasts of storm track-related winds are depicted in Fig. 4.8. The biases are small yet significant, particularly in the eastern North Pacific Ocean and over land as well as in the western North Atlantic Ocean. The small bias values in the wind forecasts suggest that the CFSv2 is generally able to reproduce storm track-related winds at weeks 3-4 time scales.
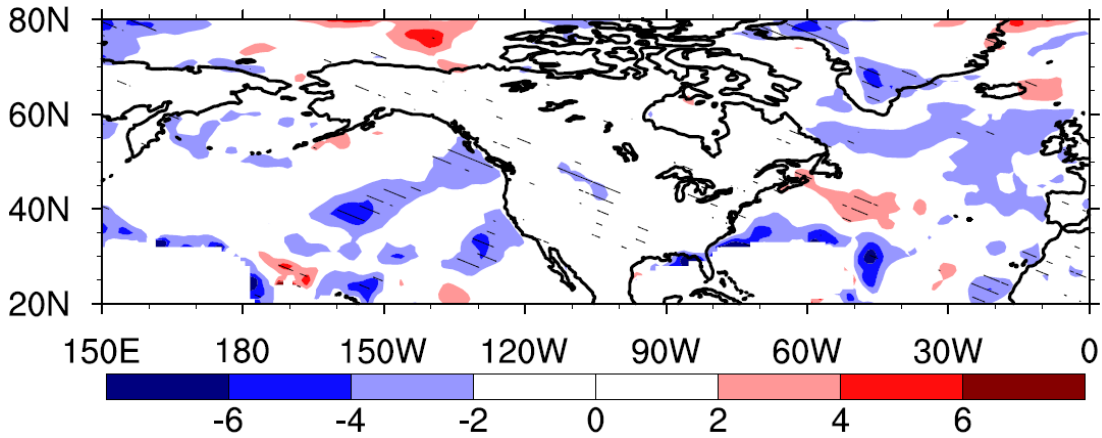
Figure 4.8: Mean bias (CFSv2 weeks 3-4 forecasts – CDASv2 analysis) in wind speed at 1000 hPa related to the storm tracks during DJF for 2012-2016. Contour interval is 2 m s^{-1}. White colors indicate values between +/- 2 m/s and masked areas with fewer than 0.5 storms per 10^6 km^2 per month.

Results from a storm track-related wind analysis for the Pacific region are presented in Fig. 4.9. In the CDASv2 analysis in the Pacific storm track region (Fig. 4.9a), the storm track-related winds are strongest over the central-eastern North Pacific Ocean. Over land, wind speed maxima are found in central North America and the northeastern US. The weeks 3-4 forecasts (Fig. 4.9b) spatially resemble the analysis winds, although the wind speeds over the eastern ocean are slightly underestimated. Removal of the average base period wind bias (see Fig. 4.8) results in the bias-corrected storm wind forecast is shown in Fig. 4.9c. The spatial distribution and intensity of the storm track-related winds in the bias-corrected forecasts correspond well with the CDASv2 analysis.

Figs. 4.9d-g statistically represent the performance of the forecasts in the Pacific region. The standard deviation of storm track-related winds in the operational analysis (Fig. 4.9d) is highest over the ocean outside of the main storm track region (i.e., where the storm track density is low; see Fig. 4.3). The RMSE of the wind forecasts (Fig.

140

4.9e, contours) exhibits similar magnitudes to the SD. The ratio of RMSE to the SD in the analysis (Fig. 4.9e, color shades) is relatively low throughout the storm track region, with values less than one found in the central Pacific where storms develop and in the lower latitudes of the eastern ocean where the SD is high. The low RSR values indicate that the forecasts already partially capture the variability in the storm track-related winds. Removal of the 2012-2016 wind bias from the forecasts yields a reduced RMSE and RSR (Fig. 4.9f), indicating improvements in the forecasts. The improvements are further highlighted by negative values in the percent change in RMSE (Fig. 4.9g). The forecast error is reduced by over 40% in the eastern North Pacific Ocean and over land. Areas where the error is shown to increase are generally found outside of the main activity storm track region and in areas where storm wind speeds are low.

Similar results are found for storm track-related winds in the Atlantic region (Fig. 4.10). Storm winds in the operational analysis (Fig. 4.10a) are strongest over the western and northeastern ocean where the storm track is more intense as well as over land east of the Rocky Mountains. Storm winds in the weeks 3-4 forecasts (Fig. 4.10b) resemble the operational analysis but show weaker wind speeds in the northeastern ocean. Removal of the 2012-2016 wind bias from the operational forecasts yields a bias-corrected storm wind forecast (Fig. 4.10c) that more closely matches the CDASv2 analysis in both magnitude and spatial distribution. The standard deviation of NAA storm winds is lowest within the main activity storm track region and larger outside of the region (Fig. 4.10d). Figs. 4.10e and 4.10f present the RSR (color shades) and RMSE (contours) of the uncorrected and bias-corrected forecasts, respectively, and the corresponding percent changes in RMSE are shown in Fig. 4.10g. The forecast storm
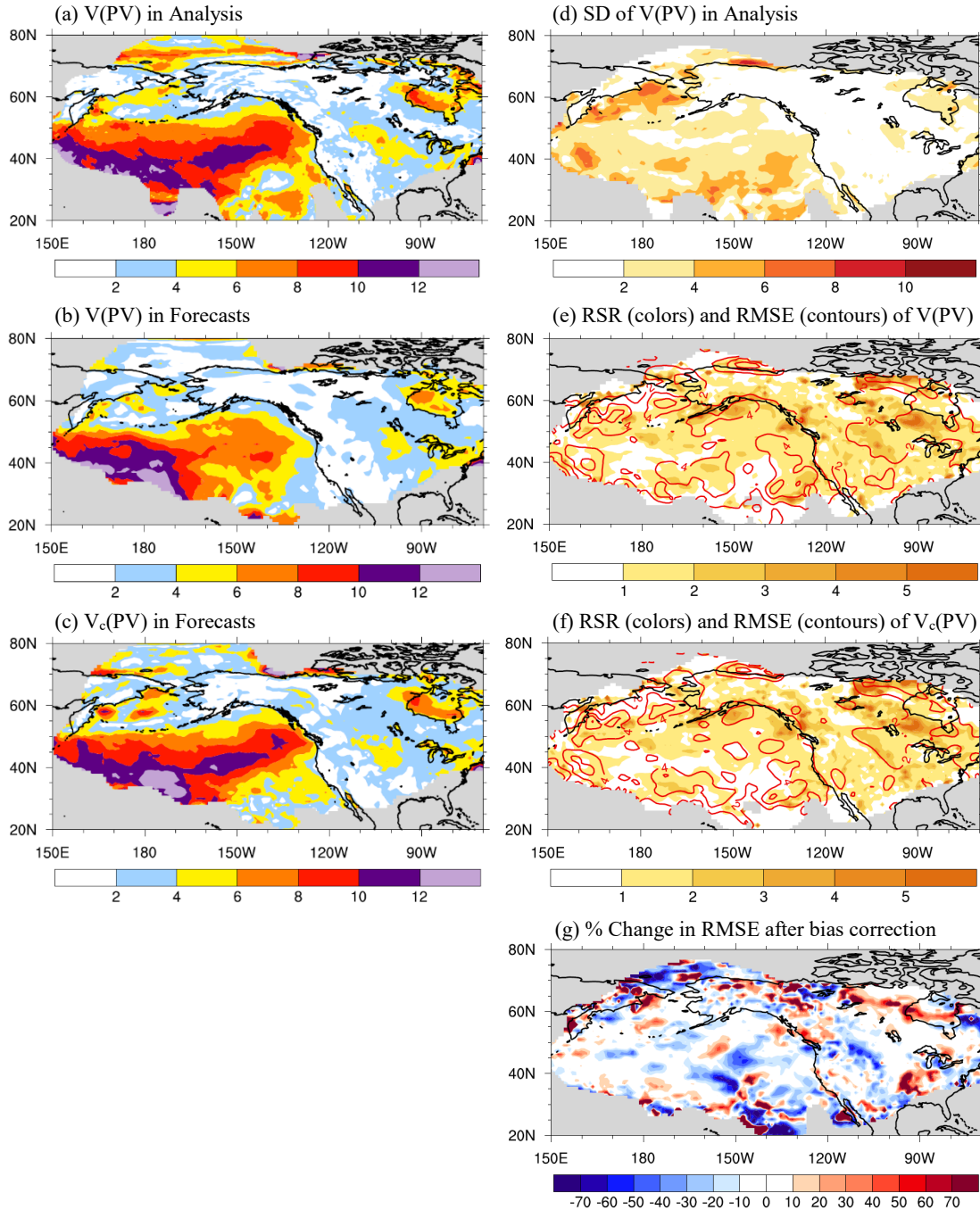
Figure 4.9: Mean wind speed on the 1000 hPa surface related to the Pacific storm track in DJF for 2012-2016: (a) CDASv2 operational analysis wind speed (V) associated with analysis potential vorticity (PV); (b) weeks 3-4 forecast wind speed associated with forecast PV; (c) bias-corrected weeks 3-4 forecast wind speed (V_c) associated with forecast PV; (d) standard deviation (SD) of analysis V(PV); (e) (colors) ratio (RSR) of RMSE of forecast V(PV) to SD of analysis V(PV) at an interval of 1, and (contours) RMSE of forecast V(PV) at an interval of 2 m s^{-1}; (f) as in (e) but for forecast V_c(PV); (g) Percent change in RMSE after forecast wind bias is removed, shown at an interval of 10%. Panels (a)-(d) are shown at an interval of 2 m s^{-1}. Gray colors mask areas with fewer than 0.5 storms per 10^6 km^2 per month.

Figure 4.10: Mean wind speed on the 1000 hPa surface related to the North American-Atlantic storm track in DJF for 2012-2016: (a) CDASv2 operational analysis wind speed (V) associated with analysis potential vorticity (PV); (b) weeks 3-4 forecast wind speed associated with forecast PV; (c) bias-corrected weeks 3-4 forecast wind speed (V_c) associated with forecast PV; (d) standard deviation (SD) of analysis V(PV); (e) (colors) ratio (RSR) of RMSE of forecast V(PV) to SD of analysis V(PV) at an interval of 1, and (contours) RMSE of forecast V(PV) at an interval of 2 m s^{-1}; (f) as in (e) but for forecast V_c(PV); (g) Percent change in RMSE after forecast wind bias is removed, shown at an interval of 10%. Panels (a)-(d) are shown at an interval of 2 m s^{-1}. Gray colors mask areas with fewer than 0.5 storms per 10^6 km^2 per month.

143

winds have lower RSR and error values where wind speeds are high, with larger errors found in areas with weaker winds (Fig. 4.10e). As is found for winds related to the Pacific storm track, the bias correction in the Atlantic region reduces the RMSE and RSR values (Fig. 4.10c), with values less than one indicating skill. The improvements are reflected in the percent change in RMSE (Fig. 4.10g) that highlights reductions in error of 30%-60% throughout the storm track region. Areas with increased error are mainly found outside of the storm track region where the track density is low (see Fig. 4.4).

The findings indicate that the CFSv2 weeks 3-4 forecasts partially encapsulate the variability in storm track-related winds in the Pacific and Atlantic regions, with bias corrections offering additional improvements over land and the oceans in areas where winter storms are most often found.

4.4.2   Storm Track-Related Winds in the Validation Period 2018

Next, we test the use of the bias correction in forecast mode. To do this, the mean base period (2012-2016) storm wind bias in the operational forecasts (see Fig. 4.8) is removed from the storm track-related winds in the validation period (2018), and the statistics are recomputed using the bias-corrected forecasts. The error in the storm wind forecasts for 2018 is measured by the mean absolute error following Eq. (4.1). The difference in MAE represents the change in error after biases are removed, with negative values indicating improvements in the bias-corrected forecasts.

Figure 4.11 presents an analysis of storm track-related winds in both the Pacific region (Figs. 4.11a-d) and the Atlantic region (Figs. 4.11e-h) for the validation period

144

Pacific Storm Track Region   **NAA Storm Track Region**

(a) V(PV) in Analysis   (e) V(PV) in Analysis

(b) V(PV) in Uncorrected Forecasts   (f) V(PV) in Uncorrected Forecasts

(c) V_c(PV) in Bias-corrected Forecasts   (g) V_c(PV) in Bias-corrected Forecasts

(d) Diff. in Wind MAE after bias correction   (h) Diff. in Wind MAE after bias correction
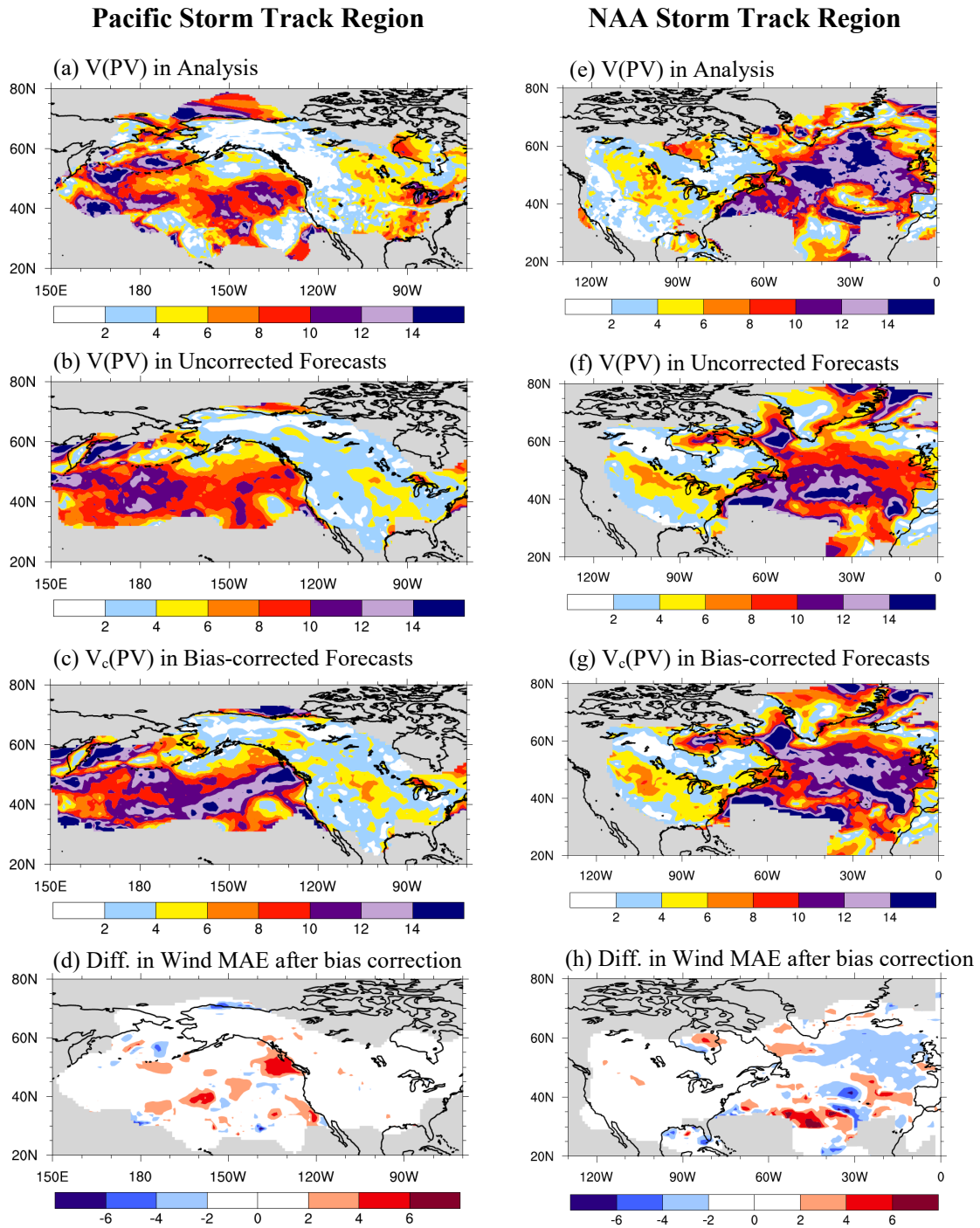
Figure 4.11: Mean wind speed on the 1000 hPa surface related to the storm tracks during DJF for 2018 in the (left column) Pacific region, and (right column) Atlantic region. (a) CDASv2 analysis wind speed (V) associated with analysis potential vorticity (PV); (b) weeks 3-4 (uncorrected) forecast wind speed associated with forecast PV; (c) bias-corrected weeks 3-4 forecast wind speed associated with forecast PV; (d) difference in MAE after the wind bias is removed. (e)-(h) as in (a)-(d) but for the NAA storm track. All panels are shown at an interval of 2 m s^{-1}. Gray colors mask areas with fewer than 0.5 storms per 10^6 km^2 per month.

145

2018. In the operational analysis in the Pacific (Fig. 4.11a), the storm track-related winds resemble those in the base period forecasts (see Fig. 4.9a). Intense winds are found over the ocean where the storm track is strongest as well as over eastern North America. The weeks 3-4 forecasts (Fig. 4.11b) are similar to the analysis in spatial distribution and magnitude, in particular in the eastern North Pacific region. Removal of the base period wind bias from the validation period forecasts results in an overestimation of Pacific storm winds over the ocean and little change over land (Fig. 4.11c). Positive values in the difference in MAE (Fig. 4.11d) emphasize that the bias correction offers little to no improvement in the Pacific storm track forecasts.

In the Atlantic sector, the CDASv2 analysis (Fig. 4.11e) and weeks 3-4 forecasts (Fig. 4.11f) are similar over land and the western North Atlantic Ocean. The bias-corrected wind forecasts for 2018 (Fig. 4.11g) are closer to the analysis in the northeastern part of the basin where the MAE is shown to decrease (Fig. 4.11h). This suggests that the bias correction offers additional minor improvements in the exit region of the NAA storm track over the ocean but little impact over land. Areas with increased MAE in the Atlantic are found outside of the main storm track region.

In general, the results indicate that the weeks 3-4 forecasts are capable of reproducing the spatial distributions and magnitudes of near-surface storm winds in both the Pacific and NAA storm track regions for a single winter season. Bias corrections are found to provide additional minor improvements in the wind forecasts in the Atlantic sector only, while they offer no additional improvement in the Pacific.

4.4.3   Storm Track-Related Precipitation in the Forecasts

In this section, the performance of the weeks 3-4 forecasts of storm track-related precipitation is evaluated. The CPC gauge-based daily precipitation analysis is considered truth and is used for comparison (see Section 3.1 for more details about the data). Daily precipitation is associated with the original (uncorrected) PV in the storm track forecasts. Bias corrections are applied to evaluate whether any additional improvements can be gained.

Precipitation related to the Pacific storm track in the contiguous United States is shown in Fig. 4.12. (Results for the NAA storm track are similar and thus are not shown.) In the CPC daily analysis (Fig. 4.12a), precipitation related to the Pacific storm track is highest in the northwestern and southeastern US where the corresponding standard deviation is large (Fig. 4.12e). The weeks 3-4 forecasts (Fig. 4.12b) show higher precipitation rates as well as higher RMSE values (Fig. 4.12f, contours) relative to the CPC analysis. The corresponding ratio RSR of RMSE to the SD of the CPC analysis (Fig. 4.12f, color shades) is low where precipitation rates are high. Similarly, the RMSE of storm precipitation in the forecasts is low in regions where precipitation rates are low and corresponding RSR values are high (Fig. 4.12f). Statistically significant positive biases are found in precipitation related to all winter storms in CFSv2 for 2012-2016, with maxima found near the west coast and in the east (Fig. 4.12d). Removal of the base period precipitation bias yields reduced precipitation intensities (Fig. 4.12c) that better correspond with the CPC gauge analysis. This is evident in the reduced RMSE and RSR values throughout CONUS (Fig. 4.12g). The

(a) PR(PV) in CPC Gauge Analysis

(e) SD of PR(PV) in CPC Gauge Analysis

(b) PR(PV) in Forecasts

(f) RSR (colors) and RMSE (contours) of PR(PV)

(c) PR$_c$(PV) in Forecasts

(g) RSR (colors) and RMSE (contours) of PR$_c$(PV)

(d) Bias in PR

(h) % Change in RMSE

148
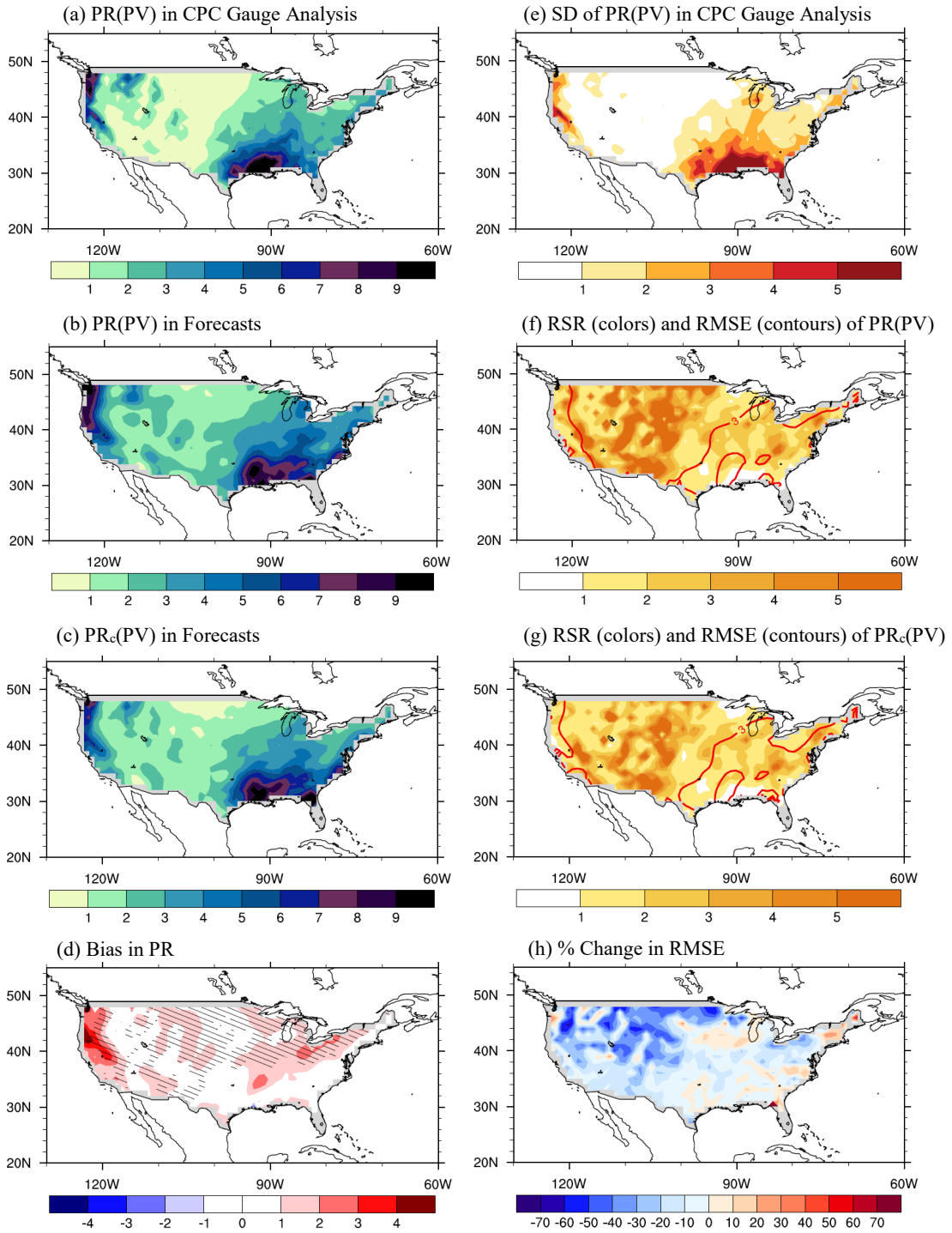
Figure 4.12: Mean precipitation related to the Pacific storm track in DJF for 2012-2016. Left column: (a) CPC gauge-based daily analysis precipitation rates (PR) associated with CDASv2 analysis potential vorticity (PV); (b) weeks 3-4 forecast PR associated with forecast PV; (c) bias-corrected weeks 3-4 forecast PR (PR_c) associated with forecast PV_c; (d) mean bias in forecast PR related to all storms, where hatched regions indicate statistical significance ($p < 0.05$). Right column: (e) Standard deviation (SD) of CPC gauge-based analysis PR(PV); (f) (colors) ratio (RSR) of RMSE of forecast PR(PV) to SD of analysis PR(PV) at an interval of 1, and (contours) RMSE of forecast PR(PV) at an interval of 1 mm day^{-1}; (f) bias-corrected forecast PR (PR_c) associated with PV; (g) as in (f) but for forecast PR_c(PV); (h) percent change in RMSE after forecast bias is removed shown at an interval of 10%. Panels (a)-(e) are shown at an interval of 1 mm day^{-1}. Gray colors in CONUS indicate missing values.

largest reductions in error as depicted by the percent change in RMSE (Fig. 4.12h) are found in regions where precipitation rates are relatively low.

Overall, the findings suggest that the CFSv2 weeks 3-4 forecasts can generally reproduce more extreme storm track-related precipitation observations without the need of a bias correction. Further, the forecasts better capture the observed variability in more extreme storm track-related precipitation relative to lower precipitation rates.

Finally, we test whether the bias correction approach has an impact on the validation period forecasts of storm track-related precipitation (not shown). It is found that the 2018 forecasts exhibit a negative bias in storm track-related precipitation that opposes the positive biases found in the base period forecasts. As such, the removal of base period precipitation biases yields no noticeable improvement in the validation period forecasts. This is particularly evident in regions that experience more extreme precipitation rates. In general, the results imply that the approach is more useful for long-term assessments of storm track-related precipitation and not as much for a single winter season.

4.5   *Summary and Conclusions*

The work presented in this chapter explored the use of storm track statistics for the advancement of subseasonal-to-seasonal prediction in operations. Specifically, storm tracks and related weather in North America were examined in the CFS operational forecasts at the weeks 3-4 lead time. Bias corrections were performed in order to evaluate whether additional information could be obtained from the weeks 3-4 operational forecasts.

The analysis focused on storm tracks in the 2012-2016 CFSv2 forecasts and corresponding CDASv2 operational analysis. The forecast performance was evaluated separately for the Pacific and North American-Atlantic storm tracks, as they have a significant impact on winter weather in North America. Statistics characterizing storm track behavior were analyzed using all identified storms that develop in each storm track region. It was found that the CFSv2 forecasts are able to reproduce the general behavior of the storm tracks (genesis, lysis, and track density) as well as the observed latitudinal distributions of winter storms in each storm track region.

Statistically significant negative biases were found in the PV_{320} storm intensity forecasts, which differ considerably from those found in CFSRR. We found that the biases are not limited to storm periods but are present in the model's mean climate. At all longitudes, PV_{320} in the CFSv2 forecasts exhibit weaker PV values north of 30°N relative to the CDASv2 analysis. An examination of the mean vertical profiles of PV and its components in the weeks 3-4 forecasts indicates that the PV biases are influenced by changes in the model climate, which suggests that care should be taken when assessing the PV forecast skill using the reforecast data. Specifically, the PV

biases are primarily driven by the static stability component, while the velocity (relative vorticity) component appears to be a secondary driver. At lower levels, the two components seem to contribute more equally to the PV bias.

The relation of storm tracks to surface weather variables was examined and the effect of bias corrections on the forecasts was explored. Near-surface winds and surface precipitation related to the storm tracks in the forecasts resemble those in the operational analysis. Small yet significant wind biases were found over the oceans and in eastern North America, and significant positive precipitation biases were found throughout CONUS. The removal of forecast biases yields reductions in wind error of over 40% in each storm track region. For precipitation, the bias correction reduces the error in regions with lower precipitation rates, and offers little additional improvement in regions that experience more intense storm precipitation in CONUS. In forecast mode, the storm track-related weather forecasts are found to correspond well with the CDASv2 analysis without the need for bias corrections. Bias corrections yield additional minor improvements in the northeast North Atlantic Ocean only, with little improvement observed elsewhere.

The findings of this study indicate that the CFSv2 weeks 3-4 forecasts do contain useful storm track-related information for S2S prediction in operations. We have found that the forecasts reproduce well the winter storm track patterns and smaller scale regions of cyclogenesis and cyclolysis, as well as the storm track-related near-surface winds and precipitation. Bias corrections offer additional minor improvements in storm track-related weather and storm PV intensity. Further, the findings suggest that if bias corrections are required, they should be done against a consistent analysis

151

dataset (i.e., operational forecasts corrected against the operational analysis). The reason is that statistics and biases are model-version dependent and are affected by updates to the model.

Chapter 5: Concluding Remarks and Future Directions

## *5.1*	*Concluding Remarks*

In this thesis we investigated the contribution of storm track-related information to the understanding and advancement of subseasonal-to-seasonal weather prediction in North America. S2S forecasts have the potential to benefit multiple sectors in the global community from the extension of lead times for severe weather warnings to the optimization of responses to weather-related resource fluctuations and subsequent effects on global economy. However, S2S prediction is still a largely unresolved scientific problem, and this has initiated a recent international effort to improve S2S forecasting in operations. Storm tracks have the potential to advance S2S prediction by supplementing existing severe weather outlooks with additional actionable information at longer lead times that may not be provided by forecasts of standard variables. These factors emphasize the need for S2S forecast development from a storm-focused perspective and motivate the research presented here. Winter weather related to the storm tracks in the Pacific and Atlantic regions is investigated using global reanalysis, retrospective forecast (reforecast), and operational forecast data in the NCEP Climate Forecast System for a single forecast period (weeks 3-4). We focus on the weeks 3-4 period because it falls within the S2S forecast range and represents the gap in predictability. Further, weeks 3-4 forecasts are routinely issued in operations by the CPC.

The results of this work further our understanding of winter storm track behavior and the impact on surface weather and extremes in North America. Storms

were identified as isentropic potential vorticity anomalies on the 320-K surface and were objectively tracked in a Lagrangian framework throughout their evolution. Two types of storm tracks were examined: the *all-storm tracks* that are shaped by all winter storms that pass the storm identification criteria, and the *strong-storm tracks* that are defined by the more intense storms in terms of PV. Strong-storm tracks were found to leave a significant imprint on winter weather potentially leading to structural and economic loss in North America, despite making up a small fraction (16%) of all storms that develop. This imprint depends on dynamical features as well as the local population density that is used to estimate storm loss. We employ the use of a storm loss metric (Klawa and Ulbrich 2003) to highlight regions that are most vulnerable to damages from storm-related high impact winds. The metric is unique in that it considers that damages are more likely to occur in regions that are more densely populated, as it accounts for both extreme wind speeds and local population. Thus, we found that while more intense strong-storm winds are found in central North America, the eastern US and North American coasts are most vulnerable to storm track-related loss in winter.

That strong-storm tracks have a significant imprint on winter weather in North America motivated the next portion of this work. We investigated whether the CFS reforecasts are able to reproduce the observed impact of storm tracks at the weeks 3-4 lead time. As a conceptual analysis for operational applications, we examined the storm tracks in the reforecasts for two periods (base, 1983-2002; validation, 2003-2010) to assess their use in advancing S2S prediction in a more realistic forecast mode. It was found that the weeks 3-4 reforecasts do contain useful storm track-related information supporting the potential use of storm track statistics in the advancement of S2S

prediction of hazardous weather in North America. Statistically significant biases were found in the reforecasts of PV storm intensity, and their removal improved general features of the storm tracks, corresponding well with those in the reanalysis and in previous studies. Further, CFSRR reproduces well the observed intensity and spatial distributions of storm track-related near-surface winds (those at 1000 hPa), with small yet significant biases found in the storm track regions. The bias correction of storm track-related weather has a positive impact on precipitation and a minor positive impact on storm winds at 1000 hPa. The bias-corrected fields better depict the observed variability and exhibit additional improvements in the representation of winter weather associated with strong-storm tracks. Further, the reforecasts reproduce the characteristic intensity and frequency of hazardous strong-storm winds. One note of caution is that the signal in precipitation is better captured by the all-storm tracks but not as well by the strong-storm tracks, suggesting further analysis will be needed.

Additionally, we examine the CFSRR winds at 1000 hPa as a proxy of the near-surface winds in place of those on the hybrid level 1 surface (H1) as was done in Chapter 2. The reason is that CFSRR exhibits large deviations from the winds at 1000 hPa. Nothing is lost in the use of 1000-hPa winds, as they are mostly valid except over regions of high topography. Further, results from H1 wind bias corrections suggest that the H1 winds contain useful information at S2S time scales after biases are removed.

The CFSv2 weeks 3-4 operational forecasts were found to retain their ability to predict winter storm tracks as observed in the reanalysis and reforecasts, indicating that CFSv2 is generally able to characterize the evolution of winter storms in North America. Moreover, the operational forecasts are able to reproduce the observed

proportions of storms per latitude in both the Pacific and Atlantic regions. As for storm PV_{320} intensity, the operational forecasts were found to exhibit statistically significant negative biases that differ considerably from those in CFSRR. The PV biases are apparently related to changes in the model climate, which suggests that care should be taken when assessing the performance of PV forecasts using the retrospective forecast data. Specifically, the PV and its biases in the model seem to be dominated by the static stability component, with the relative vorticity component acting as a secondary driver.

As for storm track-related weather, the weeks 3-4 operational forecasts were found to already partially capture the observed variability in near-surface winds in the Pacific and Atlantic regions, while they show significant positive biases in precipitation in CONUS. Bias corrections further improve the wind forecasts over the oceans and eastern North America, and in the precipitation forecasts over CONUS in regions that experience lower precipitation rates. In forecast mode, the bias corrections yield minor improvements in the Atlantic sector and not as well in the Pacific. Our results are promising for the advancement of S2S prediction of storm-related weather, although regions where the ratio of error to standard deviation is greater than 1 suggest that the forecast skill could still be improved.

The analysis presented in this thesis was primarily conducted using the National Center for Atmospheric Research (NCAR) Command Language (NCL). The storm track bias correction was specifically developed for the analysis and is a major contribution of this work. It is a simple method and takes little time to process, and this is advantageous for the rapid release of severe weather forecasts. Fig. 5.1 presents a schematic of the bias correction procedure. The uncorrected (original) weather

156

variables are related to the uncorrected PV in the storm tracks (Fig. 5.1a). After the bias in PV is removed, the uncorrected weather variables are associated with the bias-corrected PV (Fig. 5.1b). Lastly, the biases in the weather variables are removed, and the bias-corrected weather is related to the bias-corrected PV in the storm tracks (Fig. 5.1c). Further, the findings suggested that bias corrections should be applied using consistent analysis datasets (i.e., operational analysis for operational forecasts, and reanalysis for reforecasts), as the biases are influenced by updates to the model and thus are model-version dependent.

Overall, the research presented in this thesis provides a unique storm-focused perspective in the NCEP Climate Forecast System and contributes to the understanding of the potential use of storm track diagnostics in the advancement of subseasonal-to-seasonal prediction. The main contribution of this work is that it demonstrates that the use of climatological storm track statistics described by PV anomalies coupled with an appropriate storm track bias correction is a powerful instrument for the advancement of S2S prediction. The findings offer additional insight into the impact of storm tracks on severe weather in North America. Further, the CFS weeks 3-4 forecasts are found to contain useful storm track-related information at subseasonal-to-seasonal time scales that could supplement existing severe weather outlooks and advance emergency management practices across multiple sectors. Therefore, our findings support that storm track characterization is valuable for operational S2S prediction, which is advantageous for future applications in different prediction systems, including multi-model ensembles.
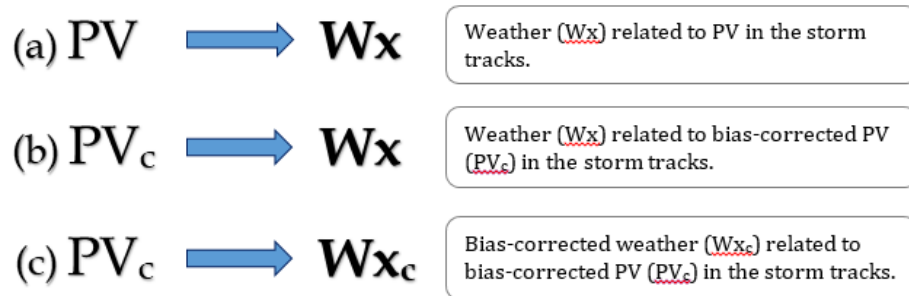
Figure 5.1: Schematic of bias correction method used in this work. (a) Uncorrected PV related to uncorrected weather (Wx) variables, (b) bias-corrected PV (PV$_c$) related to uncorrected Wx, and (c) PV$_c$ related to bias-corrected weather (Wx$_c$). The bubbles of text on the right correspond to each row.

5.2   Future Directions

We want to explore the implementation of storm track diagnostics in operational ensemble forecasts for North America in a future study. In recent years, operational forecast systems have been transitioning to a multi-model ensemble approach, as studies have shown that multi-model ensembles produce more skillful forecasts at longer lead times than any individual model (e.g., Hagedorn et al. 2005; Tebaldi and Knutti 2007). The need for ensemble forecasts was nationally recognized in a 2010 consensus report by the National Research Council that called for innovative advancements in intraseasonal to interannual prediction in order to better inform decision makers on the state of the current climate and the impacts of climate change (National Research Council 2010). As a result, multi-model ensemble experiments have since been the focus of US and international agencies for the advancement of subseasonal-to-seasonal prediction. We intend to apply our approach to different operational model forecasts in an ensemble mode, like the system known as the North

American Multi-Model Ensemble (NMME; Kirtman et al. 2014), or the recently established Subseasonal Experiment (SubX; Pegion et al. 2019), a multi-model subseasonal experiment. Both the NMME and SubX multi-model ensembles have been found to produce more skillful, better-quality seasonal and subseasonal forecasts, respectively, than any single member. We expect that our approach in an ensemble forecast system would further improve the quality of the weeks 3-4 forecasts of storm tracks and related weather, generating more robust results.

Another potential future direction would be to further explore the PV differences found in the CFS model climate, and investigate whether such differences are found in other forecast systems. In Chapter 4 we concluded that the opposing biases in PV in the CFS reforecasts and operational forecasts were largely attributed to differences in the static stability component of PV, but as of yet we do not know why these differences exist. In a future study, we would like to further understand the reasons for the opposing model climates of CFSRR and CFSv2. It is important to understand why inconsistencies in model climates exist between operational forecasts and the reforecasts used to verify them, as such inconsistencies could lead to unreliable skill assessments that affect future applications of the model. We speculate that updates to the NCEP Global Forecast System (GFS) after the generation of the CFS reforecast dataset (see Table 1.1) may in part contribute to the changes observed in the vertical stability forecasts. Diagnostics including experimental runs with and without the model updates should help clarify the impact on the model climate.

Two additional potential avenues of research include exploring (1) the use of a time-varying bias correction in improving S2S storm track prediction, and (2) the

impact of storm tracks on atmospheric river prediction. The removal of a static bias operates under the assumption that the model bias does not change over time, and this may misrepresent the results if the bias is found to vary with time. We would like to investigate whether the storm track and related weather biases change with time, and if so whether the removal of such biases can further improve storm track prediction at S2S scales, producing more robust results.

Atmospheric rivers are regions of strong water vapor transport outside of the tropics that, along with strong low-level winds, have been associated with flooding in the US (Newell et al. 1992; Rutz et al. 2014). Recently, winter storms have been found to contribute to the structure of atmospheric rivers by exporting water vapor into narrow filaments behind the storms as they travel poleward (Dacre et al. 2015). We would also like to explore how the prediction of winter storm track behavior may influence the prediction of atmospheric rivers and related impacts, which may help to enhance forecasts of extreme flooding.

Lastly, we would like to investigate how the bias correction might result in the avoidance of damages from storm-related high impact weather. The vulnerability of offshore platforms and highly populated areas on land can be quantified into expected monetary loss following Klawa and Ulbrich (2003). Expected loss is defined as the loss index multiplied by a regression coefficient that represents the factor between the loss index time series and the time series of detrended actual loss estimates in dollar amounts obtained from, e.g., life and property insurance data. Forecasts of expected loss associated with the storm tracks can then be validated against the actual loss or true damage estimates to determine the skill of the loss forecasts. We speculate that the

bias correction would improve the S2S prediction of high impact storm winds and related damages, particularly in an ensemble mode, and this could help inform decisions regarding emergency preparedness and response protocols.

Bibliography

Adler, R. F., G. Gu, and G. J. Huffman, 2012: Estimating Climatological Bias Errors for the Global Precipitation Climatology Project (GPCP). *J. Appl. Meteor. Climatol.,* **51,** 84-99, doi: 10.1175/JAMC-D-11-052.1.

Adler, R.F., G.J. Huffman, A. Chang, R. Ferraro, P. Xie, J. Janowiak, B. Rudolf, U. Schneider, S. Curtis, D. Bolvin, A. Gruber, J. Susskind, P. Arkin, E. Nelkin 2003: The Version 2 Global Precipitation Climatology Project (GPCP) Monthly Precipitation Analysis (1979-Present). *J. Hydrometeor.*, **4**, 1147-1167.

Baldwin, M. P., and T. J. Dunkerton, 2001: Stratospheric harbingers of anomalous weather regimes. *Science*, **294,** 581-584, doi: 10.1126/science.1063315.

Baldwin, M. P., D. B. Stephenson, D. W. J. Thompson, T. J. Dunkerton, A. D. Charlton, and A. O'Neill, 2003: Stratospheric memory and skill of extended-range weather forecasts. *Science*, **301,** 636-640.

Barlow, M., S. Nigam, and E. H. Berbery 1998: Evolution of the North American Monsoon System. *J. Climate,* **11**, 2238-2257.

Bell, R. J., S. L. Gray, and O. P. Jones, 2017: North Atlantic storm driving of extreme wave heights in the North Sea. *J. Geophys. Res. Oceans,* **122,** 3253-3268, doi: 10.1002/2016JC012501.

Bengtsson, L., S. Hagermann, and K. I. Hodges, 2004: Can climate trends be calculated from reanalysis data? *J. Geophys. Res.,* **109,** D11111, doi: 10.1029/2004JD004536.

Berbery, E. H., and C. S. Vera, 1996: Characteristics of the Southern Hemisphere winter storm track with filtered and unfiltered data. *J. Atmos. Sci.*, **53**, 468-481.

Blackmon, M. L., J. M. Wallace, N.-C. Lau, and S. L. Mullen, 1977: An observational study of the Northern Hemisphere wintertime circulation. *J. Atmos. Sci.,* **34,** 1040-1053.

Bolvin, D. T., R. F. Adler, G. J. Huffman, E. J. Nelkin, and J. P. Poutiainen, 2009: Comparison of GPCP Monthly and Daily Precipitation Estimates with High-Latitude Gauge Observations. *J. Applied Meteor. Clim.,* **48,** 1843-1857, doi: 10.1175/2009JAMC2147.1.

Booth, J. F., C. M. Naud, and J. Willison, 2018: Evaluation of extratropical cyclone precipitation in the North Atlantic basin: an analysis of ERA-Interim, WRF, and two CMIP5 models. *J. Climate,* **31,** 2345-2360, doi: 10.1175/JCLI-D-17-0308.1.

Booth, J. F., H. E. Rieder, D. E. Lee, and Y. Kushnir, 2015: The paths of extratropical cyclones associated with wintertime high-wind events in the northeastern United States. *J. Appl. Meteorol. Climatol.,* **54,** 1871–1885, doi: 10.1175/JAMC-D-14-0320.1.

Brayshaw, D. J., B. Hoskins, and M. Blackburn, 2008: The storm-track response to idealized SST perturbations in an aquaplanet GCM. *J. Atmos. Sci.*, **65**, 2842-2860.

Brayshaw, D. J., B. Hoskins, and M. Blackburn, 2009: The basic ingredients of the North Atlantic storm track. Part I: Land-sea contrast and orography. *J. Atmos. Sci.,* **66,** 2539-2558, doi: 10.1175/2009JAS3078.1.

Brown, Jr., J. A., 1964: A diagnostic study of tropospheric diabatic heating and the generation of available potential energy. Tellus, 16:3, 371-388, doi: 10.3402/tellusa.v16i3.8931.

Brunet, G., and Coauthors, 2010: Collaboration of the weather and climate communities to advance subseasonal to seasonal prediction. *Bull. Amer. Meteor. Soc.,* **91,** 1397–1406.

Catto, J. L., C. Jakob, G. Berry, and N. Nicholls, 2012: Relating global precipitation to atmospheric fronts. *Geophys. Res. Lett.,* **39,** L10805, doi: 10.1029/2012GL051736.

Chan, S. C., and S. Nigam, 2009: Residual diagnosis of diabatic heating from ERA-40 and NCEP reanalyses: Intercomparisons with TRMM. *J. Climate,* **22,** 414-428, doi: 10.1175/2008JCLI2417.1.

Chang, E. K. M., 2001: GCM and observational diagnoses of the seasonal and interannual variations of the Pacific storm track during the cool season. *J. Atmos. Sci.,* **58,** 1784-1800.

Chang, E. K. M., 2009: Diabatic and orographic forcing of northern winter stationary waves and storm tracks. *J. Climate,* **22,** 670-688, doi: 10.1175/2008JCLI2403.1.

Chang, E. K. M., and Y. Fu, 2002: Interdecadal variations in Northern Hemisphere winter storm track intensity. *J. Climate,* **15**, 642-658.

Chang, E. K. M., and Y. Fu, 2003: Using mean flow change as a proxy to infer interdecadal storm track variability. *J. Climate,* **16,** 2178-2196.

Chang, E. K. M., and I. Orlanski, 1993: On the dynamics of a storm track. *J. Atmos. Sci.*, **50**, 2038-2053.

Chang, E. K. M., S. Lee, and K. L. Swanson, 2002: Storm track dynamics. *J. Climate,* **15,** 2163-2183.

Chelliah, M., W. Ebisuzaki, S. Weaver, and A. Kumar, 2011: Evaluating the tropospheric variability in National Centers for Environmental Prediction's climate forecast system reanalysis. *J. Geophys. Res.*, **116**, D17107.

Chen, M., W. Shi, P. Xie, V. B. S. Silva, V. E. Kousky, R. W. Higgins, and J. E. Janowiak, 2008: Assessing objective techniques for gauge-based analyses of global daily precipitation. *J. Geophys. Res.,* **113,** D04110.

Colucci, S. J., 1976: Winter cyclone frequencies over the eastern United States and adjacent western Atlantic. *Bull. Amer, Meteor. Soc,* **57(5),** 548-553.

Dacre, H. F., P. A. Clark, O. Martinez-Alvarado, M. A. Stringer, and D. A. Lavers, 2015: How do atmospheric rivers form? *Bull. Amer, Meteor. Soc,* **96,** 1243-1255, doi: 10.1175/BAMS-D-14-00031.1.

Davis, R. E., and R. Dolan, 1993: Nor'easters. *American Scientist,* **81,** 428-439.

Dobson, J. E., E. A. Bright, P. R. Coleman, R. C. Durfee, B. A. Worley, 2000: A Global Population database for Estimating Populations at Risk. *Photogrammetric Engineering & Remote Sensing,* **66**, 849-857.

Donat, M. G., G. C. Leckebusch, S. Wild, and U. Ulbrich, 2011: Future changes in European winter storm losses and extreme wind speeds inferred from GCM and RCM multi-model simulations. *Nat. Hazards Earth Syst. Sci.*, **11**, 1351-1370, https://doi.org/10.5194/nhess-11-1351-2011.

Field, P. R., and R. Wood, 2007: Precipitation and cloud structure in midlatitude cyclones. *J. Climate,* **20,** 233-254, doi: 10.1175/JCLI3998.1.

Garreaud, R., 2007: Precipitation and circulation covariability in the extratropics. *J. Climate,* **20,** 4789-4797, doi: 10.1175/JCLI4257.1.

Geller, M. A., and S. K. Avery, 1978: Northern Hemisphere distributions of diabatic heating in the troposphere derived from general circulation data. *Mon. Wea. Rev.,* **106,** 629-636.

Grise, K. M., S.-W. Son, and J. R. Gyakum, 2013: Intraseasonal and interannual variability in North American storm tracks and its relationship to equatorial Pacific variability. *Mon. Wea. Rev.*, **141**, 3610-3625, doi: 10.1175/MWR-D-12-00322.1.

Gulev, S. K., O. Zolina, and S. Grigoriev, 2001: Extratropical cyclone variability in the Northern Hemisphere winter from the NCEP/NCAR reanalysis data. *Clim. Dyn.*, **17,** 795-809.

Guo, Y., T. Shinoda, J. Lin, and E. K. M. Chang, 2017: Variations of Northern Hemisphere storm track and extratropical cyclone activity associated with the Madden-Julian oscillation. *J. Climate*, **30,** 4799-4818, doi: 10.1175/JCLI-D-16-0513.1.

Hagedorn, R., F. J. Doblas-Reyes, and T. N. Palmer, 2005: The rationale behind the success of multi-model ensembles in seasonal forecasting – I. Basic concept. *Tellus,* **57a,** 219-233.

Hawcroft, M. K., L. C. Shaffrey, K. I. Hodges, and H. F. Dacre, 2012: How much Northern Hemisphere precipitation is associated with extratropical cyclones? *Geophys. Res. Lett.,* **39**, L24809.

Hawcroft, M. K., L. C. Shaffrey, K. I., Hodges, and H. F. Dacre, 2015: Can climate models represent the precipitation associated with extratropical cyclones? *Clim. Dyn.*, 1-17, doi: 10.1007/s00382-015-2863-z.

Held, I. M., 1993: Large-Scale Dynamics and Global Warming. *Bull. Amer. Meteor. Soc.,* **74,** 228-241.

Hodges, K. I., 1994: A general method for tracking analysis and its application to meteorological data. *Mon. Wea. Rev.,* **122**, 2573-2586.

Hodges, K. I., 1995: Feature tracking on the unit sphere. *Mon. Wea. Rev.,* **123**, 3458-3465.

Hodges, K. I., 1996: Spherical Nonparametric Estimators Applied to the UGAMP Model Integration for AMIP. *Mon. Wea. Rev.,* **124,** 2914-2932.

Hodges, K. I., 1999: Adaptive constraints for feature tracking. *Mon. Wea. Rev.,* **127,** 1362-1373.

Hodges, K. I., 2008: Confidence Intervals and Significance Tests for Spherical Data Derived from Feature Tracking. *Mon. Wea. Rev.,* **136,** 1758-1777, doi: 10.1175/2007MWR2299.1.

Holman, B. P., S. M. Lazarus, and M. E. Splitt, 2017: A fetch-based statistical method to bias correct and downscale wind speed over unresolved water bodies. *Wea. Forecasting,* **32,** 1637-1657, doi: 10.1175/WAF-D-17-0016.1.

Holton, J. R., 2004: An introduction to dynamic meteorology, 4th edition. *Intl Geophys. Series,* **88.**

Hoskins, B. J., 1997: A potential vorticity view of synoptic development. *Meteorol. Appl.,* **4,** 325-334.

Hoskins, B. J., 2015: Potential vorticity and the PV perspective. *Adv. Atmos. Sci.,* **32,** 2–9, doi:10.1007/s00376-014-0007-8.

Hoskins, B. J., and K. I. Hodges, 2002: New perspectives on the Northern Hemisphere winter storm tracks. *J. Atmos. Sci.*, **59**, 1041-1061.

Hoskins, B. J., and P. J. Valdes, 1990: On the existence of storm-tracks. *J. Atmos. Sci.*, **47**, 1854-1864.

Hoskins, B. J., M. E. McIntyre, and A. W. Robertson, 1985: On the use and significance of isentropic potential vorticity maps. *Quart. J. Roy. Meteor. Soc.,* **111,** 877-946.

Hoskins, B. J., H. H. Hsu, I. N. James, M. Masutani, P. D. Sardeshmukh, and G. H. White, 1989: Diagnostics of the global atmospheric circulation based on ECMWF analyses 1979–1989. WMO/TD-No. 326, World Meteorological Organization, 217 pp.

Hotta, D., and H. Nakamura, 2011: On the significance of the sensible heat supply from the ocean in the maintenance of the mean baroclinicity along storm tracks. *J. Climate,* **24,** 3377-3401, doi: 10.1175/2010JCLI3910.1.

Huffman, G. J., D. T. Bolvin, and R. F. Adler, 2012: GPCP Version 1.2 1-Degree Daily (1DD) Precipitation Data Set. WDC-A, NCDC, accessed 3 June 2015,

https://www.ncdc.noaa.gov/wdcmet/data-access-search-viewer-tools/global-precipitation-climatologyproject-gpcp-clearinghouse.

Huffman, G.J., R.F. Adler, M. Morrissey, D.T. Bolvin, S. Curtis, R. Joyce, B McGavock, J. Susskind, 2001: Global Precipitation at One-Degree Daily Resolution from Multi-Satellite Observations. *J. Hydrometeor.*, **2**, 36-50.

Karl, T. R., G. A. Meehl, C. D. Miller, S. J. Hassol, A. M. Waple, and W. L. Murray, Eds., 2008: Weather and climate extremes in a changing climate. Regions of focus: North America, Hawaii, Caribbean, and U.S. Pacific Islands. U.S. Climate Change Science Program and the Subcommittee on Global Change Research Synthesis and Assessment Product 3.3, 180 pp.

Kim, H.-M., P. J. Webster, J. A. Curry, 2012: Seasonal prediction skill of ECMWF System 4 and NCEP CFSv2 retrospective forecast for the Northern Hemisphere winter. *Clim. Dyn.,* **39,** 2957-2973, doi: 10.1007/s00382-012-1364-6.

Kirtman, B. P., and Coauthors, 2014: The North American Multimodel Ensemble: Phase-1 seasonal-tointerannual prediction; phase-2 toward developing intraseasonal prediction. *Bull. Amer. Meteor. Soc.*, **95,** 585–601, doi:10.1175/BAMS-D-12-00050.1.

Klawa, M., and U. Ulbrich, 2003: A model for the estimation of storm losses and the identification of severe winter storms in Germany. *Nat. Hazards Earth Syst. Sci.,* **3**, 725–732, doi: 10.5194/nhess-3-725-2003.

Kunkel, K. E., R. A. Pielke Jr., and S. A. Changnon, 1999: Temporal fluctuations in weather and climate extremes that cause economic and human health impacts: A review. *Bull. Amer. Meteor. Soc.,* **80,** 1077-1098.

Kunkel, K. E., D. R. Easterling, D. A. R. Kristovich, B. Gleason, L. Stoecker, and R. Smith, 2012: Meteorological causes of the secular variations in observed extreme precipitation events for the conterminous United States. *J. Hydrometeor*., **13**, 1131-1141, doi: 10.1175/JHM-D-11-0108.1.

Kunkel, K. E., and Coauthors, 2013: Monitoring and understanding trends in extreme storms: State of knowledge. *Bull. Amer. Meteor. Soc.*, **94**, 499–514, doi: 10.1175/BAMS-D-11-00262.1.

Kuo, Y.-H., R. J. Reed, and S. Low-Nam, 1991: Effects of surface energy fluxes during the early development and rapid intensification states of seven explosive cyclones in the western Atlantic. *Mon. Wea. Rev.,* **119,** 457-476.

Lawrimore, J., T. R. Kari, and M. Squires, 2014: Trends and variability of severe snowstorms east of the Rocky Mountains. *J. Hydromet.*, **15,** 1762-1777, doi: 10.1175/JHM-D-13-068.s1.

Leckebusch, G. C., D. Renggli, and U. Ulbrich, 2008: Development and application of an objective storm severity measure for the northeast Atlantic region. *Meteor. Z.,* **17,** 575–587, doi: 10.1127/0941-2948/2008/0323.

Lim, E.-P., and I. Simmonds, 2007: Southern Hemisphere winter extratropical cyclone characteristics and vertical organization observed with the ERA-40 data in 1979-2001. *J. Climate,* **20,** 2675-2690, doi: 10.1175/JCLI4135.1.

Lin, H., G. Brunet, and J. S. Fontecilla, 2010: Impact of the Madden-Julian Oscillation on the intraseasonal forecast skill of the North Atlantic Oscillation. *Geophys. Res. Lett.,* **37,** L19803, doi:10.1029/2010GL044315.

Lindzen, R. S., and B. Farrell, 1980: A simple approximate result for maximum growth rate of baroclinic instabilities. *J. Atmos. Sci.,* **37,** 1648-1654.

Lukens, K. E., and E. H. Berbery, 2019: Winter Storm Tracks and Related Weather in the NCEP Climate Forecast System Weeks 3-4 Reforecasts for North America. *WAF,* **34,** 751-772, doi: 10.1175/WAF-D-18-0113.1.

Lukens, K. E., E. H. Berbery, and K. I. Hodges, 2018: The imprint of strong-storm tracks on winter weather in North America. *J. Climate*, **31,** 2057-2074, doi: 10.1175/JCLI-D-17-0420.1.

Ma, C.-G., and E. K. M. Chang, 2017: Impacts of storm-track variations on wintertime extreme weather events over the continental United States. *J. Climate,* **30,** 4601-4624, doi: 10.1175/JCLI-D-16-0560.1.

Ma, X., and Y. Zhang, 2018: Interannaul variability of the North Pacific winter storm track and its relationship with extratropical atmospheric circulation. *Clim. Dyn.,* **51,** 3685-3698, https://doi.org/10.1007/s00382-018-4104-8.

Maddox, R. A., C. F. Chappell, and L. R. Hoxit, 1979: Synoptic and meso-scale aspects of flash flood events. *Bull. Amer. Meteor. Soc.*, **60**, 115-123, doi:10.1175/1520-0477-60.2.115.

Mailier, P. J., D. B. Stephenson, C. A. T. Ferro, and K. I. Hodges, 2006: Serial clustering of extratropical cyclones. *Mon. Wea. Rev.,* **134,** 2224-2240.

Mak, M., 1998: Influence of surface sensible heat flux on incipient marine cyclogenesis. *J. Atmos. Sci.,* **55,** 820-834.

Mariotti, A., P. M. Ruti, and M. Rixen, 2018: Progress in subseasonal to seasonal prediction through a joint weather and climate community effort. *npj Climate and Atmos. Sci.,* **1,** 1-4, doi: 10.1038/s41612-018-0014-z.

Minobe, S., A. Kuwano-Yoshida, N. Komori, S.-P. Xie, and R. J. Small, 2008: Influence of the Gulf Stream on the troposphere. *Nature,* **452(7184),** 206-209, doi: 10.1038/nature06690.

Minobe, S., M. Miyashita, A. Kuwano-Yoshida, H. Tokinaga, and S.-P. Xie, 2010: Atmospheric response to the Gulf Stream: seasonal variations. *J. Climate,* **23,** 3699-3719, doi: 10.1175/2010JCLI3359.1.

Moriasi, D. N., Arnold, J. G., Van Liew, M. W., Bingner, R. L., Harmel, R. D., and Veith, T. L., 2007: Model evaluation guidelines for systematic quantification of accuracy in watershed simulations. *T. ASABE*, **50**, 885–900.

National Research Council, 2010: Assessment of intraseasonal to interannual climate prediction and predictability. *Washington, DC: The National Academies Press*. https://doi.org/10.17226/12878.

National Weather Service, 2019: NWS Service Change Notices: Archive of PNSs, SCNs and TINs, accessed 8 June 2019, https://www.weather.gov/notification/archive.

NCEP, 2015: GFS model upgrade on WCOSS. *NCEP Quarterly Newsletter,* accessed 8 June 2019, https://www.ncep.noaa.gov/newsletter/current/newsletter.pdf.

NCEP Central Operations, 2019: Changes to NCEP models/implementation dates to NOAAPORT, accessed 21 May 2019, https://www.nco.ncep.noaa.gov/pmb/changes/.

Newell, R. E., N. E. Newell, Y. Zhu, and C. Scott, 1992: Tropospheric rivers?—A pilot study. *Geophys. Res. Lett.,* **19,** 2401–2404.

Orlanski, I., and E. K. M. Chang, 1993: Ageostrophic geopotential fluxes in downstream and upstream development of baroclinic waves. *J. Atmos. Sci*., **50,** 212-225.

Pegion, K., and Coauthors, 2019: The Subseasonal Experiment (SubX): A multi-model subseasonal prediction experiment. *BAMS, submitted manuscript.*

Pendergrass, A., and NCAR Staff (Eds), 2015: The Climate Data Guide: GPCP (Daily): Global Precipitation Climatology Project. Retrieved from https://climatedataguide.ucar.edu/climate-data/gpcp-daily-global-precipitation-climatology-project

Pfahl, S., and H. Wernli, 2012: Quantifying the relevance of cyclones for precipitation extremes. J. Climate, **25**, 6770-6780, doi: 10.1175/JCLI-D-11-00705.1.

Pielke, Jr., R., and R. E. Carbone, 2002: Weather impacts, forecasts, and policy. *Bull. Amer. Meteor. Soc.,* **83,** 393-403.

Raible, C. C., 2007: On the relation between extremes of midlatitude cyclones and the atmospheric circulation using ERA40. *Geophys. Res. Lett.,* **34,** L07703, doi: 10.1029/2006GL029084.

Rutz, J. J., W. J. Steenburgh, and F. M. Ralph, 2014: Climatological characteristics of atmospheric rivers and their inland penetration over the western United States. *Mon. Wea. Rev.,* **142,** 905–921, doi:10.1175/MWR-D-13-00168.1.

Saha, S., and Coauthors, 2010a: NCEP Climate Forecast System Reanalysis (CFSR) 6-hourly products, January 1979 to December 2010. NCAR Computational and

Information Systems Laboratory Research Data Archive, accessed 11 March 2014, https://doi.org/10.5065/D69K487J.

Saha, S., and Coauthors, 2010b: The NCEP Climate Forecast System Reanalysis. *Bull. Amer. Meteor. Soc.,* **91**, 1015-1057, doi: 10.1175/2010BAMS3001.1.

Saha, S., and Coauthors, 2011, updated daily: NCEP Climate Forecast System Version 2 (CFSv2) 6-hourly Products. Research Data Archive at the National Center for Atmospheric Research, Computational and Information Systems Laboratory, https://doi.org/10.5065/D61C1TXF. Accessed 27 Feb 2019.

Saha. S., and Coauthors, 2014a: NCEP Climate Forecast System Reforecast products, December 1981 to March 2011. NOAA National Centers for Environmental Information, accessed 20 October 2017, https://www.ncdc.noaa.gov/data-access/model-data/model-datasets/climate-forecast-system-version2-cfsv2#CFS%20Reforecasts.

Saha. S., and Coauthors, 2014b: NCEP Climate Forecast System version 2 Operational Forecast products, April 2011 to Present. NOAA National Centers for Environmental Information, accessed 4 March 2019, https://www.ncdc.noaa.gov/data-access/model-data/model-datasets/climate-forecast-system-version2-cfsv2#CFSv2%20Operational%20Forecasts.

Saha. S., and Coauthors, 2014c: The NCEP Climate Forecast System version 2. *J. Climate,* **27,** 2185-2208, doi: 10.1175/JCLI-D-12-00823.1.

Salathé, E. P., Jr., 2006: Influences of a shift in North Pacific storm tracks on western North American precipitation under global warming. *Geophys. Res. Lett*., **33**, L19820.

Sanders, F., 1986: Explosive cyclogenesis in the west-central North Atlantic Ocean, 1981-84. Part I: Composite structure and mean behavior. *Mon. Wea. Rev.,* **114,** 1781-1794.

Shapiro, M., and Coauthors, 2010: An earth-system prediction initiative for the twenty-first century. *Bull. Amer. Meteor. Soc.,* **91**, 1377–1388.

Simmons, A. J., and B. J. Hoskins, 1979: The downstream and upstream development of unstable baroclinic waves. *J. Atmos. Sci.*, **36**, 1239-1254.

Sinclair, M. R., 1997: Objective identification of cyclones and their circulation intensity, and climatology. *Weather and Forecasting,* **12,** 595-612.

Smith, T. M., and R. E. Livezey, 1999: GCM systematic error correction and specification of the seasonal mean Pacific-North American region atmosphere from global SSTs. *J. Climate,* **12,** 273-288.

Sweeney, C. P., P. Lynch, and P. Nolan, 2013: Reducing errors of wind speed forecasts by an optimal combination of post-processing methods. *Meteorol. Appl.*, **20,** 32-40, doi: 10.1002/met.294.

Tebaldi, C., and R. Knutti, 2007: The use of the multi-model ensemble in probabilistic climate projections. *Phil. Trans. R. Soc. A*, **365,** 2053-2075, doi: 10.1098/rsta.2007.2076.

Tian, D., E. E. Wood, and X. Yuan, 2017: CFSv2-based sub-seasonal precipitation and temperature forecast skill over the contiguous Unites States. *Hydrol. Earth Syst. Sci.,* **21,** 1477-1490, doi: 10.5194/hess-21-1477-2017.

Trenberth, K. E., A. Dai, R. M. Rasmussen, and D. B. Parsons, 2003: The changing character of precipitation. *BAMS,* **84,** 1205-1217, doi: 10.1175/BAMS-84-9-1205.

Ulbrich, U., and M. Christoph, 1999: A shift of the NAO and increasing storm track activity over Europe due to anthropogenic greenhouse gas forcing. *Clim. Dyn.,* **15,** 551-559.

Vitart, F., 2014: Evolution of ECMWF sub-seasonal forecast skill scores. *Quart. J. Roy. Meteor. Soc.,* **140,** 1889-1899, doi: 10.1002/qj.2256.

Vitart, F., A. W. Robertson, and D. L. T. Anderson, 2012: Subseasonal to seasonal prediction project: Bridging the gap between weather and climate. *WMO Bull.,* **61**, 23–28.

Vitart, F., and Coauthors, 2017: The subseasonal to seasonal (S2S) prediction project database. *Bull. Amer. Meteor. Soc.,* **98,** 163-173, doi: 10.1175/BAMS-D-16-0017.1.

Waliser, D. E., K. M. Lau, W. Stern, and C. Jones, 2003: Potential predictability of the Madden-Julian Oscillation. *Bull. Amer. Meteor. Soc.,* **84,** 33–50, https://doi.org/10.1175/BAMS-84-1-33.

Wallace, J. M., G.-H. Lim, and M. L. Blackmon, 1988: Relationship between cyclone tracks, anticyclone tracks and baroclinic waveguides. *J. Atmos. Sci.,* **45**, 439-462.

Wang, W., P. Xie, S. H. Yoo, Y. Xue, A. Kumar, and X. Wu, 2011: An assessment of the surface climate in the NCEP climate forecast system reanalysis, *Clim. Dynamics*, **37,** 1601-1620, doi: 10.1007/s00382-010-0935-7.

Wang, Y., Q. Wang, and J. E. Taylor, 2017: Aggregated responses of human mobility to severe winter storms: An empirical study. PLoS ONE, 12(12), e0188734, doi: 10.1371/journal.pone.0188734.

Weber, N. J., and C. F. Mass, 2017: Evaluating CFSv2 subseasonal forecast skill with an emphasis on tropical convection. *Mon. Wea. Rev.,* **145,** 3795-3815, doi: 10.1175/MWR-D-17-0109.1.

Wei, M-Y, D. R. Johnson, and R. D. Townsend, 1983: Seasonal distributions of diabatic heating during the First GARP Global Experiment. *Tellus*, **35A**, 241-255.

White, C.J., and Coauthors, 2017: Review: Potential applications of subseasonal-to-seasonal (S2S) predictions. *Meteorol. Appl.,* **24,** 315-325, doi: 10.1002/met.1654.

Xie, P., M. Chen, and W. Shi, 2010: CPC unified gauge-based analysis of global daily precipitation. Preprints, 24th Conf. on Hydrology, Atlanta, GA, Amer. Meteor. Soc., 2.3A. [Available online at https://ams.confex.com/ams/90annual/webprogram/Paper163676.html.]

Xie, P., A. Yatagai, M. Chen, T. Hayasaka, Y. Fukushima, C. Liu, and S. Yang, 2007: A gauge-based analysis of daily precipitation over East Asia. *J. Hydrometeorol.,* **8,** 607– 626.

Xie, P., R. Joyce, S. Wu, S. Yoo, Y. Yarosh, F. Sun, and R. Lin, 2017: Reprocessed, Bias-Corrected CMORPH Global High-Resolution Precipitation Estimates from 1998. *J. Hydrometeor.* doi:10.1175/JHM-D-16-0168.1.

Yang, X., and Coauthors, 2015: Seasonal predictability of extratropical storm tracks in GFDL's high-resolution climate prediction model. *J. Climate,* **28,** 3592-3611, doi: 10.1175/JCLI-D-14-00517.1.

Yao, Y., W. Perrie, W. Zhang, and J. Jiang, 2008: Characteristics of atmosphere-ocean interactions along North Atlantic extratropical storm tracks. *J. Geophys. Res.,* **113,** D14124, doi: 10.1029/2007JD008854.

Yin, J. H., 2005: A consistent poleward shift of the storm tracks in simulations of 21st century climate. *Geophys. Res. Lett,* **32,** L18701, doi:10.1029/2005GL023684.

Zhang, L., A. Kumar, and W. Wang, 2012: Influence of changes in observations on precipitation: a case study for the Climate Forecast System Reanalysis (CFSR), J. Geophys. Res., **117**, D08105, doi:10.1029/2011JD017347.

Zheng, C., E. K.-M. Chang, H.-M. Kim, and M. Zhang, 2018: Impacts of the Madden-Julian Oscillation on storm-track activity, surface air temperature, and precipitation over North America. *J. Climate,* **31,** 6113-6134, doi: 10.1175/JCLI-D-17-0534.1.

Zhu, Y., and Y. Luo, 2015: Precipitation calibration based on the frequency-matching method. *Wea. Forecasting*, **30,** 1109-1124, doi: 10.1175/WAF-D-13-00049.1.